Aus dem Institut für Medizinische Informatik
der Medizinischen Fakultät Charité - Universitätsmedizin Berlin

DISSERTATION

Development and validation of *in vivo* ultrasound time-harmonic elastography of the human brain towards clinical application

Entwicklung und Validierung der *in vivo* zeitharmonischen Ultraschall-Elastografie des menschlichen Gehirns für die klinische Anwendung

zur Erlangung des akademischen Grades
Doctor of Philosophy (PhD)

vorgelegt der Medizinischen Fakultät
Charité - Universitätsmedizin Berlin

von

Bernhard Kreft

Datum der Promotion: 25.06.2023

Contents

List of Abbreviations 2

List of Figures 6

Abstract 7

Kurzfassung 8

1 Introduction 9

2 Theory 11
- 2.1 Purely elastic materials 11
- 2.2 Purely viscous materials 13
- 2.3 Oscillating stress and complex modulus $\boldsymbol{G}^*$ 13
- 2.4 Mechanical waves 14
- 2.5 Physiology of intracranial pressure 17

3 Materials and Methods 20
- 3.1 Experimental setup 20
- 3.2 Studies on healthy volunteers 23
- 3.3 Clinical patient study 27

4 Results 29
- 4.1 Studies on healthy volunteers 29
- 4.2 Clinical patient study 32

5 Discussion 35
- 5.1 Cerebral THE in healthy volunteers 35
- 5.2 Clinical patient study 37
- 5.3 Limitations 39

6 Conclusion 40

References 41

Eidesstattliche Erklärung 54

Anteilserklärung an den erfolgten Publikationen 55

Publications 58
- Time-Resolved Response of Cerebral Stiffness to Hypercapnia in Humans 58
- Corrigendum to: "Time Resolved Response of Cerebral Stiffness to Hypercapnia in Humans" 67
- Cerebral Ultrasound Time-Harmonic Elastography Reveals Softening of the Human Brain Due to Dehydration 67
- Noninvasive Detection of Intracranial Hypertension by Novel Ultrasound Time-Harmonic Elastography 78

Curriculum Vitae 87

Danksagung 89

List of Abbreviations

ARFI	Acoustic Radiation Force Impulse
CBF	Cerebral Blood Flow
CS	Cerebral Stiffness
CSF	Cerebrospinal fluid
ICP	Intracranial Pressure
IIH	Idiopathic Intracranial Hypertension
LP	Lumbar Puncture
MRE	Magnetic Resonance Elastography
MRI	Magnetic Resonance Imaging
THE	Time-Harmonic Elastography

List of Figures

2.1 **Principal types of deformation in elastic solids.** (A) Uniaxial deformation, where stress and strain are related through the Young's modulus E, (B) Shear deformation, where stress and strain are related through the shear modulus μ and, (C) volumetric deformation, where stress and strain are related through the bulk modulus K. Red arrows labelled with $\vec{F}$ denote the direction of the applied force, while blue brackets denote the resulting deformation along the main axes. Black dashed lines represent the original shape of the block and solid lines the deformed state under the influence of the acting force. . . 12

2.2 **Shear deformation of a viscous fluid modeled as laminar flow between two plates.** Schematic representation of the shear deformation of a viscous fluid modeled with fluid layers in equal distance dz to each other. The acting force $\vec{F}$ along the top layer is denoted as a red arrow. The top layer moves with speed v_{max}, while the bottom layer does not move, resulting in a speed gradient dv/dz, denoted as blue bracket. 13

2.3 **Schematic illustration of compression- and shear wave.** (A) Pressure wave, where the propagation direction corresponds to the deformation direction and (B) shear wave, where the deformation direction is perpendicular to the propagation direction. 15

2.4 **Exponential relationship between averaged ICP and intracranial volume. Figure adapted from Marmarou *et al.* [54] with friendly permission of the Journal of Neurosurgery Publishing Group.** Schematic representations of the exponential relationship between ICP and intracranial volume. At low pressures and high compliance (i), cardiac-induced blood volume variations will result in small ICP fluctuations. At high pressures and low compliance (ii), the same volume change results in a larger cardiac-induced ICP fluctuation. 17

3.1 **Experimental setup for cerebral THE. Figure adapted from Kreft *et al.* [78].** The setup comprised three main components: (i) the customized patient bed with the vibration plate (red), (ii) the clinical ultrasound scanner and (iii) the elastography computer with the integrated post processing software. The magnification shows the positioning of the ultrasound probe on the volunteer's temporal bone window to conduct transcranial ultrasound. 20

3.2 **Flowchart of the post-processing pipeline.** Schematic description of the steps of pot-processing starting with the RF data acquired by transcranial ultrasound and finishing with the frequency-compounded elastogram. 21

3.3 **Multifrequency waveform and the resulting frequency spectrum along with frequency-resolved shear wave fields and elastograms. Figures adapted from Tzschätzsch *et al.* [41].** (A) The waveform fed into the amplifier in the time domain (top panel) and in the frequency domain (bottom panel). Alternating aliased and unaliased frequencies due to the stroboscopic sampling are marked as blue peaks in the spectrum. (B) Shear wave fields (top panel) of different vibration frequencies with the manually measured wavelengths marked as white lines and the corresponding frequency resolved elastograms (bottom panel). 22

3.4 **Representative B-mode image along with corresponding elastogram.** (A) B-mode image reconstructed from radiofrequency (RF-) data and (B) average elastogram compounded from all vibration frequencies with a threshold of 1 m/s. Anatomical features such as (i) dura, (ii) temporal lobe parenchyma, (iii) hyperechogenic basal cisterns and (iv) hypoechogenic mesencephalic brainstem are demarcated by white lines. Regions of Interest (ROI) were drawn manually in (ii) the temporal lobe parenchyma. 23

3.5 **Measurement setup for hypercapnia experiment. Figure adapted from Kreft *et al.* [77] with friendly permission of Elsevier Publishers.** Basic experimental setup for cerebral THE, as described in Section 3.1 with four additional components: supply of CO_2-enriched gas comprising of (i) an airtight breathing mask connected to a (ii) carbogen gas cylinder, (iii) a patient monitor connected to the volunteer to provide the monitoring of heart rate via pulsoxymeter as well as $etCO_2$ via capnometry, visible in the magnification (top-right) and (iv) a customized mounting device for the ultrasound probe to minimalize volunteer and operator movement, illustrated in more detail in the magnification (top-left). 24

3.6 **Flowchart diagram of the hypercapnia study design.** All volunteers underwent continous monitoring of SWS, heart rate and $etCO_2$ (measurements every 10 seconds) as well as blood pressure (every 2 minutes) for 22 minutes in total. The experiment was subdivided in three phases of 7 minutes each: (i) Baseline phase, where volunteers breathed ambient air, (ii) hypercapnia phase, where carbogen was administered and (iii) recovery phase, where volunteers breathed ambient air again. In the following, correlation analysis based on Pearson‘s linear correlation coefficient and group analysis based on paired *t*-tests were performed. 25

3.7 **Flowchart diagram of the dehydration study design. Adapted and modified from Kreft *et al.* [78].** Volunteers were first measured in a normally hydrated state (NH). After a 12-h-fasting period, measurements were conducted in the dehydrated state (DH). Then, 4 sets of data in different hydration states were acquired after oral rehydration (RH1 – RH4) in a 15-min-increment. For every hydration state, cerebral time-harmonic elastography (cerebral THE), transcranial Doppler (TCD), blood pressure and heart rate measurement was performed. Urine samples for determination of urine osmolality were taken at hydration states NH, DH and RH4. While all volunteers were included in the correlation analysis, only 10 volunteers were included in the group analysis, because two volunteers did not comply with the fasting protocol, as determined by their urine osmolality. 26

3.8 **Flowchart diagram of the IIH study design. Figure adapted and modified from Kreft *et al.* [79] with friendly permission of Wolters Kluwer Health Publishers.** Two study cohorts were investigated in this study. The clinical group consisted of 22 participants with known or initial diagnosis of idiopathic intracranial hypertension (IIH) enrolled for treatment by lumbar puncture (LP), while the control cohort consisted of 18 healthy volunteers, who did not receive LP. Cerebral ultrasound time-harmonic elastography (cerebral THE) was performed both before and after treatment on diseased participants and once on healthy participants. Invasively measured cerebrospinal fluid pressure (P_{CSF}) and drained CSF volume (V_{CSF}) was recorded during LP. Participants with P_{CSF} below a threshold of $25\,cmH_2O$ ($n = 4$) were excluded from all steps of group analysis. 27

4.1 **Representative elastograms of one volunteer during baseline, hypercapnia, and recovery phase. Figure adapted from Kreft *et al.* [77] with friendly permission of Elsevier Publishers.** Representative SWS maps of one volunteer with a penetration depth of 8 cm measured during the second half (late phases) of (A) baseline, (B) hypercapnia, and (C) recovery. The shift towards red colors (equals stiffening) is clearly visible within the temporal lobe parenchyma demarcated by manually drawn ROI (white line). 29

4.2 **Statistical boxplot of the hypercapnia data along with time resolved mean SWS and mean etCO$_2$. Figure adapted from Kreft *et al.* [77] with friendly permission of Elsevier Publishers.** (A) Mean values corresponding to the group data analysis, in which data were averaged over time during the second halves (late phases) of baseline, hypercapnia, and recovery. Gray lines connect mean SWS values in each volunteer, while red symbols indicate outliers. (B) Group mean SWS values (blue) and etCO$_2$ (red) with mean fit curves shown as dotted lines. Baseline mean SWS is demarcated by the dashed line, while standard deviations for SWS and etCO$_2$ are shown by light gray and light red areas. Vertical lines indicate the transition to the next phase. The horizontal arrows indicate time points of increase (τ_i) and decrease (τ_d) in SWS and etCO$_2$. While τ_i is nearly the same for both parameters during hypercapnia, τ_d significantly differs during recovery. 30

4.3 **Representative elastograms of one volunteer in normally hydrated, dehydrated, and rehydrated states. Figure adapted from Kreft *et al.* [78].** Elastograms of one volunteer in (A) normally hydrated (NH), (B) dehydrated (DH) and (C) rehydrated (RH4) condition are shown as color-coded shear wave speed (SWS) maps with a penetration depth of 12 cm. In the normally hydrated state (A) as well as in the rehydrated state (C), mean SWS in the demarcated region of interest (ROI, white line) is higher than in the dehydrated state (B). 30

4.4 **Boxplots of SWS and urine osmolality during de- and oral rehydration. Figures adapted from Kreft *et al.* [78].** Boxplots of mean SWS (A) across all hydration states and urine osmolality (B) of three hydration states – normal hydration (NH), dehydration (DH), and rehydration (RH4). Urine osmolality increased after dehydration and decreased to normal hydration values after 1 hour of rehydration. Conversely, SWS significantly decreased after 12 hours of fasting and returned to normal hydration values within 30 minutes after oral rehydration. Two volunteers (□ and ◇, dashed red) were excluded from statistical group analysis due to incomplete fasting, as reflected in urine osmolality and confirmed by them after the experiment. Significant differences between the groups are indicated by * ($p < 0.05$) and ** ($p < 0.001$). 31

4.5 **Scatter plot of SWS and urine osmolality. Figure adapted from Kreft *et al.* [78].** Pearson's linear correlation between shear wave speed (SWS) and urine osmolality (30 values each, $p < 0.001$, $r = -0.68$). Linear regression is shown as black line. The two volunteers (□ and ◇, red) excluded from the group analysis were included in the correlation analysis as they received urine osmolality quantification. 32

4.6 **Representative elastograms of one healthy volunteer one patient before and after LP. Figure adapted from Kreft *et al.* [79] with friendly permission of Wolters Kluwer Health Publishers.** (A) B mode image with demarcated region of interest (ROI, white line). (B) Elastogram before CSF drainage treatment; and (C) elastogram 30 min after treatment. While the decrease in SWS resulting from CSF drainage following lumbar puncture from images (B) to (C) is more clearly visible in the top region of the ROI, the overall percentage decrease is the same throughout the area of interest. 32

4.7 **Statistical plots of group analysis and diagnostic performance. Figures adapted from Kreft *et al.* [79] with friendly permission of Wolters Kluwer Health Publishers.** (A) Boxplots of mean SWS values in healthy volunteers as well as patients before and after LP treatment. Significant differences were observed between healthy volunteers and patients before LP treatment ($p < 0.001$), and between patients before and after LP treatment ($p < 0.001$) while SWS was not distinguishable between healthy volunteers and patients after treatment ($p = 0.60$). Lines connect mean SWS values for individual patients included in the statistical group analysis ($P_{\mathrm{CSF}} > 25\,\mathrm{cmH_2O}$, grey) and patients excluded from in the group statistics ($P_{\mathrm{CSF}} < 25\,\mathrm{cmH_2O}$, red). (B) ROC curve with ICP cutoff of 25 $\mathrm{cmH_2O}$ (according to the clinical threshold of IIH diagnosis). An optimum SWS cutoff of 1.67 m/s was derived. 33

4.8 **Scatter plots of statistical correlation analysis. Figures adapted from Kreft *et al.* [79] with friendly permission of Wolters Kluwer Health Publishers.** (A) Correlation between SWS before LP and CSF volume drained from the spinal tap. A moderate linear correlation with a slope of 0.01 m/(s·ml) was revealed ($r = 0.72$, $p < 0.001$). (B) A similar correlation was found between SWS before LP and CSF opening pressure with a slope of 0.01 $\mathrm{m/(s\cdot cmH_2O)}$ with $r = 0.69$ and $p < 0.001$. Patients who did not meet the final criterion of an opening pressure $P_{\mathrm{CSF}} > 25\,\mathrm{cmH_2O25}$ but were included in this analysis are marked by red diamonds (◊). 34

Abstract

Motivation: In neurology, the determination of intracranial pressure (ICP) is of central importance for the diagnosis of brain damage. However, reliable ICP measurements are realized by invasive techniques such as lumbar puncture or surgically implanted pressure probes. Cerebral stiffness (CS) measured by elastography could be a parameter sensitive to ICP variations. However, CS is currently measured exclusively by magnetic resonance elastography, which is associated with long examinations and limited availability. Time-harmonic shear wave excitation used in magnetic resonance elastography combined with transcranial ultrasound (cerebral THE) can provide reproducible and stable elastograms over a large field-of-view in real-time. Initial applications of cerebral THE in healthy volunteers during performance of the Valsalva maneuver demonstrated sensitivity of CS to blood flow and pressure changes in the brain. The goal of this PhD project was to optimize and validate cerebral THE that I previously developed to quantify CS, identify it as a marker of cerebral perfusion, and provide initial evidence for the potential clinical application of the method as a noninvasive technique for estimating ICP.

Methods: To this end, I conducted two studies in healthy volunteers aimed at artificial manipulation of cerebral blood flow: (i) I investigated the effect of hypercapnia during breathing of carbon dioxide-enriched gas and (ii) the effect of dehydration and oral rehydration on CS measured by cerebral THE. Finally, I applied cerebral THE in a pilot clinical study in patients with idiopathic intracranial hypertension (IIH) who underwent lumbar puncture (LP) along with invasive quantification of cerebrospinal fluid (CSF) opening pressure and, if necessary, CSF drainage.

Results: Hypercapnia increased CS by $6 \pm 4\,\%$ above baseline. In contrast, dehydration of healthy volunteers resulted in a decrease in CS of $4 \pm 2\,\%$, whereas CS returned to baseline after oral rehydration. In patients with IIH, CS was $16 \pm 5\,\%$ higher than in healthy volunteers and correlated positively with CSF opening pressure ($r = 0.69$, $p < 0.001$). Approximately 30 min after LP, patients' CS values were within the range of CS values in healthy volunteers.

Conclusion: Cerebral THE proved to be a reproducible, stable imaging technique for real-time determination of CS. This project demonstrated that changes in CS are closely associated with changes in cerebral perfusion and ICP. These results suggest that cerebral THE may be a promising noninvasive diagnostic tool for determining ICP in routine clinical practice.

Kurzfassung

Motivation: In der Neurologie ist die Bestimmung des intrakraniellen Drucks (ICP) von zentraler Bedeutung für die Diagnose von Hirnschäden. Zuverlässige ICP-Messungen werden jedoch durch invasive Techniken wie die Lumbalpunktion oder chirurgisch implantierte Drucksonden realisiert. Die mittels Elastografie gemessene zerebrale Steifigkeit (CS) könnte ein Parameter sein, der empfindlich auf ICP-Schwankungen reagiert. Allerdings wird die CS derzeit ausschließlich mit der Magnetresonanz-Elastografie gemessen, die mit langen Untersuchungen und begrenzter Verfügbarkeit verbunden ist. Zeitharmonische Scherwellenanregung, wie sie in der Magnetresonanz-Elastografie verwendet wird, kombiniert mit transkraniellem Ultraschall (zerebrale THE) kann reproduzierbare, stabile Elastogramme über ein großes Sichtfeld in Echtzeit liefern. Erste Anwendungen der zerebralen THE bei gesunden Probanden während der Durchführung des Valsalva-Manövers zeigten, dass die CS empfindlich auf Blutflussund Druckänderungen im Gehirn reagiert. Ziel dieses Promotionsprojekts war die Optimierung und Validierung der zerebralen THE, welche ich zuvor entwickelt habe, um CS zu quantifizieren, als Marker für zerebrale Perfusion zu identifizieren und erste Beweise für die potenzielle klinische Anwendung der Methode als nichtinvasive Technik zur Abschätzung des ICP zu liefern.

Methoden: Zu diesem Zweck führte ich zwei Studien an gesunden Probanden durch, welche die künstliche Manipulation des zerebralen Blutflusses zum Ziel hatten: (i) Ich untersuchte die Auswirkung von Hyperkapnie während der Atmung von mit Kohlendioxid angereichertem Gas und (ii) die Auswirkung von Dehydrierung und oraler Rehydrierung auf die durch zerebrale THE gemessene CS. Schließlich habe ich die zerebrale THE in einer klinischen Pilotstudie bei Patienten mit idiopathischer intrakranieller Hypertension (IIH) angewandt, bei denen eine Lumbalpunktion (LP) zusammen mit einer invasiven Quantifizierung des Liquoröffnungsdrucks und, falls erforderlich, einer Liquordrainage durchgeführt wurde.

Ergebnisse: Hyperkapnie erhöhte den CS um $6 \pm 4\,\%$ über den Ausgangswert. Im Gegensatz dazu führte die Dehydratation gesunder Probanden zu einem Rückgang des CS um $4 \pm 2\,\%$, während der CS nach oraler Rehydrierung wieder den Ausgangswert erreichte. Bei Patienten mit IIH war die CS um $16 \pm 5\,\%$ höher als bei gesunden Probanden und korrelierte positiv mit dem Liquoröffnungsdruck ($r = 0.69$, $p < 0.001$). Etwa 30 Minuten nach der LP lagen die CS Werte der Patienten im Bereich der CS Werte gesunder Probanden.

Schlussfolgerung: Die zerebrale THE erwies sich als reproduzierbares, stabiles bildgebendes Verfahren zur Echtzeit-Bestimmung der CS. Dieses Projekt zeigte, dass Änderungen des CS eng mit Änderungen der zerebralen Perfusion und des ICP verbunden sind. Diese Ergebnisse deuten darauf hin, dass die zerebrale THE ein vielversprechendes nichtinvasives Diagnoseinstrument zur Bestimmung des ICP in der klinischen Routinepraxis sein könnte.

1. Introduction

Intracranial pressure (ICP) monitoring is crucial in today's clinical practice for patients with neurological conditions such as stroke, ischemia, intracranial tumors, hydrocephalus, meningitis, or liver failure [1, 2, 3, 4]. Due to the formation of edema or hemorrhage, ICP is easily derailed in these patients [5, 6]. However, the current gold standard methods to monitor ICP, such as pressure probes implanted in the brain by a neurosurgeon or lumbar puncture (LP), are time-consuming and highly invasive [7, 8, 9, 10]. They are also associated with a high risk of complications, such as bleeding, displacement of the probe, or infection [11, 12]. To prevent excessive burden on medical staff as well as patients in such situations, a rapidly feasible, noninvasive technique to reliably detect ICP would be of great benefit to clinical practice.

To realize this, several noninvasive imaging techniques for visualization or quantification of ICP-related parameters have been developed and investigated in recent years. Promising approaches to date have included measuring anatomical features such as midline shift using computed tomography [13, 14], measuring brain parenchymal compliance using magnetic resonance imaging (MRI) [15, 16], and determining optic nerve sheath diameter using ocular ultrasound [17]. Although great progress has been made, these techniques are not yet reliable and reproducible enough to monitor ICP as continuously and accurately as the invasive procedures [7, 12]. For this reason, none of these techniques can be used independently to decide on further therapies. Rather, multiple examinations, including computed tomography, MRI, and ultrasound, are performed when elevated ICP is suspected, and the exact procedures depend on local standards [5, 18, 19].

Since pressure is physically associated with mechanical deformation, a potential ICP-sensitive parameter could be based on noninvasive *in vivo* quantification of the viscoelastic properties of brain tissue by detecting shear waves with modern imaging modalities such as MRI or ultrasound, also known as *elastography* [20, 21]. Due to the use of time-harmonic wave excitation that can produce stable shear waves within the intact skull, mechanical imaging of the brain has been performed exclusively with magnetic resonance elastography (MRE). However, despite numerous advances towards real-time MRE [22, 23, 24], this technique is still associated with long acquisition times. Due to rapid autoregulatory mechanisms, mechanical parameters such as stiffness and viscosity in the brain can change within seconds [25, 26], making MR-based elastography limited in its ability to detect these dynamic effects.

The application of fast ultrasound-based elastography techniques could easily overcome this limitation. The most common quantitative ultrasound elastography techniques rely on focused *acoustic radiation force impulses* (ARFI) generated by the ultrasound transducer for tissue deformation. However, because the skull distorts the ultrasound beam and absorbs most of the signal, focusing ARFI within the brain is difficult, making this type of elastography unsuitable for transcranial applications [27]. Furthermore, ARFI-based techniques can only illuminate a small portion of the ultrasound field-of-view (approximately 2×2 cm2) and achieve a maximum penetration depth of 8 cm, making it difficult to obtain an overview of the spatial distribution of mechanical parameters and any abnormalities [28, 29, 30, 31].

Recently, a new elastography technique was introduced, ultrasound time-harmonic elastography (THE) [32], which combines the external time-harmonic excitation used in MRE applications with fast ultrasound image acquisition. This technique allows measurement of tissue elasticity throughout the ultrasound field-of-view at depths up to 13 cm in real-time and with high stability due to multifrequency excitation. So far, THE has been successfully tested on abdominal organs such as liver and spleen [32], kidneys [33] as well as pancreas [34] and showed good diagnostic performance for diseases such as liver fibrosis [35], chronic kidney disease [36] or non-alcoholic fatty liver disease [37]. In addition, abdominal THE proved to be sensitive to changes in blood flow and pressure, either caused by the Valsalva maneuver [38], water ingestion [39] or disease such as portal hypertension [40].

Based on these findings, I adapted and modified THE for use on the brain (cerebral THE) prior to the start of this project to quantify cerebral stiffness (CS) in real-time. Initial applications showed that cerebral THE was a reproducible and stable technique, which was also able to reproduce results from previous MRE studies regarding brain softening with age [41, 42, 43]. Moreover, I found that CS measured with cerebral THE was increased in healthy volunteers performing the Valsalva maneuver [41], which can be attributed to increased cerebral perfusion and ICP [24, 44, 45, 46].

Since the main purpose of ICP is to autoregulate cerebral blood flow [47], the sensitivity of cerebral THE to perfusion changes in abdominal organs and brain suggests that cerebral THE may be sensitive to changes in ICP. The aim of my PhD project was to substantiate this hypothesis by performing two further studies in healthy volunteers, examining CS under known conditions associated with altered cerebral perfusion. After this validation phase, I performed a pilot clinical study to investigate the relationship between CS and ICP in patients suffering from idiopathic intracranial hypertension (IIH) who received invasive quantification of cerebrospinal fluid (CSF) opening pressure as a surrogate for ICP along with therapy in the form of lumbar puncture.

2. Theory

Elastography in the clinical context is based on manual palpation, which allows the physician to feel hard or soft structures in comparison to the surrounding tissue below the skin surface. Modern elastography techniques offer the possibility to quantitatively determine the viscoelastic properties of deep-seated tissue. Viscoelasticity is a characteristic property of soft tissue, composed of viscous and elastic behavior, and describes the ability of the tissue to resist deformation. This deformation, further referred to as strain ϵ, is triggered by the action of external forces, hereafter referred to as stress σ. These deformations can occur in numerous variations depending on the nature of the material and the type of applied stress. In rheology, a distinction is made between purely elastic, purely viscous, and viscoelastic materials.

2.1 Purely elastic materials

In purely elastic materials, the energy used to generate a strain ϵ under the influence of a certain stress σ is completely stored. A purely elastic material will therefore always regain its original shape as soon as the stress is removed [20]. The governing equation for the mathematical description of the linear relationship between stress and strain in elastic materials is known as *Hooke's law.*

$$\sigma = \Gamma \cdot \epsilon \tag{2.1}$$

The coupling constant Γ, commonly referred to as the mechanical modulus, is a characteristic material property that depends on the type of stress applied to the material. Any stress applied to a particular material can be represented by a superposition of three special cases: (i) uniaxial stress, (ii) shear stress, and (iii) volumetric stress. The mathematical description of these special cases along with the acting forces as well as the strain response to the associated deformations are shown in Figure 2.1. Here, a linearly elastic, solid, and isotropic material is assumed.

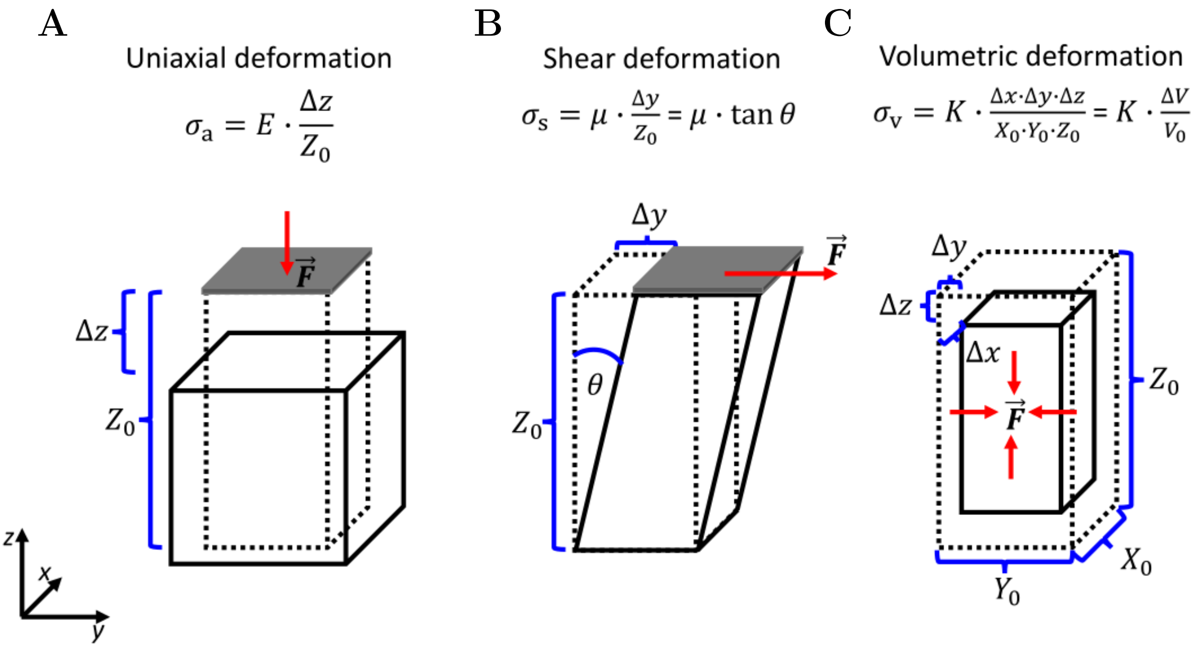
A
Uniaxial deformation
$\sigma_a = E \cdot \frac{\Delta z}{Z_0}$
Δz
Z_0
$\vec{F}$
z
x
y
B
Shear deformation
$\sigma_s = \mu \cdot \frac{\Delta y}{Z_0} = \mu \cdot \tan\theta$
Δy
$\vec{F}$
θ
Z_0
C
Volumetric deformation
$\sigma_v = K \cdot \frac{\Delta x \cdot \Delta y \cdot \Delta z}{X_0 \cdot Y_0 \cdot Z_0} = K \cdot \frac{\Delta V}{V_0}$
Δy
Δz
Δx
$\vec{F}$
Z_0
X_0
Y_0

Figure 2.1: Principal types of deformation in elastic solids.

In the case of uniaxial deformation (Figure 2.1A), the external force acts along a direction and perpendicular to the surface of the material, causing a shortening of the block along this direction, which is defined by the *Young's modulus* E. In shear deformation (Figure 2.1B), the external force acts parallel to the surface of the material. The strain here depends on the tilt angle Θ of the material and is determined by the *shear modulus* μ. If forces act perpendicular to the material surface from all sides, the effect is volumetric deformation (Figure 2.1C). The relationship between stress and volume change is determined by the *bulk modulus* K. The mechanical moduli describing these special cases are coupled via the *Poisson's ratio* ν, which is the material constant defined as the ratio between the deformation parallel and perpendicular to the effective direction of the external force and thus describes the compressibility of a material [20].

$$\mu = \frac{E}{2(1+\nu)} \tag{2.2}$$

$$K = \frac{E}{3(1-2\nu)} \tag{2.3}$$

Since biological soft tissues have a large water content, the Poisson's ratio can be approximated by $\nu \approx 0.5$ [20]. In this case, the relationship between Young's-, shear- and bulk modulus can be simplified.

$$K \gg E \approx 3\mu \tag{2.4}$$

2.2 Purely viscous materials

In contrast to an elastic medium, in a purely viscous medium the deformation energy is converted into thermal energy by friction, so that the strain remains after the stress is removed. The relationship between stress and strain such a medium can be derived mathematically by assuming laminar flow of a viscous fluid confined between two infinite plates, as shown in Figure 2.2.

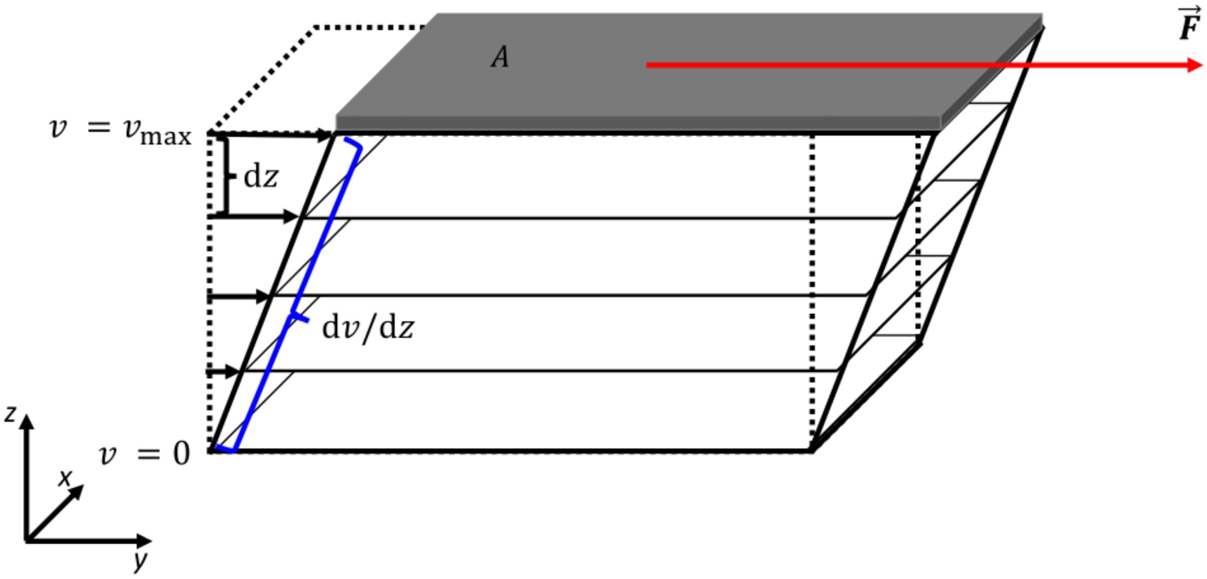

Figure 2.2: Shear deformation of a viscous fluid modeled as laminar flow between two plates.

The fluid is thereby divided into thin layers running parallel to the x-y plane at a distance dz. If a shear force $\vec{F}$ is applied to the upper plate parallel to its surface, the layers begin to flow in the direction of the force, while their velocity v varies from 0 at the lower, stationary plate to $v_{\max}$ at the upper plate. The infinitesimal velocity difference between the layers is thereby dv. The shear stress σ_{s}, which ensures that the upper layer moves at a constant velocity, therefore depends on the derivative of the velocity with respect to the height of the layer dv/dz, also referred to as shear rate $\dot{\epsilon}_{\mathrm{s}}$, and the viscosity η of the fluid.

$$\sigma_{\mathrm{s}} = \eta \frac{dv}{dz} = \eta \dot{\epsilon}_{\mathrm{s}} \tag{2.5}$$

2.3 Oscillating stress and complex modulus G^*

The mechanical moduli E, μ and K described above, as well as the viscosity η, have so far been derived as real-valued quantities under static deformation. However, when an oscillating stress with angular frequency ω of the form $\sigma(t) = \sigma_0 e^{\mathrm{i}\omega t}$ is applied to a material over a time t, the moduli can also take complex values. While the resultant strain for an elastic solid remains simply a scaled version of the stress of the form:

$$\epsilon(t)E = \sigma_0 e^{\mathrm{i}\omega t} \tag{2.6}$$

, the resultant strain for a viscous fluid exhibits an interesting property. The time derivative of the oscillatory strain results in a phase shift of 90 degrees, described by the complex unit i. The strain therefore lags the stress by 1/4 of an oscillation period.

$$\epsilon(t)\eta\mathrm{i}\omega = \sigma_0 e^{\mathrm{i}\omega t} \tag{2.7}$$

Up to this point, only purely elastic and viscous materials have been considered. However, this description is an idealized model, which in many cases does not correspond to reality. Most materials, especially biological soft tissue consisting of solid and fluid compartments, exhibit both behaviors simultaneously. They are therefore referred to as viscoelastic materials. For these types of materials, the coupling between stress and strain can be described by the complex shear modulus G^* and the complex bulk modulus H^*:

$$G^* = |G^*|e^{\mathrm{i}\varphi_G} \tag{2.8}$$

$$H^* = |H^*|e^{\mathrm{i}\varphi_H} \tag{2.9}$$

Where $|G^*|$ and $|H^*|$ denote the Euclidean norm of G^* and H^* and mainly represent the elastic properties. The phase angle φ describes the phase shift between stress and strain and is mainly responsible for the viscous behavior. The complex notation of the mechanical modulus has a decisive advantage since it allows the mechanical behavior of a viscoelastic material to be easily described with a single material constant. In elastography, mechanical waves are coupled into the tissue by applying oscillating stresses. The propagation behavior of these waves in biological soft tissue can be analyzed and related to the complex modulus G^*.

2.4 Mechanical waves

When an oscillating stress is applied to a material, particles at any position $\vec{r}$ within the material will displace at any time t, which can be expressed using a displacement field of the form $\vec{u}(\vec{r}, t)$. Assuming small strains, and thus a linear relationship between stress and strain, the strain tensor $\boldsymbol{\epsilon}$ can be expressed using the displacement field.

$$\boldsymbol{\epsilon} = \frac{1}{2}(\nabla\vec{u} + \nabla\vec{u}^T) \tag{2.10}$$

In addition, the strain tensor can be expressed as a superposition of pure compression and pure shear deformation.

$$\boldsymbol{\epsilon} = \boldsymbol{\epsilon}_{\text{compr.}} + \boldsymbol{\epsilon}_{\text{shear}} \tag{2.11}$$

The spatial and temporal behavior of the displacement field $\vec{u}$ caused by mechanical waves in a viscoelastic material can generally be described by the Navier equation with the complex bulk modulus H^* and the complex shear modulus G^* [48].

$$\rho\ddot{\vec{u}} = \left(H^* - \frac{4}{3}G^*\right)\nabla\left(\nabla\cdot\vec{u}\right) - G^*\nabla\times\left(\nabla\times\vec{u}\right) \tag{2.12}$$

The density of the material under consideration is denoted here by ρ, while $\ddot{\vec{u}}$ describes the second time derivative of the displacement field. Analogous to the strain tensor, the displacement field $\vec{u}$ can be decomposed a pure compression and a pure shear deformation. This is done by applying the Helmholtz decomposition, which states that any non-singular smooth vector field can be decomposed into the summation of a divergence-free ($\nabla\times\vec{\phi}$) and a curl-free ($\nabla\cdot\vec{\psi}$) vector field.

$$\vec{u} = \nabla\times\vec{\phi} + \nabla\cdot\vec{\psi} \tag{2.13}$$

Here, the curl-free vector field represents the pure compression wave field, while the divergence-free vector field describes the pure shear wave field. Figure 2.3 shows the two types of waves with a uniform propagation direction and their respective longitudinal and transverse particle motion directions.

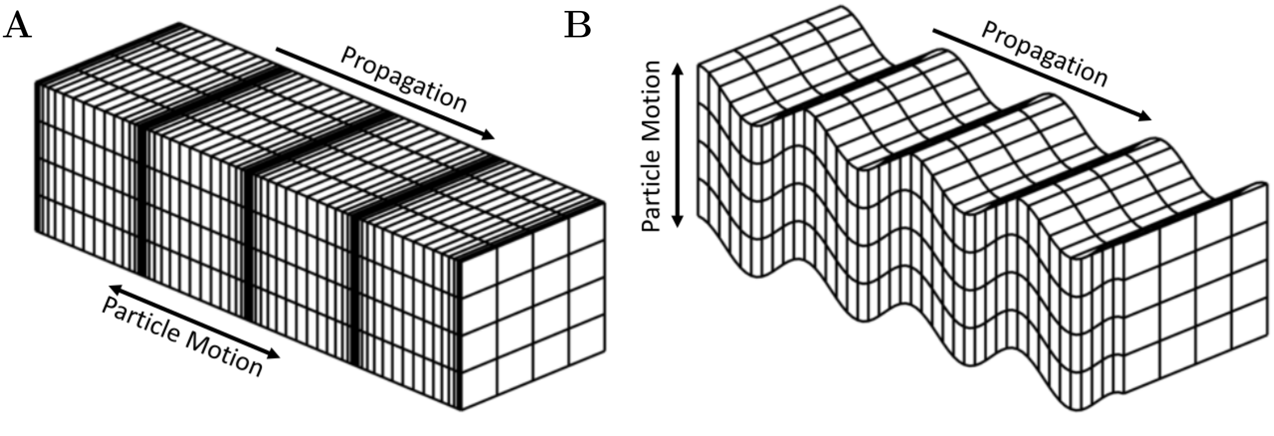

Figure 2.3: Schematic illustration of compression- and shear wave.

By applying the divergence or the curl operator, compression- and shear waves can be analyzed in separately in the form of three-dimensional wave equations.

$$\ddot{\vec{\phi}} = \frac{G^*}{\rho}\Delta\vec{\phi} = \left(c^*_{\text{shear}}\right)^2\Delta\vec{\phi} \tag{2.14}$$

$$\ddot{\vec{\psi}} = \frac{\left(H^* + \frac{4}{3}G^*\right)}{\rho}\Delta\vec{\psi} = \left(c^*_{\text{compr.}}\right)^2 \Delta\vec{\psi} \tag{2.15}$$

Here, the wave velocity is defined by the coupling constant between the spatial and temporal derivatives. The complex velocity of the shear wave c^*_{shear} is dependent on the complex shear modulus G^*, while the speed of the compression wave $c^*_{\text{compr.}}$ depends on both complex shear modulus and complex bulk modulus H^*. In the case of soft biological tissue, the $K \gg \mu$ estimate for the real-valued bulk- (K) and shear modulus (μ) from Equation 2.4 also applies to the Euclidean norms of the generalized complex moduli ($|H^*| \gg |G^*|$) [48], allowing the complex velocity of the shear and compression wave to be expressed as follows:

$$c^*_{\text{shear}} = \sqrt{\frac{G^*}{\rho}} \tag{2.16}$$

$$c^*_{\text{compr.}} = \sqrt{\frac{\left(H^* + \frac{4}{3}G^*\right)}{\rho}} \approx \sqrt{\frac{H^*}{\rho}} \tag{2.17}$$

To derive measurable compression wave speed (CWS) and shear wave speed (SWS) from the complex quantities, the real part of the complex wave vector $k^* = \omega/c^*$ with $k^* = k' + k''$ and the relation $k' = \omega/c$ are used. Together with the identities $G^* = |G^*|e^{\mathrm{i}\varphi_G}$ and $H^* = |H^*|e^{\mathrm{i}\varphi_H}$, CWS and SWS can be calculated [48, 49].

$$CWS(\omega) = \sqrt{\frac{2|H^*(\omega)|}{\rho(1 + \cos\varphi_H)}} \tag{2.18}$$

$$SWS(\omega) = \sqrt{\frac{2|G^*(\omega)|}{\rho(1 + \cos\varphi_G)}} \tag{2.19}$$

It is known from ultrasound applications that the pressure wave propagates in the human brain at a velocity of 1460 m/s to 1680 m/s, with a small difference between different tissue types [50]. In contrast, shear waves propagate through the brain at approximately 1000 times lower speed of 1 m/s to 4 m/s, with large differences between different tissue types. Therefore, imaging shear wave velocity provides good anatomical contrast for elastography purposes [50]. In ultrasound elastography, the fast pressure waves used for echo imaging are used to sample the slow deformation of tissue by shear waves, and therefore high temporal resolution of measurements can be obtained with this elastography technique.

2.5 Physiology of intracranial pressure

The main role of ICP is to regulate hemostatic processes in the brain, e.g., cerebral blood flow or maintaining the balance of interstitial fluids. In healthy adults, mean ICP varies between 5 and 15 mmHg [47]. One approach used to date to model this autoregulation is the Monro-Kellie hypothesis, in which the brain is described as a tightly packed, closed system within a semi-rigid container. The contents of the skull are thereby composed of three distinct compartments: (i) the solid brain tissue, (ii) the cerebral blood volume, and (iii) CSF [51]. While the sum of the volumes of these compartments is assumed to be constant in the healthy brain, it can change in diseases such as tumors [52], hemorrhage [3], or even age-related brain atrophy [53]. The possibility of volume change in a densely packed system is thereby given by the description of the brain as a mechanical system with variable compliance. The concept of compliance is best described by considering the variation of ICP due to the variation in blood volume through the cardiac cycle along with the exponential dependence of averaged ICP on intracranial volume, as shown schematically in Figure 2.4 [54, 47]. In this plot, the compliance can be graphically interpreted as the inverse slope of the curve. In a system with high compliance (point (i) in Figure 2.4), changes in volume can be easily compensated for by compression or redistribution of compartments, meaning that the change in blood volume with the heartbeat produces only small pressure variations, resulting in minor cardiac ICP fluctuations. In contrast, in a system with low compliance (point (ii) in Figure 2.4), compression or redistribution may be more difficult to realize, and the same variation in blood volume results in larger ICP fluctuations. Because of this effect, space-occupying diseases that increase ICP are always associated with a decrease in compliance.

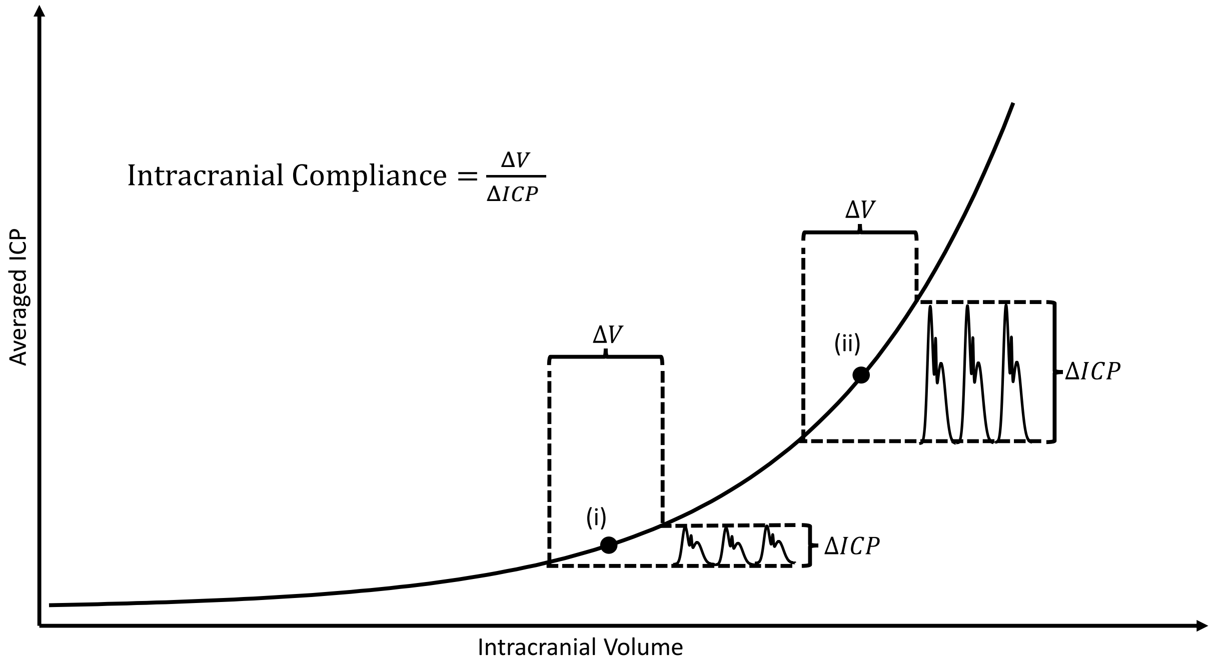

Figure 2.4: Exponential relationship between averaged ICP and intracranial volume. Figure adapted from Marmarou *et al.* [54] with friendly permission of the Journal of Neurosurgery Publishing Group.

Influence of cerebral perfusion change on ICP

ICP also varies in normal diurnal rhythm in response to physical exertion [55], gravity [56], perfusion- [8], and hydration changes [57]. It is well known that ICP can be altered in a controlled manner. One effect that has been extensively studied is the adjustment of cerebral vessel diameters in response to external stimuli, also known as cerebrovascular reactivity. For example, one such stimulus is increased partial pressure of carbon dioxide in the blood (pCO_2). Vessels respond to pCO_2 levels between 20 mmHg to 60 mmHg [58]. While normal pCO_2 in adult humans is in the range of 35 mmHg to 40 mmHg [59], values above 40 mmHg are referred to as hypercapnia and values below 35 mmHg are referred to as hypocapnia. In hypercapnia, cerebral vessels are in a vasodilated state, while vasoconstriction occurs in hypocapnia. In clinical practice, hypercapnia can be artificially induced to test cerebrovascular reactivity using CO_2-enriched gases. Hypocapnia is commonly used in ventilated patients to decrease ICP and prevent cerebral hypo-perfusion [45, 60, 58].

Alteration of cerebral blood flow can also be induced by varying hydration. Because the brain has a large water content of 75 % [61], hypotonic dehydration and subsequent rehydration by oral water intake, as often occurs during the diurnal cycle, also results in volume shifts between different brain compartments. During dehydration, osmotic gradients transport water from the intracellular compartment within the brain parenchyma into the blood compartment to compensate for a decrease in perfusion [62], leading to a decrease in brain tissue volume [63, 64] and consequently lowering ICP. This effect is used clinically in the form of drug-induced cerebral dehydration, also referred to as hyperosmolar therapy, in patients with elevated ICP and cerebral edema [65]. Oral rehydration, on the other hand, increases brain perfusion and thus ICP and is used clinically to treat intracranial hypotension, which is a common side effect of CSF removal [66].

Influence of CSF removal on ICP

The CSF compartment is the target of acute clinical therapy in patients with elevated ICP and is usually achieved by a combination of invasive ICP monitoring and a CSF drainage system [67]. CSF drainage lowers ICP immediately and is therefore an effective, albeit symptomatic, intervention for patients in critical condition at acute risk for neurologic impairment. However, permanent monitoring of ICP is not always necessary, for example, in patients with IIH, characterized by elevated ICP of unknown etiology [68]. In this case, CSF can also be drained by lumbar puncture, where a drainage needle is inserted into the lumbar spinal canal. Spot measurement of CSF opening pressure, which is used as a surrogate for ICP, can also be performed during LP by attaching a manometer to the drainage catheter.

Relationship of ICP and tissue stiffness

Under in vivo conditions, CS is influenced by both static and dynamic factors. While static factors such as the structural integrity of the cellular matrix, which is compromised in diseases such as multiple sclerosis and Altzheimer's disease [69, 70, 71], have been studied for some time using MRE, dynamic contributions to CS such as perfusion, brain activation, and solid-fluid interactions between compartments in the brain are increasingly becoming the focus of research [72, 73, 74, 75]. The link between CS and cerebral perfusion is an important indication that ICP fluctuations could be detected noninvasively using MRE or ultrasound elastography. This hypothesis is further supported by recent studies, where perfusion- and pressure-related stiffness changes were found *in vivo* in liver, spleen, and kidney [41, 38, 76].

3. Materials and Methods

For data acquisition, I used an optimized version of the abdominal THE setup as described in Tzschätzsch *et al.* [32], which I adapted for transtemporal data acquisition. During the project, I optimized the system several times with respect to B-mode resolution as well as penetration depth. The following section briefly describes the current experimental setup for data acquisition and the post-processing pipeline. The experimental setup explained in the following was previously reported in several articles [32, 41, 77, 78, 79].

3.1 Experimental setup

Data acquisition

The basic experimental setup, as shown in Figure 3.1, consisted of three main components: (i) a custom-built examination bed with a vibration unit consisting of a vibration plate with an amplifier underneath (GAMT, Merseburg, Germany), (ii) a clinical ultrasound scanner for radiofrequency (RF) data acquisition (SonixMDP, UltraSonix, Scottsdale AZ, USA) equipped first with a convex transducer (C5-2/60, 2 MHz), which was later replaced by a phased transducer (SA4-2/24, 3.3 MHz), and (iii) the elastography computer for post-processing and visualization of the data. Volunteers were placed in the supine position with the vibration plate under the back of the head. A tailored waveform with a total of six frequencies in the audible range (27, 33, 39, 44, 50, and 56 Hz) was fed into the amplifier to generate shear waves within the brain. Inspired by transcranial Doppler examinations conducted in clinical routine, the temporal bone window located between the eye and ear was used for ultrasound measurements through the intact skull, as shown in the magnification in Figure 3.1. In this measurement position, RF data were recorded during harmonic vibration of the head at a frame rate of 80 Hz over one second and transmitted to the elastography computer for real-time post-processing.

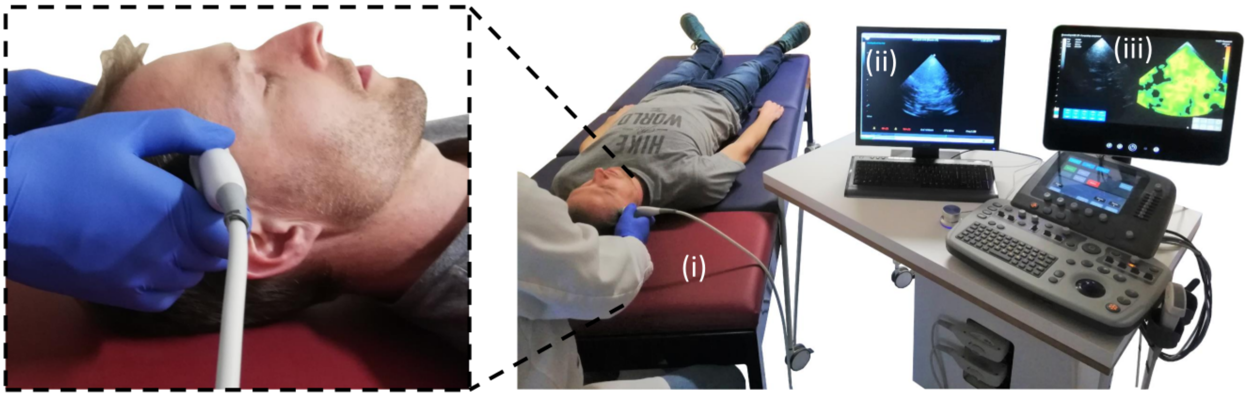

Figure 3.1: Experimental setup for cerebral THE. Adapted from Kreft *et al.* [78].

Post-processing

Since a detailed description of the post-processing is beyond the scope of this work, only the most important steps are explained below. The algorithm used here was developed by Tzschätzsch *et al.* [80] and is called k-Multifrequency Dual Elasto-Visco inversion (k-MDEV). This algorithm is capable of reconstructing wavenumbers of multifrequency shear waves propagating from different directions and generating a composite map of shear wave speed with a spatial resolution of 0.5 mm. The individual post-processing steps are shown chronologically in the flowchart in Figure 3.2.

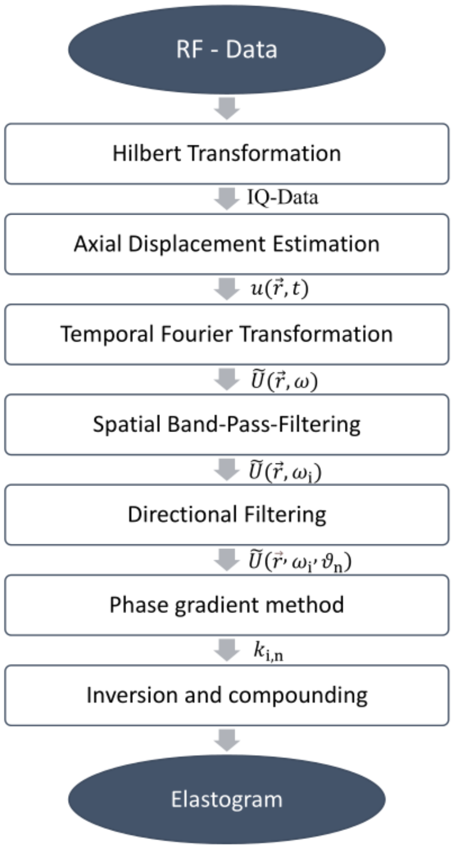
RF - Data
Hilbert Transformation
IQ-Data
Axial Displacement Estimation
$u(\vec{r},t)$
Temporal Fourier Transformation
$\widetilde{U}(\vec{r},\omega)$
Spatial Band-Pass-Filtering
$\widetilde{U}(\vec{r},\omega_\mathrm{i})$
Directional Filtering
$\widetilde{U}(\vec{r},\omega_\mathrm{i},\vartheta_\mathrm{n})$
Phase gradient method
$k_{\mathrm{i,n}}$
Inversion and compounding
Elastogram

Figure 3.2: Flowchart of the post-processing pipeline.

First, the axial Hilbert transform was applied to the real-valued RF data to produce complex-valued in-phase quadrature (IQ) data for each acquired image. The axial displacement field $u(\vec{r},t)$ was then estimated at each location $\vec{r}$ and at each time t of the measurement by calculating the spatially resolved phase shift between adjacent images. In the following step, the multifrequency displacement field $u(\vec{r},t)$ was decomposed into complex wavefields $\widetilde{U}(\vec{r},\omega)$ at the excitation frequencies using temporal Fourier transform. The upper half of the vibration frequencies, which were above the Nyquist limit ($f_\mathrm{N} = 1/2$ Frame Rate $=$ 40 Hz), appeared aliased in the frequency spectrum at positions 24 Hz ($\widehat{=}$ 56 Hz), 27 Hz, 30 Hz ($\widehat{=}$ 50 Hz), 33 Hz, 36 Hz ($\widehat{=}$ 44 Hz), but were further processed according to their unaliased positions. This type of stroboscopic sampling is called controlled aliasing [32]. Figure 3.3A schematically shows the waveform fed into the amplifier along with the resulting frequency spectrum.

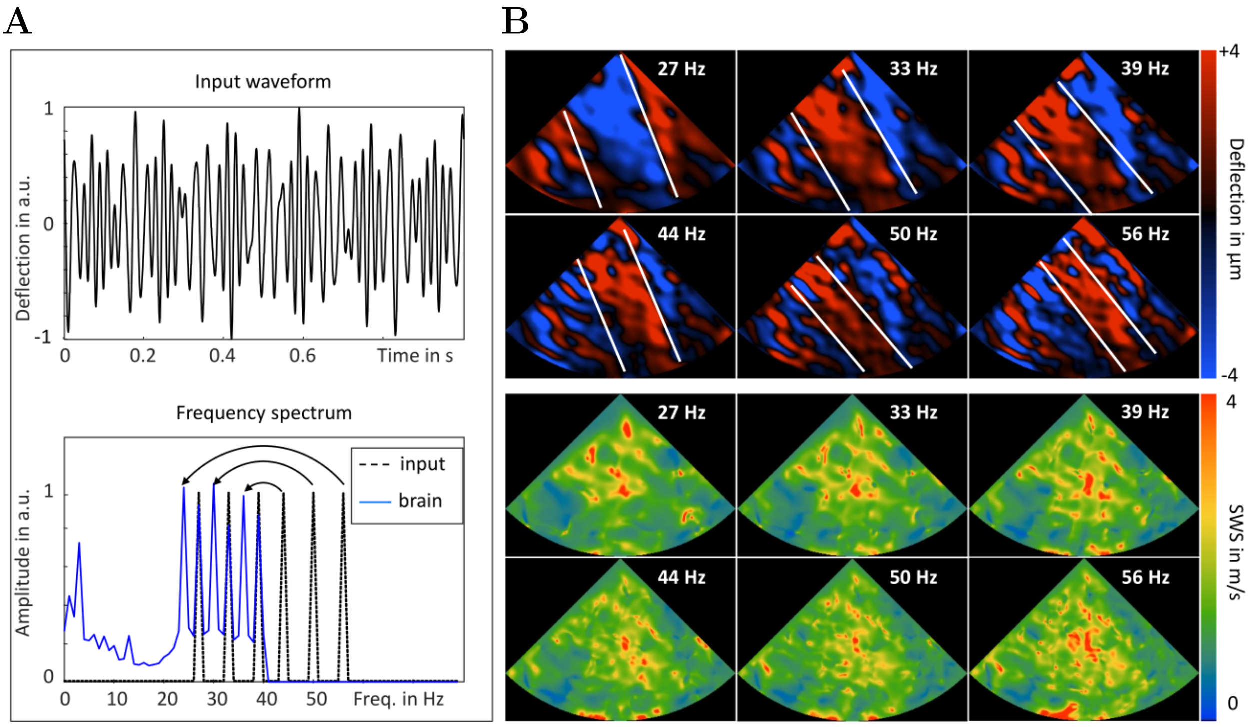

Figure 3.3: Multifrequency waveform and the resulting frequency spectrum along with frequency-resolved shear wave fields and elastograms. Adapted from Tzschätzsch *et al.* [41].

The extraction of the shear waves $\widetilde{U}(\vec{r},\omega_i)$ for each frequency ω_i was then performed in k-space by applying a two-dimensional bandpass filter $\zeta(|k|)$ to the complex wavefields.

$$\zeta(|k|) = \frac{|k|}{\sigma_{|k|}\sqrt{2\pi}} e^{\frac{|k|}{\sqrt{2}\sigma_{|k|}}} \tag{3.1}$$

Here, $|k| = \sqrt{k_x^2 + k_y^2}$ was the radial vector in k-space and $\sigma_{|k|}$ was the width of the filter. After bandpass filtering, the shear wavefield still consisted of a superposition of multidirectional waves due to reflection and refraction at different interfaces in the brain tissue and skull bone. Since the k-MDEV algorithm was designed for plane waves, the next step was to apply a cone-shaped directional filter $\xi(\vartheta_n)$ in 8 directions [81].

$$\xi(\vartheta_n) = \frac{1}{\sigma_\vartheta\sqrt{2\pi}} e^{-\left(\frac{\vartheta-\vartheta_n}{\sqrt{2}\sigma_\vartheta}\right)} \qquad \text{for } n = 1,\ldots,8 \tag{3.2}$$

In this filter, $\vartheta = \arg(k_x + \mathrm{i}k_y)$ describes the phase angle in complex k-space. The shear wave fields for all vibration frequencies corresponding to a selected direction are shown in Figure 3.3B. The wavefields $\widetilde{U}(\vec{r},\omega_i,\vartheta_n)$ were then used to calculate the respective wavenumber $k_{i,n}$ for each frequency ω_i and each direction ϑ_n. For this purpose, the phase gradient method was used [80].

$$k_{i,n} = \left\|\nabla\arg\left(\widetilde{U}(\vec{r},\omega_i,\vartheta_n)\right)\right\| \tag{3.3}$$

Finally, $\mathrm{SWS}_{i,n} = \omega_i / k_{i,n}$ was calculated by inversion of the wave numbers $k_{i,n}$. Amplitude-weighted harmonic averaging was used to create a single multifrequency multidirectional elastogram. This type of averaging ensured that waves with low amplitude and high noise content had less influence on the result. In addition to this, a threshold of 1 m/s was applied to the composite elastogram to exclude regions which still showed low signal-to-noise ratio from further analysis. Figure 3.4 shows a reconstructed B-mode image along with a composite elastogram of one measurement. Typical anatomical landmarks within the B-Mode image included (i) the dura, (ii) the temporal lobe parenchyma, (iii) the basal cisterns around (iv) the mesencephalic brainstem and could also be moderately delineated in the elastograms.

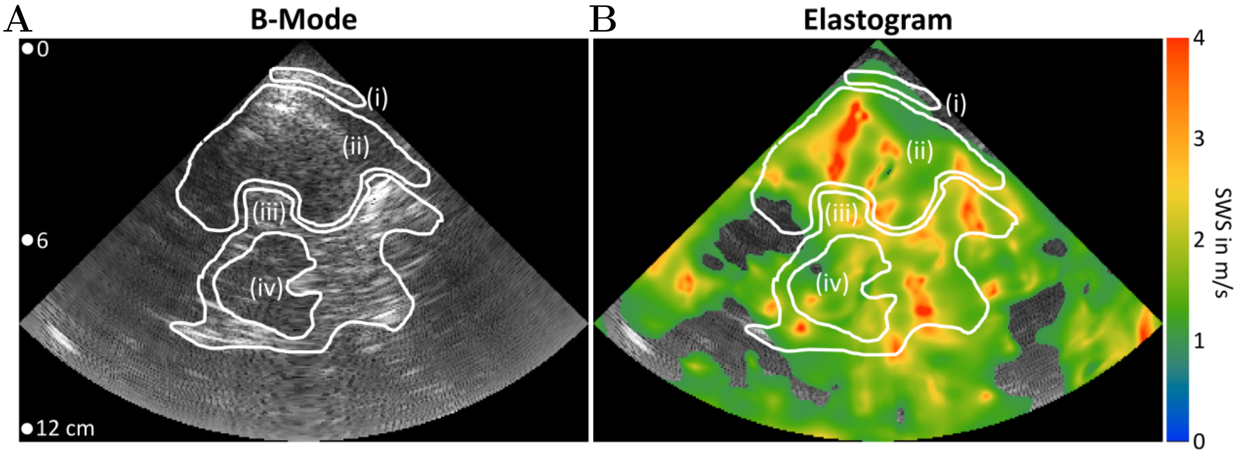

Figure 3.4: Representative B-mode image along with corresponding elastogram.

The region of interest (ROI) around the temporal lobe parenchyma (ii) was manually drawn and analyzed by averaging all values within the ROI to obtain a stable and representative SWS value for each measurement. This initial step of data analysis was used for all studies described in the following section.

3.2 Studies on healthy volunteers

In total, I performed two experiments on healthy volunteers. The aim was to change the ICP by manipulation of cerebral perfusion. All study protocols were in accordance with the Declaration of Helsinki and were approved by the Institutional Review Board of the Charité - Universitätsmedizin Berlin (EA1/242/18). Written informed consent was obtained from all study participants. None of the participants had a history of psychiatric disorders or a recent severe head injury.

Hypercapnia

To test the effect of increased CO_2 respiration on CS, a total of 10 healthy volunteers (5/5 women/men, mean age: 29 ± 6 years, age range: 20 to 41 years) were measured continuously for 22 minutes during artificially induced hypercapnia in one session. For this purpose, the volunteers breathed slightly increased amounts of carbon dioxide using an airtight breathing mask connected to a gas cylinder filled with carbogen (Linde, Pullach, Germany), a gas comprised of 5 % CO_2 and 95 % O_2. The complete setup of the measuring station is shown in Figure 3.5.

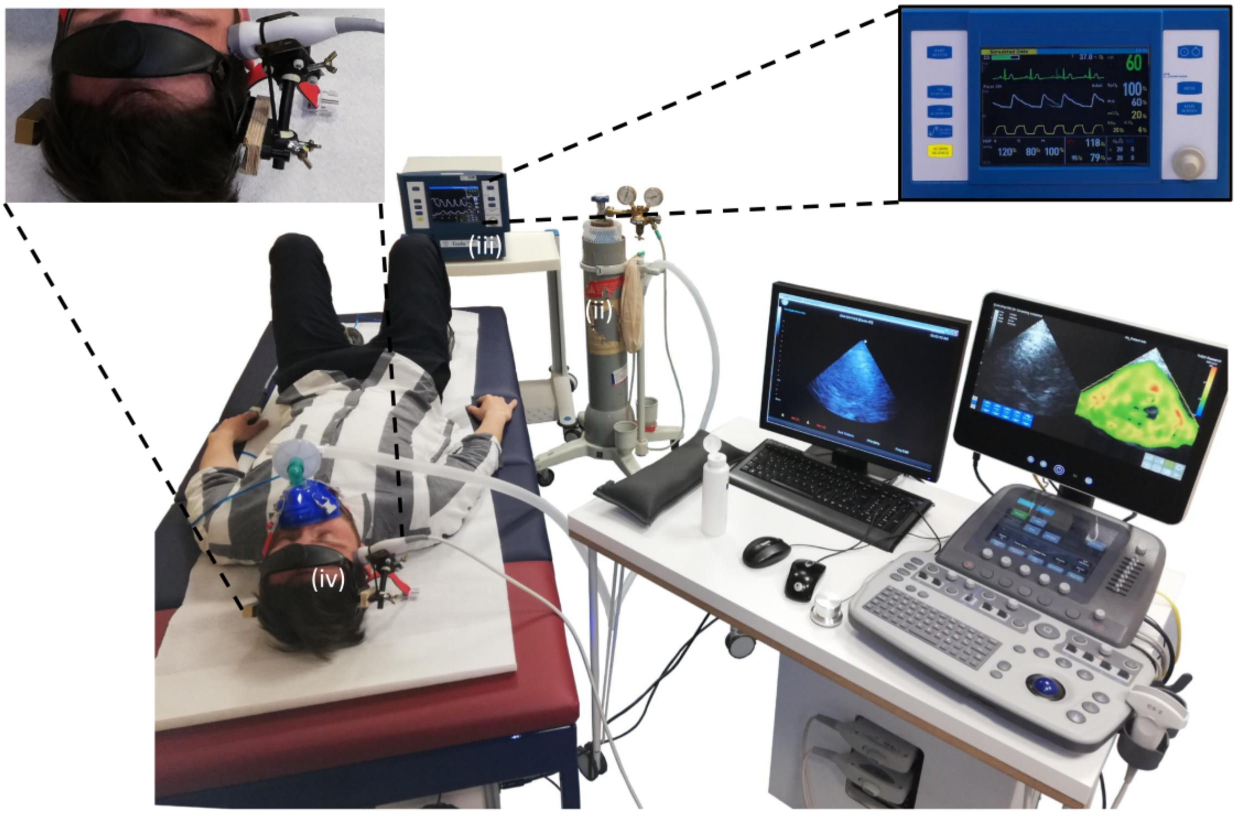

Figure 3.5: Measurement setup for hypercapnia experiment. Figure adapted from Kreft *et al.* [77] with friendly permission of Elsevier Publishers.

Since such a long measurement is strenuous for both the volunteer and the person performing the investigation, involuntary movements of the transducer relative to the temples affected the stability of the measurement. Therefore, a specially designed mounting device, as shown in the top-left magnification in Figure 3.5, was used to attach the transducer to the volunteer's head and thus minimize the measurement errors. One measurement session was divided into three phases of 7 minutes each. The complete study design is illustrated in the flowchart in Figure 3.6.

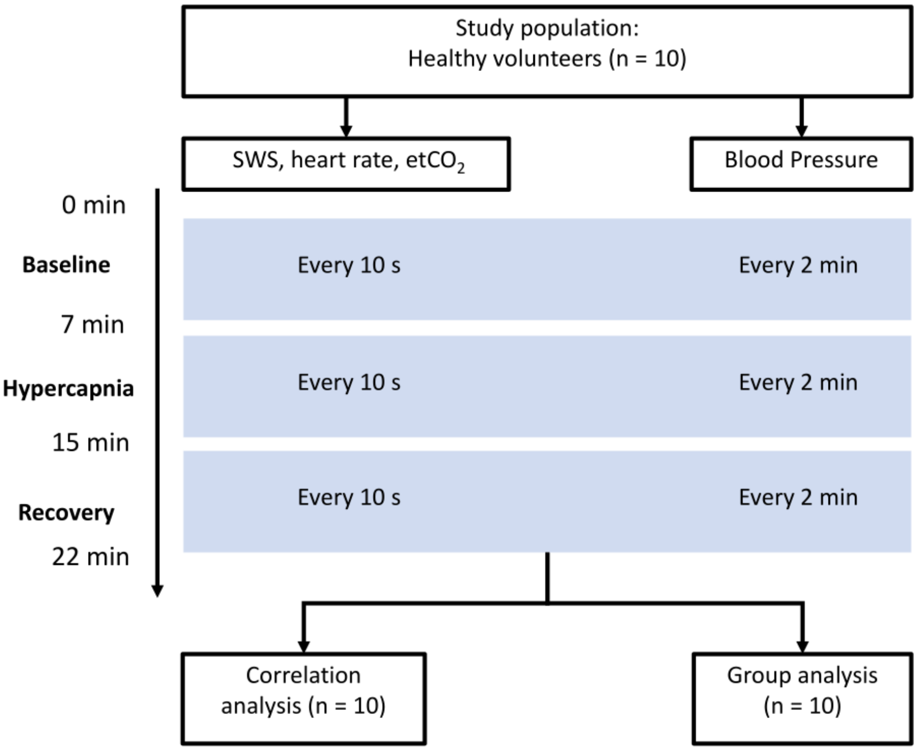
Study population:
Healthy volunteers (n = 10)
SWS, heart rate, etCO2
Blood Pressure
0 min
Baseline
7 min
Hypercapnia
15 min
Recovery
22 min
Every 10 s
Every 2 min
Every 10 s
Every 2 min
Every 10 s
Every 2 min
Correlation analysis (n = 10)
Group analysis (n = 10)

Figure 3.6: Flowchart diagram of the hypercapnia study design.

The first phase was the baseline phase, in which the volunteer was already wearing the mask but was breathing ambient air. The second phase was the hypercapnia phase. Here the breathing mask was connected to the carbogen supply and hypercapnia was induced. In the third phase, the recovery phase, the gas supply was disconnected, and the volunteers breathed normal ambient air again. In each volunteer, SWS, heart rate, and expiratory CO_2 content ($etCO_2$) were measured every 10 seconds using a clinical patient monitor (Tesla Guard, Mammendorf, Germany), as shown in the top-right magnification in Figure 3.5. In addition, blood pressure was measured every 2 minutes. Because the gas cylinder had to be connected and disconnected, there was a 30-second pause in measurement between each phase. Within the temporal lobe parenchyma, a single ROI was determined for each volunteer as described in Section 3.1. Time-resolved curves were plotted for SWS and $etCO_2$. The time points of increase (τ_i) or decrease (τ_d) in SWS and $etCO_2$ were determined using a sigmoidal shape fitting function $f(t)$.

$$f(t) = \mathrm{SWS_{BL}} + \frac{\mathrm{SWS_P} - \mathrm{SWS_{BL}}}{1 + e^{S_\mathrm{i}(t-\tau_\mathrm{i})} + e^{S_\mathrm{d}(t-\tau_\mathrm{d})}} \tag{3.4}$$

In this function, $\mathrm{SWS_{BL}}$ represents the baseline value, $\mathrm{SWS_P}$ represents the plateau value, and $\mathrm{S_i}$ and $\mathrm{S_d}$ represent the slopes of the increase or decrease in the curve. For each phase, the last 25 measurement points were aggregated for each volunteer. These aggregated data were then tested for statistical differences using a paired *t*-test. In addition, a paired *t*-test was performed to detect statistical differences in the time of increase τ_i and time of decrease τ_d between SWS and $etCO_2$. Because they represent the temporal response of the effective medium, including the vascular bed, to hypercapnia, these parameters are considered important in terms of cerebrovascular response. All p-values less than 0.05 were considered statistically significant.

De- and Rehydration

To determine the effects of hydration status on CS, a total of 12 healthy volunteers (3/9 women/men, mean age: 33 ± 9 years, age range: 22 to 50 years) were measured 10 times each in 6 sessions within two consecutive days. The experimental procedure is shown in Figure 3.7.

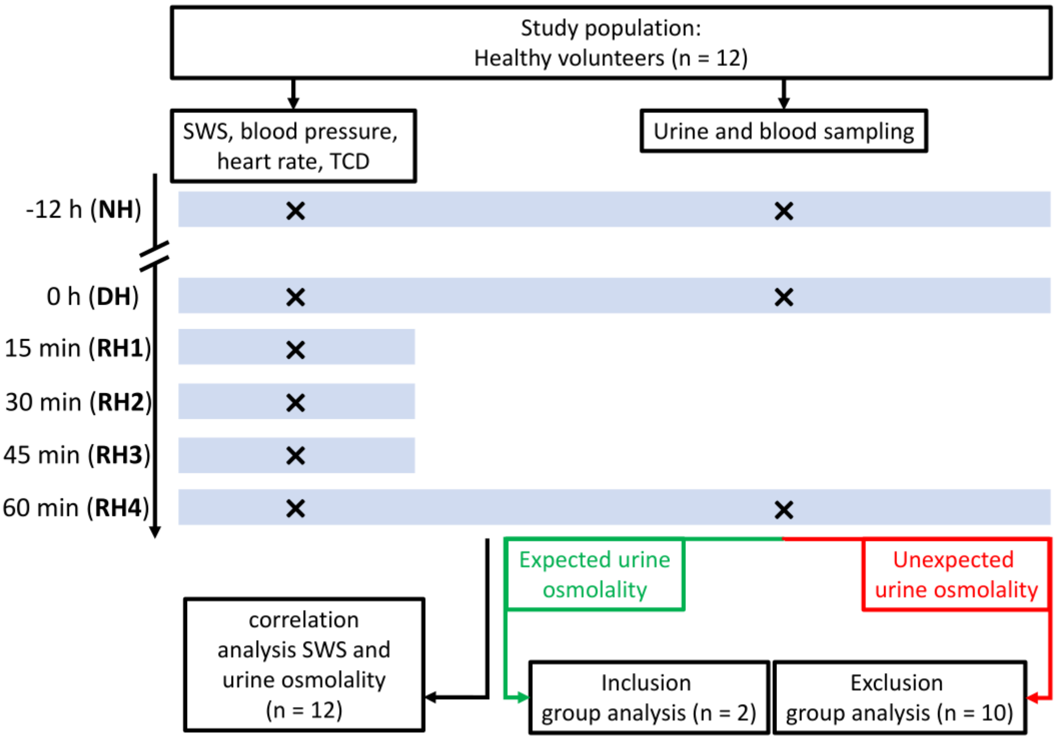
Study population:
Healthy volunteers (n = 12)
SWS, blood pressure, heart rate, TCD
Urine and blood sampling
-12 h (NH)
0 h (DH)
15 min (RH1)
30 min (RH2)
45 min (RH3)
60 min (RH4)
Expected urine osmolality
Unexpected urine osmolality
correlation analysis SWS and urine osmolality (n = 12)
Inclusion group analysis (n = 2)
Exclusion group analysis (n = 10)

Figure 3.7: Flowchart diagram of the dehydration study design. Adapted and modified from Kreft *et al.* [78].

The first measurement under normal hydration (NH) was performed on day 1 after a regulated fluid intake of 1.5 litres of water over a 5-hour period. After this measurement, volunteers spent the night without food and fluid intake for 12 hours. The second measurement was performed on day 2 in the dehydrated state (DH). After this session, volunteers drank 12 ml/kg of water within 15 minutes according to their body weight. Immediately after drinking, volunteers were measured four additional times during rehydration (RH1-4) at 15-minute intervals. Heart rate, blood pressure, blood flow velocity in the middle cerebral artery by transcranial Doppler, and 10 SWS measurements were recorded at each session. In the NH, DH, and RH4 sessions, urine samples were collected, and a small blood count was obtained to determine urine osmolality and hematocrit. For each volunteer and session, an ROI was manually drawn in the temporal parenchyma as described in Section 3.1, and 10 SWS values were determined. These 10 SWS values were then averaged to yield 6 representative SWS values for each volunteer (one for each session). Statistically significant differences in SWS between sessions were determined using a one-way ANOVA. Possible correlations between the identified parameters were calculated using the Pearson correlation coefficient. In addition, sessions were compared by group analysis using a paired *t*-test. All *p*-values below 0.05 were considered significant. While all 12 volunteers were included in the correlation analysis, only 10 volunteers were included in the group statistics because two volunteers did not follow the dehydration protocol. This was determined by the trajectories of their urine osmolality and verbal testimony of the volunteers.

3.3 Clinical patient study

To conclude my project, I determined the dependence of noninvasively measured SWS on invasively measured ICP within a clinical pilot study. In this study, 22 patients (17/5 women/men, mean age: 34 ± 11 years, age range 22 to 55 years) who met the preliminary diagnostic criteria for IIH such as headache, papilledema, and visual field defects, were examined in 2 sessions consisting of 20 measurements each using cerebral THE. The complete procedure of the experiment is shown in Figure 3.8.

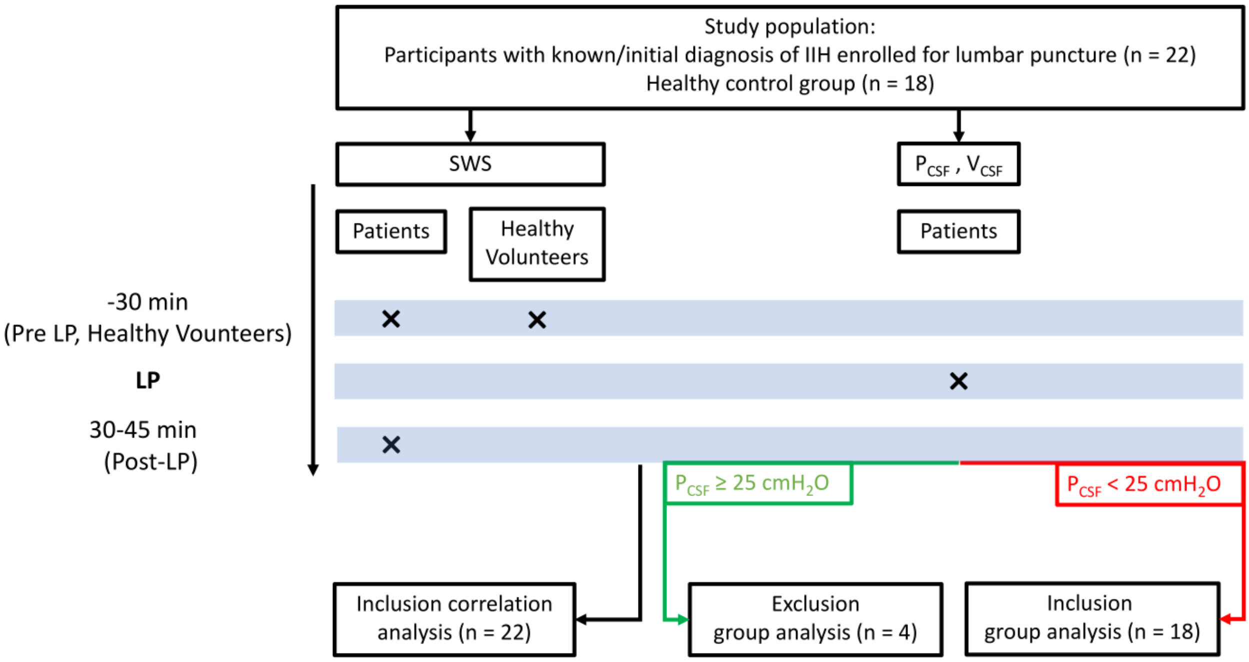
Study population:
Participants with known/initial diagnosis of IIH enrolled for lumbar puncture (n = 22)
Healthy control group (n = 18)
SWS
P_{CSF}, V_{CSF}
Patients
Healthy Volunteers
Patients
-30 min
(Pre LP, Healthy Vounteers)
LP
30-45 min
(Post-LP)
×
×
×
×
$P_{CSF} \geq 25$ cmH$_2$O
$P_{CSF} < 25$ cmH$_2$O
Inclusion correlation analysis (n = 22)
Exclusion group analysis (n = 4)
Inclusion group analysis (n = 18)

Figure 3.8: Flowchart diagram of the IIH study design. Figure adapted and modified from Kreft *et al.* [79] with friendly permission of Wolters Kluwer Health Publishers.

Here, the first session was performed under the assumption of an elevated ICP. Before the second session, patients received treatment in the form of LP with an atraumatic needle (Pajunk Sprotte Lumbar, Pajunk GmbH Medizintechnologie, Geising, Germany). During LP, invasive measurement of CSF opening pressure (P_{CSF}) was also performed with a manometer (Mediplast Optidynamic Spinal Fluid Manometer, Gazzo Veronese, Italy). The entire procedure was performed in the supine position to avoid distortion of P_{CSF} measurements by gravity. When necessary, CSF was drained from the spinal canal, and the drained CSF volume (V_{CSF}) was recorded. After 30 to 45 minutes, the second session of cerebral THE was then performed in each patient. Because the necessary criterion for the diagnosis of IIH is based on quantification of P_{CSF}, 4 patients were further excluded from the group analysis because they fell below the clinical threshold for definitive IIH diagnosis (25 cmH_2O). In addition to the patient cohort, an age-matched control cohort of 18 healthy volunteers (9/9 women/men, mean age 33 ± 9 years, age range: 20 to 47 years) was examined 20 times with cerebral THE in one session.

The 20 measurements for each session were averaged to obtain a representative SWS value for healthy volunteers as well as for patients before and after LP. A paired t-test was used to test for statistical differences between the mean SWS values within the patient cohort, whereas an unpaired t-test was used to test for statistical differences between the patient cohort and healthy control volunteers. The diagnostic performance of cerebral THE was tested by receiver operating characteristic analysis with a P_{CSF} cutoff of 25 cmH_2O for pathologically elevated ICP. The 4 patients who did not meet the final criterion for IIH were excluded from this part of the statistical analysis but were included in the correlation analysis because P_{CSF} quantification was also performed in these patients. In the correlation analysis, Pearson's linear correlation coefficient was used to compare pre-LP SWS with P_{CSF} and V_{CSF}. In addition, P_{CSF} and V_{CSF} were compared separately.

4. Results

4.1 Studies on healthy volunteers

In the following, the results of the studies on healthy volunteers, including the hypercapnia experiment and the de- and rehydration experiment as well as the results of the pilot clinical study are described in the scope of this project. More detailed reports can be found in [77, 78, 79].

Hypercapnia

Representative elastograms of one volunteer from each of the three phases of the study are shown in Figure 4.1. The increase in SWS during hypercapnia can be seen within the temporal lobe parenchyma (delineated by a white line) in the middle elastogram (Figure 4.1B) as a shift in the color map to the red region.

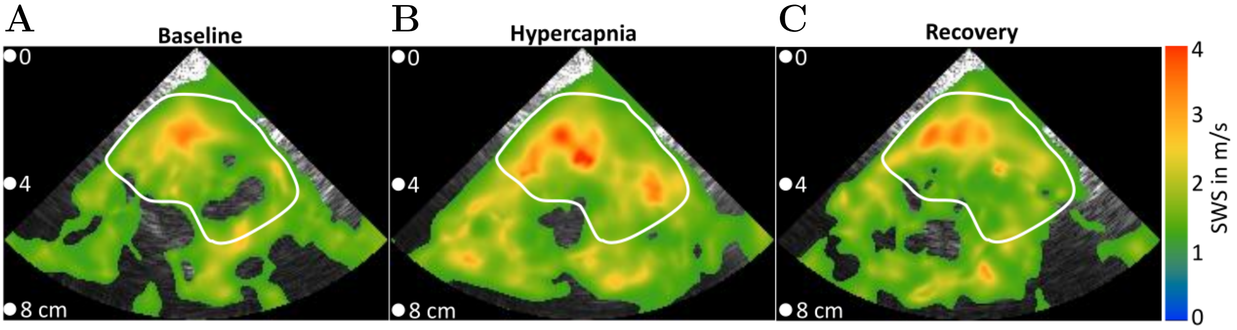

Figure 4.1: Representative elastograms of one volunteer during baseline, hypercapnia, and recovery phase. Figure adapted from Kreft *et al.* [77] with friendly permission of Elsevier Publishers.

Boxplots of SWS averaged over the second halves of the baseline, hypercapnia, and recovery phases are shown in Figure 4.2A. During the hypercapnia phase, SWS values were higher compared to baseline and recovery ($p = 0.001$), while no difference was detected between SWS values in baseline and recovery ($p = 0.13$). During hypercapnia, SWS values increased in all volunteers, with an average increase of $0.09 \pm 0.06\,\mathrm{m/s}$. The time-resolved group means and standard deviations of SWS (blue) and $\mathrm{etCO_2}$ (red) are shown in Figure 4.2B. During the early phase of hypercapnia at $\tau_{\mathrm{i,SWS}} = 2.2 \pm 2.0$ minutes, baseline SWS increased from $1.57 \pm 0.04\,\mathrm{m/s}$ to plateau values of $1.66 \pm 0.05\,\mathrm{m/s}$ (relative SWS change: $5.9 \pm 4.0\,\%$, $p = 0.001$). From this plateau, SWS decreased to normal values of $1.59 \pm 0.03\,\mathrm{m/s}$ ($p = 0.003$) in the early recovery phase at $\tau_{\mathrm{d,SWS}} = 3.6 \pm 1.5$ minutes. A similar trend was observed for $\mathrm{etCO_2}$. From a baseline $\mathrm{etCO_2}$ of $32 \pm 3\,\mathrm{mmHg}$, it increased to plateau values of $42 \pm 2\,\mathrm{mmHg}$ in the early hypercapnia phase at $\tau_{\mathrm{i,CO2}} = 1.9 \pm 1.3$ minutes (relative $\mathrm{etCO_2}$ change: $29.1 \pm 8.6\,\%$, $p < 0.001$). From this plateau, $\mathrm{etCO_2}$ returned to baseline values without significant delay at $\tau_{\mathrm{d,CO2}} = 0.9 \pm 0.4$ minutes after the gas supply was interrupted. While SWS and $\mathrm{etCO_2}$ increased with similar τ_{i} ($p = 0.48$), $\mathrm{etCO_2}$ returned to normal values 2.7 minutes earlier than SWS ($p < 0.001$).

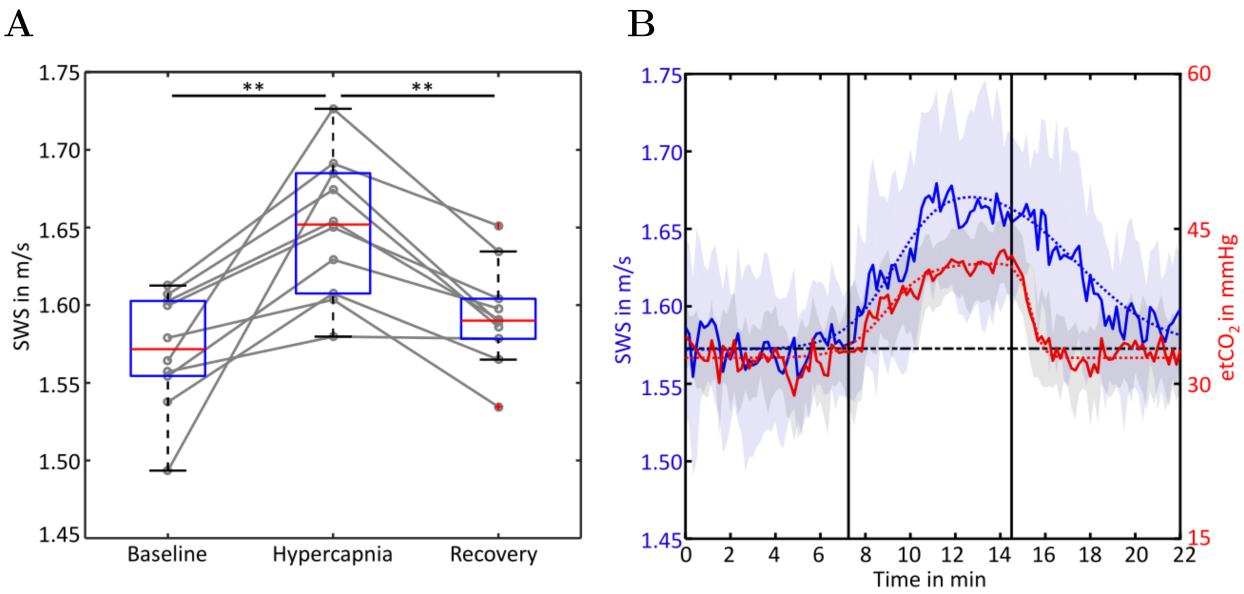

Figure 4.2: Statistical boxplot of the hypercapnia data along with time resolved mean SWS and mean etCO$_2$. Figure adapted from Kreft *et al.* [77] with friendly permission of Elsevier Publishers.

De- and Rehydration

Figure 4.3 shows representative elastograms of one volunteer under (A) normally hydrated (NH), (B) dehydrated (DH), and (C) rehydrated (RH4) conditions. The decreased SWS in the dehydrated condition (Figure 4.3B) within the temporal lobe parenchyma (delineated by white line) is visible here as a shift of the SWS map towards green colors.

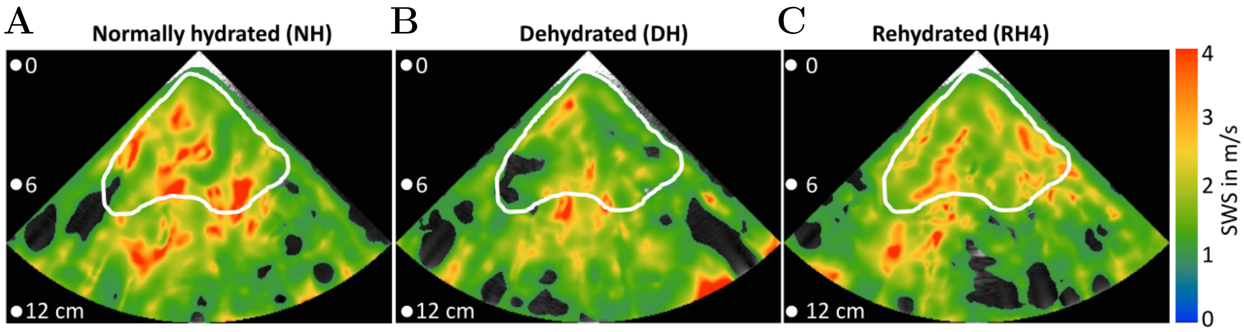

Figure 4.3: Representative elastograms of one volunteer in normally hydrated, dehydrated, and rehydrated states. Figure adapted from Kreft *et al.* [78].

The trajectories of mean SWS and urine osmolality throughout the experiment are shown in Figure 4.4. It was found that SWS (Figure 4.4A) decreased from normal hydration to dehydration (NH to DH) from $1.64 \pm 0.02\,\mathrm{m/s}$ to $1.57 \pm 0.04\,\mathrm{m/s}$ ($p < 0.001$). Approximately 30 minutes after water intake on day 2 (RH2), SWS increased again to $1.62 \pm 0.02\,\mathrm{m/s}$ ($p < 0.001$) and remained unchanged at this value for another 30 minutes. Plateau values were similar to those during normal hydration (all p-values > 0.9). In contrast to SWS, urine osmolality (Figure 4.4B) increased from a normal hydration value of $320 \pm 150\,\mathrm{mOsm/kg}$ to $780 \pm 110\,\mathrm{mOsm/kg}$ in the dehydrated state ($p < 0.001$). After water drinking, urine osmolality decreased to $290 \pm 130\,\mathrm{mOsm/kg}$ ($p < 0.001$), which corresponded to normal hydration levels ($p = 0.83$). Two volunteers, who are specifically identified in Figure 4.4, did not comply with the fasting protocol. Figure 4.4B shows the striking trend in urine osmolality during the experiment for these two volunteers. They were therefore excluded from the statistical group analysis.

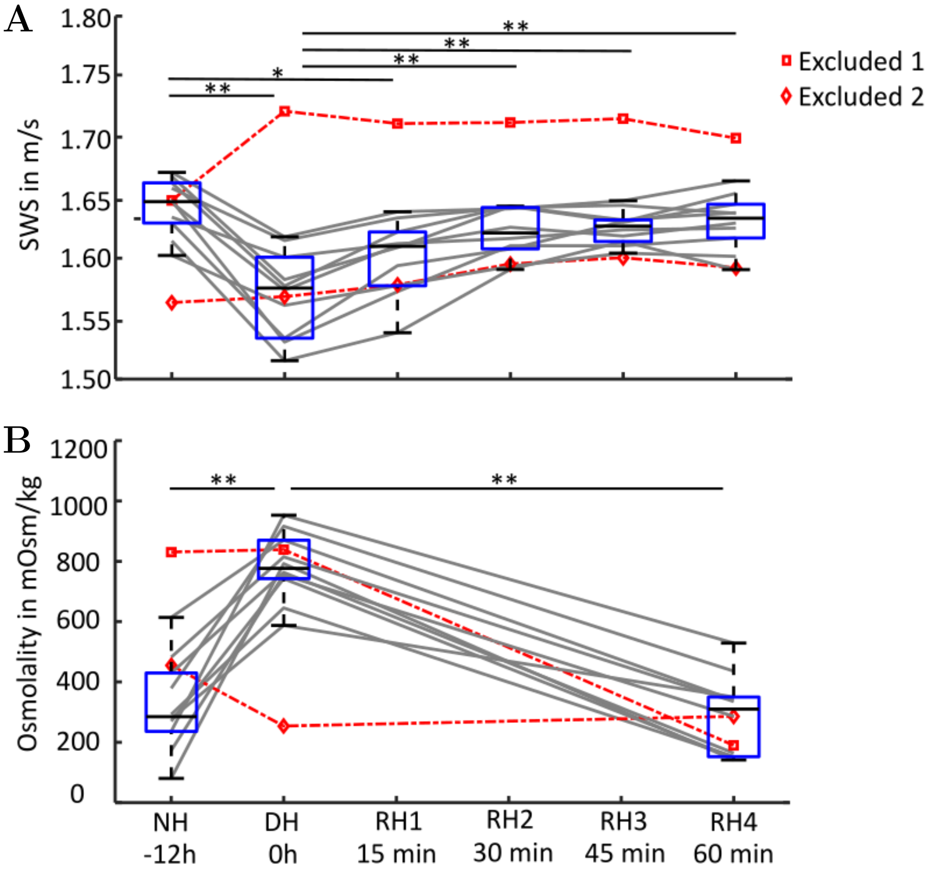

Figure 4.4: Boxplots of SWS and urine osmolality during de- and oral rehydration. Figures adapted from Kreft *et al.* [78].

In contrast to the group analysis, no volunteer was excluded from the correlation analysis because all received quantification of urine osmolality and hematocrit. A linear correlation was observed between SWS and urine osmolality ($r = -0.68$, $p < 0.001$), as shown in the scatter plot in Figure 4.5. Blood pressure, heart rate, cerebral blood flow velocity, and hematocrit values did not change with hydration and were not correlated with SWS.

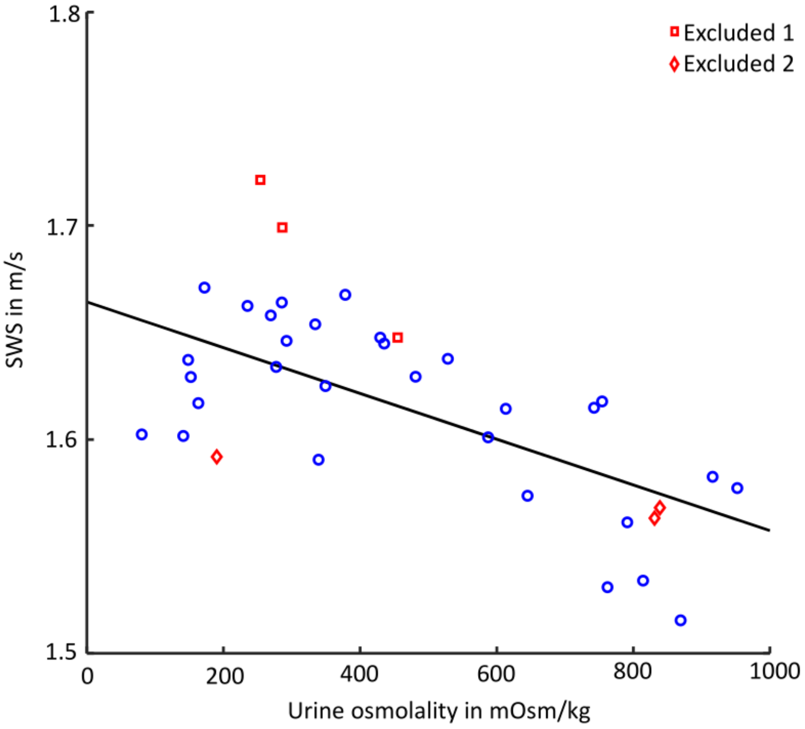

Figure 4.5: Scatter plot of SWS and urine osmolality. Figure adapted from Kreft et al. [78].

4.2 Clinical patient study

Figure 4.6 shows the representative elastograms of a (A) healthy volunteer and a patient (B) before and (C) after LP. Within the temporal lobe parenchyma (delineated by a white line), the difference in SWS between healthy volunteers and patients with IIH on the one hand (Figure 4.6A to B), and the decrease in SWS within the patient cohort due to CSF withdrawal on the other hand (Figure 4.6B to C) can be seen.

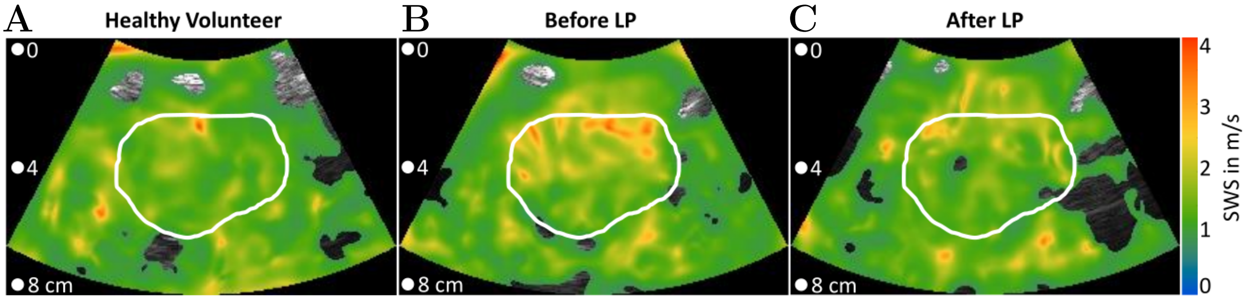

Figure 4.6: Representative elastograms of one healthy volunteer one patient before and after LP. Figure adapted from Kreft et al. [79] with friendly permission of Wolters Kluwer Health Publishers.

Boxplots of mean SWS in healthy volunteers as well as patients before and after LP are shown in Figure 4.7A. Mean baseline SWS of healthy volunteers was $1.55 \pm 0.08\,\mathrm{m/s}$, whereas it was significantly increased in patients before LP with $1.81 \pm 0.10\,\mathrm{m/s}$ ($p < 0.001$). Approximately 30 to 45 minutes after LP, a decrease in SWS of $16 \pm 5\,\%$ to $1.56 \pm 0.06\,\mathrm{m/s}$ was observed in patients ($p < 0.001$). No difference was observed when comparing the SWS of patients after LP with the SWS of healthy volunteers ($p = 0.60$). Additionally, the four patients who did not meet the pathological threshold of $P_{\mathrm{CSF}} = 25\,\mathrm{cmH_2O}$ showed SWS values in the range of healthy volunteers previous to LP and could be identified by cerebral THE, as indicated by the red lines in Figure 4.7A. The diagnostic performance of cerebral THE, derived by receiver operating characteristic analysis and shown in Figure 4.7B, revealed a SWS cutoff value of 1.67 m/s with a specificity of 94 % and a sensitivity of 100 % for increased CSF pressure above $25\,\mathrm{cmH_2O}$.

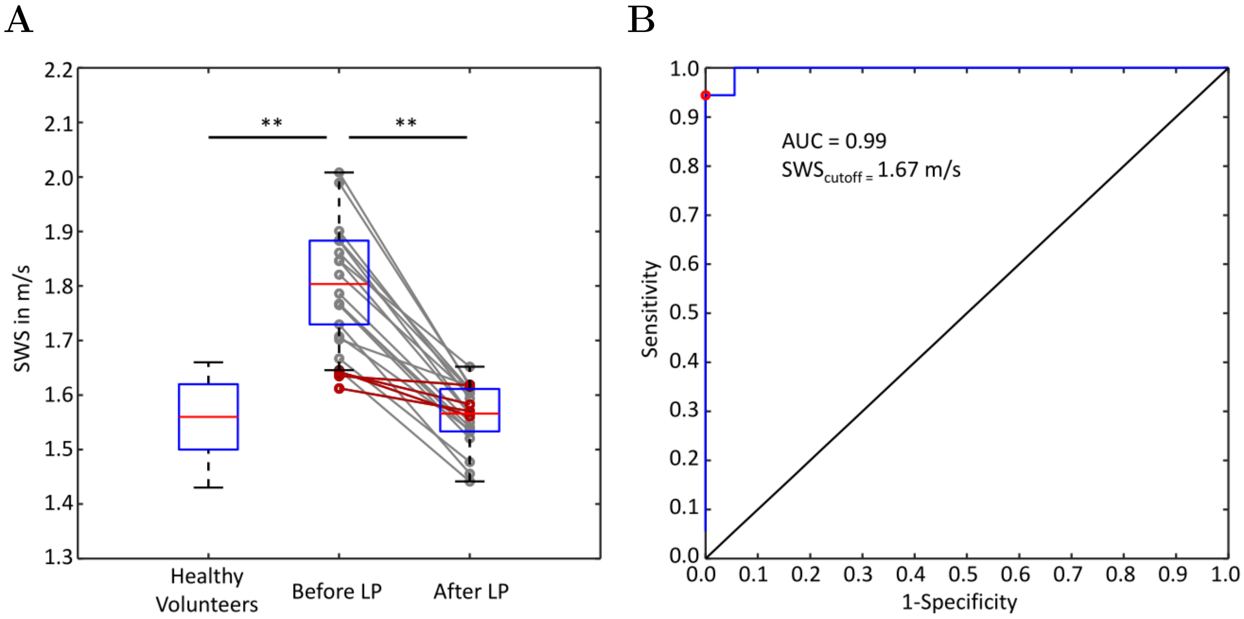

Figure 4.7: Statistical plots of group analysis and diagnostic performance. Figures adapted from Kreft et al. [79] with friendly permission of Wolters Kluwer Health Publishers.

Correlation analysis, shown in Figure 4.8, revealed a linear correlation of SWS with (A) V_{CSF} ($r = 0.72$, $p < 0.001$) and (B) P_{CSF} ($r = 0.69$, $p < 0.001$). A correlation was also found between V_{CSF} and P_{CSF} ($r = 0.54$, $p = 0.008$). While no correlations were found between P_{CSF}, SWS before LP, and SWS after LP with patient BMI or age, SWS correlated with age in healthy volunteers ($r = -0.77$, $p < 0.001$).

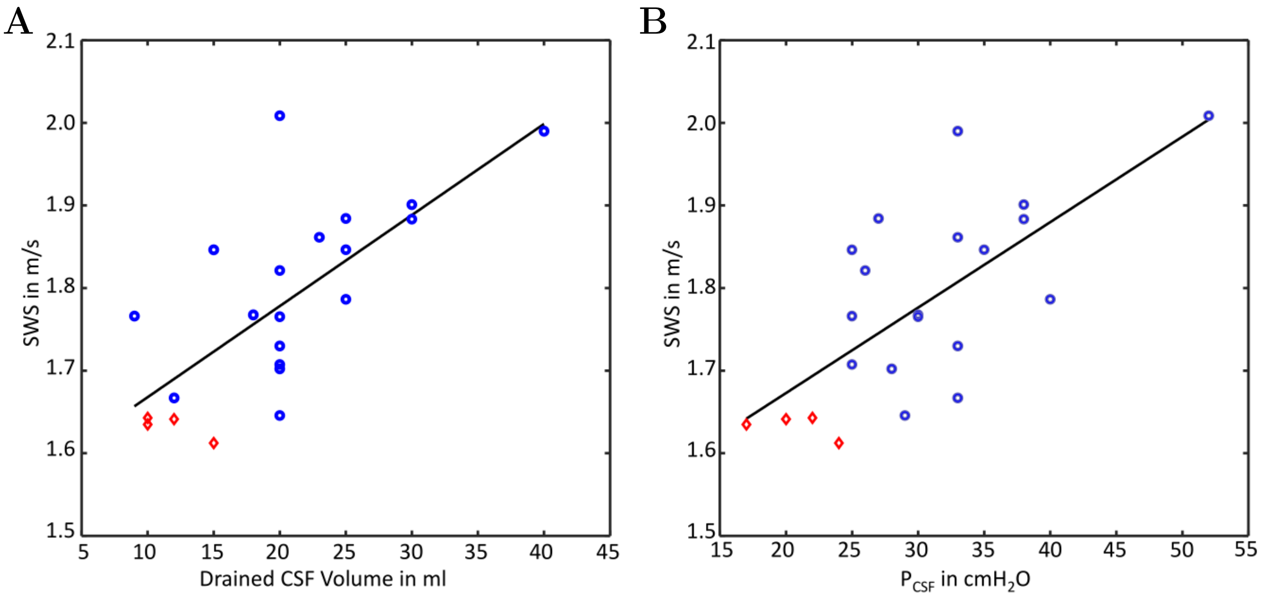

Figure 4.8: Scatter plots of statistical correlation analysis. Figures adapted from Kreft et al. [79] with friendly permission of Wolters Kluwer Health Publishers.

5. Discussion

Accurate determination of ICP is of central importance in today's clinical routine. However, previous noninvasive approaches such as computed tomography, MRI or ocular ultrasound examinations provide only crude and indirect indicators of elevated ICP, which in most cases is already coupled with pathological changes in the brain [7, 12, 13, 14, 15, 16, 17]. Cerebral THE is the first noninvasive, bedside, and easy-to-use ultrasound elastography modality suitable to reliably determine changes in CS [41, 20, 27]. Using cerebral THE, I observed that (i) CS measured in healthy volunteers is sensitive to altered cerebral perfusion during hypercapnia and hypotonic dehydration and rehydration, (ii) patients with confirmed IIH have abnormally high CS compared to healthy controls, and (iii) that reduction of CSF volume by LP immediately lowers CS in those patients to normal values comparable with healthy volunteers.

5.1 Cerebral THE in healthy volunteers

Hypercapnia

Within this project, the carbogen breathing experiment provided the first information on the time response of CS to a hypercapnic stimulus. Overall, a $5.9 \pm 4.0\,\%$ increase in CS was measured during 7 minutes of hypercapnia, which returned to baseline values approximately 3 minutes after carbogen breathing ceased. Because hypercapnia is associated with cerebral vasodilation and increased cerebral blood flow (CBF), it has been used in the past to study cerebrovascular reactivity and cerebral autoregulation [82, 83]. Based on relationship between hypercapnia and increased cerebral blood volume, my data suggest that changes in CS are tightly coupled with altered cerebral blood flow.

Hypercapnia-induced CS changes have been previously studied with MRE, where a CS increase of $3.3 \pm 1.9\,\%$ was observed, which overlaps with my results [84]. Furthermore, the dynamic time course of CS as I measured it in this experiment has never been assessed before. My data showed a delayed response of CS to hypercapnia by approximately 20 seconds, suggesting that cerebrovascular reactivity triggers vasodilation after this time and increases brain perfusion. Previous studies reported a CBF increase approximately 30 seconds after the pCO_2 increase [85], which is consistent with the observations in the present study. In addition, I found a delayed decrease in CS relative to $etCO_2$, which could be attributed to either a delayed vasoconstrictive response of cerebral vessels or a delayed washout of CO_2 from the lungs after 7 minutes of carbogen breathing.

According to previous studies, increased CBF during hypercapnia is in turn coupled with increased ICP, as postulated by the Monro-Kellie hypothesis discussed in Section 2.5 [47, 51, 82]. Therefore, the CS changes I measured during hypercapnia could reflect, at least in part, changes in ICP. Speculating here on the relationship between CS and ICP, the results of this study can be compared with the combination of the results of two previous studies in pigs. In one study, the response of ICP to elevated pCO_2 was examined, and a linear increase in ICP of approximately 0.7 % per 1 mmHg pCO_2 was observed [86]. A recent study in turn examined the response of CS to increased ICP by pumping saline into the ventricles in a controlled manner during MRE measurements. Here, a linear increase in CS of 0.6 % per 1 mmHg ICP was observed [87]. Based on these studies, an increase in CS of 0.75 % per 1 mmHg ICP could be predicted. Converting the increase in $etCO_2$ measured in my present study (in the range of 10 mmHg) to an ICP increase suggests a CS increase of 0.59 % per 1 mmHg. Although this value is in the same range as the predicted value, interspecies differences should be considered in this case.

De- and Rehydration

While the effect of hypercapnia on CS has been previously studied using MRE [84], this study provides the first insight into the effect of de- and rehydration on *in vivo* CS. I observed a significant decrease in CS of $4.4 \pm 1.7\,\%$ after a 12-hour fasting period, which returned to baseline values within 30 minutes after oral rehydration and was correlated with urine osmolality.

In healthy volunteers, hypotonic dehydration leads to a decrease, and oral rehydration consequently to an increase in urine osmolality, whereas it is less affected in patients with renal dysfunction or chronic kidney disease [88, 89]. Since only healthy volunteers were examined in this study, abnormal urine osmolality could be used as an exclusion criterion for group statistics. Consequently, two volunteers were excluded here because they did not comply with the fasting protocol. However, the CS changes measured in these volunteers were consistent with the correlation of urine osmolality and CS, providing clear evidence for the sensitivity of cerebral THE to the hydration status. In contrast to urine osmolality, none of the other recorded biological parameters such as blood pressure, heart rate, or hematocrit were correlated with CS. Previous studies did observe a slight decrease in CBF and blood pressure [62, 90, 91]. However, these studies (i) measured vessel diameters, which is a critical parameter in the assessment of CBF by Doppler ultrasound, and (ii) examined the effects of dehydration during physiological exercise, whereas I focused on dehydration at rest, which is generally associated with stable physiological conditions.

That CBF as well as brain tissue volume decrease during dehydration is well known and has been studied in the past using Doppler ultrasound as well as MRI [10, 63, 64, 92]. CS, in turn, is significantly affected by CBF, as observed by both MRE and my previous studies using cerebral THE [41, 72, 73, 84]. These observations further support my hypothesis that the CS variations I measured by cerebral THE during dehydration and rehydration may be due to changes in cerebral blood flow and -volume, and consequently influenced by changes in ICP.

Comparison with previous work

Whereas the baseline values in all studies I have performed so far (hypercapnia: $1.57 \pm 0.04\,\mathrm{m/s}$; de- and rehydration: $1.64 \pm 0.02\,\mathrm{m/s}$) were consistent with the baseline values obtained before this project ($1.56 \pm 0.08\,\mathrm{m/s}$) [41], the variations in CS I measured during hypercapnia ($5.9 \pm 4.0\,\%$) as well as de- and rehydration ($4.4 \pm 1.7\,\%$) are still relatively small compared to the effect I previously measured during the Valsalva maneuver ($10.8 \pm 2.5\,\%$) [41]. This could either be due to the fact that stiffness is only indirectly linked to perfusion via poroelastic interactions between fluid and solid compartments of brain tissue [25, 26, 74, 75, 93, 94] or due to the fact that cerebral autoregulation, with its task of keeping brain perfusion constant, changes biomechanical properties only over a small range [95, 96]. This would imply that medium- to long-term fluctuations in CBF could be fully compensated by a minor adjustment of the ICP, whereas rapid fluctuations such as the Valsalva maneuver, in which thoracic pressure is additionally transferred to the ICP, are too sudden to be fully compensated by cerebral autoregulation alone [97]. However, the hypothesis that fluctuations in cerebral perfusion, and in turn fluctuations in ICP [51], were reflected in CS variations was supported in every experiment I performed. This was the basis for applying cerebral THE clinically for the first time in patients with altered ICP who qualified for invasive ICP quantification.

5.2 Clinical patient study

My pilot clinical patient study showed a high sensitivity of cerebral THE in patients with confirmed IIH compared with healthy volunteers. In addition, I observed in patients that a reduction in CSF volume by LP resulted in a reduction in CS approximately 30 minutes after treatment. CS of patients after LP was subsequently indistinguishable from CS in healthy volunteers.

The choice of IIH as a model disease to study the sensitivity of CS to ICP fluctuations was motivated by the fact that the most prominent clinical sign in this disease is an elevated ICP without space-occupying comorbidities such as tumors, cerebral edema, or hemorrhage. In the past, it has been suggested that increased BMI may have an impact on the development of IIH. However, this association remains unclear, which is why obesity has not been included in diagnostic guidelines to date [18]. This was also reflected by my data, as I did not find an association between BMI and any other biological parameter obtained during this study. In contrast, I observed an association between measured CS and elevated ICP in diseased patients.

While CS values in healthy volunteers were in the same range as baseline values in all other experiments ($1.55 \pm 0.08\,\mathrm{m/s}$), patients exceeding the clinical threshold of $> 25\,\mathrm{cmH_2O}$ had significantly higher CS values ($1.81 \pm 0.10\,\mathrm{m/s}$). This was also reflected in the excellent diagnostic accuracy with which these two groups could be distinguished ($p < 0.001, AUC = 0.99$). In patients with the typical symptoms of IIH, such as chronic headache, visual field loss, and the presence of papilledema, LP with point measurement of CSF opening pressure is generally performed with suspicion of elevated ICP [18]. In the absence of prior information about ICP, patients who do not exceed the pathologic threshold of $> 25\,\mathrm{cmH_2O}$ must have a differential diagnosis, as IIH is ruled out as an underlying condition. Because all patients who did not meet this threshold within this study could be identified using noninvasive cerebral THE, my observations suggest that cerebral THE would be a promising tool to support the diagnosis of IIH and avoid unnecessary LP in the future.

In addition, I observed a decrease in of CS in patients to levels comparable with healthy volunteers after treatment. However, despite this CS decrease, patients with IIH are generally not in their normal state after LP, as the cranial system may adapt to long-term ICP changes such as those caused by IIH [98, 99, 100]. Because LP is considered more of a symptomatic treatment that results in an immediate decrease in CSF hydrostatic pressure and thus a decrease in ICP [67], the correlation I observed of invasively measured $\mathrm{P_{CSF}}$, SWS before LP, and $\mathrm{V_{CSF}}$, along with the decrease in CS after CSF drainage, is a strong argument that CS is affected by these short-term pressure changes. The change in CS due to LP in IIH patients has also been recently studied using MRE [101]. While an increased CS was also found in patients prior to LP, no LP-related decrease in CS was observed. One reason for this could be the increased stability of multifrequency cerebral THE compared to single frequency MRE (60 Hz vibration). To compare my results with those of this study, I analyzed the 56-Hz subset of my data. I found that the LP-related CS decrease detected with multifrequency evaluation changed from $16 \pm 5\,\%$ ($p < 0.001$) to $13 \pm 14\,\%$ ($p < 0.001$) with an increase in standard deviation, indicating the high robustness of multifrequency composite elastograms. In another MRE study, an initial increase and subsequent decrease in CS after LP was observed in patients with normal pressure hydrocephalus who responded to shunting [102]. However, that study measured intrinsically excited shear waves, which limits the comparability with my results.

Previously, I established a relationship between ICP and CS by comparing the results of MRE studies in pigs with my CS increase during hypercapnia and predicted a linear CS increase of 0.75 % per 1 mmHg ICP [86, 87]. The results of this study show that CS was increased by 0.9 % per 1 mmHg $\mathrm{P_{CSF}}$ prior to LP, which is within the range of this prediction and suggests a linear relationship between CS and ICP. However, this hypothesis needs to be carefully tested. For example, I found no difference between the correlation of CS measured as SWS with $\mathrm{P_{CSF}}$ and squared SWS ($\sim$ shear modulus, μ) with $\mathrm{P_{CSF}}$, so I cannot assume a strict linear relationship of CS measured with cerebral THE and invasively measured ICP.

In general, the factors that determine CS in vivo are very complex and are the subject of ongoing research. Most data on in vivo CS in humans or small animal models have been obtained using MRE measurements [103, 104, 105, 106]. In recent years, there has been increasing evidence of the sensitivity of CS to ICP-related diseases, such as normal pressure hydrocephalus [4, 102, 107]. Previous MRE studies have also observed associations between CS, ICP, and cerebral perfusion pressure [73] under the influence of hypercapnia [84], body temperature [108], hypoxia [109], and arterial pulsation [23]. Currently, the coupling of CS and pressure is being studied with a focus on biphasic material properties, as the brain is a complex biomechanical environment composed of fluid and solid parts that can interact with each other on multiple time and length scales [25, 26, 74, 75, 93, 110]. Although the underlying mechanisms are far from being fully deciphered, cerebral THE which I developed and validated in this project contributes significantly to understanding the relationship between CS, CBF and ICP and opens pathways of investigating rapid changes in CS in real-time [25, 26].

5.3 Limitations

Although the results of this project are encouraging, both cerebral THE and the studies I have conducted still have a few limitations. Cerebral THE, in its current stage of development, has limited spatial resolution and limited access to the brain. These are limitations that this method shares with transcranial ultrasound imaging. However, transcranial Doppler examinations are routinely used in the clinic to measure cerebral blood flow velocity. Further optimizations of transcranial imaging acquisition in terms of aberration corrections, as well as the use of ultrasound contrast agents to improve the echogenicity of highly vascularized areas such as the deep gray matter [73], could help improve the image quality of cerebral THE. In addition, the use of other acoustic windows could provide access to additional brain regions.

Experiments performed in healthy volunteers have so far lacked mechanistic validation of the underlying effects as well as evidence of ICP modulations. This is due to two reasons: (i) Doppler imaging could not be performed together with elastography measurements so far because imaging parameters were optimized for the post-processing algorithm and the high frame rates that I used were unsuitable for simultaneous measurement of Doppler and elastography data, and (ii) ICP measurement is invasive, and the risk outweighs the benefit in healthy volunteers. The first limitation could be overcome by designing a data acquisition system that can acquire both data sets simultaneously by rapidly switching between Doppler and elastography acquisition. For this purpose, plane-wave ultrasound could possibly be used together with the ultrafast Doppler technique [111]. The second limitation can be overcome by performing further clinical studies in patients who qualify for invasive ICP monitoring for a variety of reasons to further disentangle the relationship between CS and ICP.

Another limitation is that there is generally little knowledge about the relationship between CS and chronic tissue changes caused by abnormal ICP in patients. Because the brain can adapt to long-term pressure changes, baseline CS could also change because of progressive brain tissue degradation. Therefore, although some of the studies previously discussed show a linear relationship between CS and ICP [87, 102] and I can confirm this with the observations from this project, CS should not be translated into ICP without further modeling.

6. Conclusion

In summary, the cerebral THE I developed in this project could be used to quantify CS changes in healthy volunteers that could be associated with changes in cerebral perfusion. The measured data showed a 5.9 % increase in CS due to hypercapnia, a 4.4 % decrease in CS after 12 hours of dehydration, and a subsequent recovery of CS to baseline values 30 minutes after oral rehydration. All these findings were consistent with previously published data on CS changes due to ICP increases during the Valsalva maneuver and provided the basis for the first pilot clinical trial in patients with IIH. I found that diseased patients had significantly higher CS values than healthy volunteers, which returned to normal values after LP. Invasive P_{CSF} measurements during LP correlated linearly with CS measured noninvasively by cerebral THE, which is a strong argument that cerebral THE may allow the use of CS as a noninvasive surrogate for ICP changes in the future. Future clinical studies are needed to further investigate the relationship between CS and ICP in healthy volunteers and in ICP-related diseases. Overall, measurement of CS in real-time during physiological maneuvers such as Valsalva and hypercapnia may also help to assess the individual ability to regulate CBF changes and assist in neurological diagnosis. Cerebral THE may also provide initial noninvasive insight into patients with abnormal ICP and therefore promises to be of great benefit to neurologists, emergency departments, and patients.

References

1. Cook AM, Morgan Jones G, Hawryluk GWJ, Mailloux P, McLaughlin D, Papangelou A, Samuel S, Tokumaru S, Venkatasubramanian C, Zacko C, Zimmermann LL, Hirsch K, and Shutter L. Guidelines for the Acute Treatment of Cerebral Edema in Neurocritical Care Patients. Neurocrit Care 2020; 32:647–66. DOI: `10.1007/s12028-020-00959-7`. Available from: `https://www.ncbi.nlm.nih.gov/pubmed/32227294`
2. Okidi R, Ogwang DM, Okello TR, Ezati D, Kyegombe W, Nyeko D, and Scolding NJ. Factors affecting mortality after traumatic brain injury in a resource-poor setting. BJS Open 2020; 4:320–5. DOI: `10.1002/bjs5.50243`. Available from: `https://www.ncbi.nlm.nih.gov/pubmed/32207576`
3. Ren J, Wu X, Huang J, Cao X, Yuan Q, Zhang D, Du Z, Zhong P, and Hu J. Intracranial Pressure Monitoring-Aided Management Associated with Favorable Outcomes in Patients with Hypertension-Related Spontaneous Intracerebral Hemorrhage. Transl Stroke Res 2020. DOI: `10.1007/s12975-020-00798-w`. Available from: `https://www.ncbi.nlm.nih.gov/pubmed/32144586`
4. Murphy MC, Cogswell PM, Trzasko JD, Manduca A, Senjem ML, Meyer FB, Ehman RL, and Huston J. 3. Identification of Normal Pressure Hydrocephalus by Disease-Specific Patterns of Brain Stiffness and Damping Ratio. Invest Radiol 2020; 55:200–8. DOI: `10.1097/RLI.0000000000000630`. Available from: `https://www.ncbi.nlm.nih.gov/pubmed/32058331`
5. Gurney SP, Ramalingam S, Thomas A, Sinclair AJ, and Mollan SP. Exploring The Current Management Idiopathic Intracranial Hypertension, And Understanding The Role Of Dural Venous Sinus Stenting. Eye Brain 2020; 12:1–13. DOI: `10.2147/EB.S193027`. Available from: `https://www.ncbi.nlm.nih.gov/pubmed/32021528`
6. Leinonen V, Vanninen R, and Rauramaa T. Raised intracranial pressure and brain edema. Handb Clin Neurol 2017; 145:25–37. DOI: `10.1016/B978-0-12-802395-2.00004-3`. Available from: `https://www.ncbi.nlm.nih.gov/pubmed/28987174%20https://www.sciencedirect.com/science/article/pii/B9780128023952000043?via%3Dihub`
7. Rakhit S, Nordness MF, Lombardo SR, Cook M, Smith L, and Patel MB. Management and Challenges of Severe Traumatic Brain Injury. Semin Respir Crit Care Med 2021; 42:127–44. DOI: `10.1055/s-0040-1716493`. Available from: `https://www.ncbi.nlm.nih.gov/pubmed/32916746%20https://www.thieme-connect.com/products/ejournals/abstract/10.1055/s-0040-1716493`
8. Nag DS, Sahu S, Swain A, and Kant S. Intracranial pressure monitoring: Gold standard and recent innovations. World J Clin Cases 2019; 7:1535–53. DOI: `10.12998/wjcc.v7.i13.1535`. Available from: `https://www.ncbi.nlm.nih.gov/pubmed/31367614%`

20https://www.ncbi.nlm.nih.gov/pmc/articles/PMC6658373/pdf/WJCC-7-1535.pdf

9. Bo SH and Lundqvist C. Cerebrospinal fluid opening pressure in clinical practice - a prospective study. J Neurol 2020; 267:3696–701. DOI: 10.1007/s00415-020-10075-3. Available from: https://www.ncbi.nlm.nih.gov/pubmed/32681283%20https://www.ncbi.nlm.nih.gov/pmc/articles/PMC7674322/pdf/415_2020_Article_10075.pdf

10. Sonig A, Jumah F, Raju B, Patel NV, Gupta G, and Nanda A. The Historical Evolution of Intracranial Pressure Monitoring. World Neurosurg 2020; 138:491–7. DOI: 10.1016/j.wneu.2020.03.028. Available from: https://www.ncbi.nlm.nih.gov/pubmed/32179192

11. Tavakoli S, Peitz G, Ares W, Hafeez S, and Grandhi R. Complications of invasive intracranial pressure monitoring devices in neurocritical care. Neurosurg Focus 2017; 43:E6. DOI: 10.3171/2017.8.FOCUS17450. Available from: https://www.ncbi.nlm.nih.gov/pubmed/29088962

12. Zhang X, Medow JE, Iskandar BJ, Wang F, Shokoueinejad M, Koueik J, and Webster JG. Invasive and noninvasive means of measuring intracranial pressure: a review. Physiol Meas 2017; 38:R143–R182. DOI: 10.1088/1361-6579/aa7256. Available from: https://www.ncbi.nlm.nih.gov/pubmed/28489610

13. Eisenberg HM, Gary H. E. J, Aldrich EF, Saydjari C, Turner B, Foulkes MA, Jane JA, Marmarou A, Marshall LF, and Young HF. Initial CT findings in 753 patients with severe head injury. A report from the NIH Traumatic Coma Data Bank. J Neurosurg 1990; 73:688–98. DOI: 10.3171/jns.1990.73.5.0688. Available from: https://www.ncbi.nlm.nih.gov/pubmed/2213158%20https://thejns.org/view/journals/j-neurosurg/73/5/article-p688.xml

14. Wei H, Tang X, Zhang M, Li Q, Xing X, Sean Zhou X, Xue Z, Zhu W, Chen Z, and Shi F. The delineation of largely deformed brain midline using regression-based line detection network. Med Phys 2020; 47:5531–42. DOI: 10.1002/mp.14302. Available from: https://www.ncbi.nlm.nih.gov/pubmed/32471017

15. Alperin NJ, Lee SH, Loth F, Raksin PB, and Lichtor T. MR-Intracranial pressure (ICP): a method to measure intracranial elastance and pressure noninvasively by means of MR imaging: baboon and human study. Radiology 2000; 217:877–85. DOI: 10.1148/radiology.217.3.r00dc42877. Available from: https://www.ncbi.nlm.nih.gov/pubmed/11110957

16. Alperin N. MR-intracranial compliance and pressure: a method for noninvasive measurement of important neurophysiologic parameters. Methods Enzymol 2004; 386:323–49. DOI: 10.1016/S0076-6879(04)86016-6. Available from: https://www.ncbi.nlm.nih.gov/pubmed/15120260

17. Wang LJ, Chen HX, Chen Y, Yu ZY, and Xing YQ. Optic nerve sheath diameter ultrasonography for elevated intracranial pressure detection. Ann Clin Transl Neurol 2020; 7:865–8. DOI: `10.1002/acn3.51054`. Available from: `https://www.ncbi.nlm.nih.gov/pubmed/32383326`

18. Mollan SP, Davies B, Silver NC, Shaw S, Mallucci CL, Wakerley BR, Krishnan A, Chavda SV, Ramalingam S, Edwards J, Hemmings K, Williamson M, Burdon MA, Hassan-Smith G, Digre K, Liu GT, Jensen RH, and Sinclair AJ. Idiopathic intracranial hypertension: consensus guidelines on management. J Neurol Neurosurg Psychiatry 2018; 89:1088–100. DOI: `10.1136/jnnp-2017-317440`. Available from: `https://www.ncbi.nlm.nih.gov/pubmed/29903905`

19. Pedersen SH, Lilja-Cyron A, Astrand R, and Juhler M. Monitoring and Measurement of Intracranial Pressure in Pediatric Head Trauma. Front Neurol 2019; 10:1376. DOI: `10.3389/fneur.2019.01376`. Available from: `https://www.ncbi.nlm.nih.gov/pubmed/32010042`

20. Hirsch S, Braun J, and Sack I. Magnetic Resonance Elastography: Physical Background And Medical Applications. Wiley-VCH, 2017

21. Sack I and Schaeffter T. Quantification of biophysical parameters in medical imaging. Springer Nature, 2018

22. Schrank F, Warmuth C, Gorner S, Meyer T, Tzschatzsch H, Guo J, Uca YO, Elgeti T, Braun J, and Sack I. Real-time MR elastography for viscoelasticity quantification in skeletal muscle during dynamic exercises. Magn Reson Med 2020; 84:103–14. DOI: `10.1002/mrm.28095`. Available from: `https://www.ncbi.nlm.nih.gov/pubmed/31774210`

23. Schrank F, Warmuth C, Tzschatzsch H, Kreft B, Hirsch S, Braun J, Elgeti T, and Sack I. Cardiac-gated steady-state multifrequency magnetic resonance elastography of the brain: Effect of cerebral arterial pulsation on brain viscoelasticity. J Cereb Blood Flow Metab 2020; 40:991–1001. DOI: `10.1177/0271678X19850936`. Available from: `https://www.ncbi.nlm.nih.gov/pubmed/31142226%20https://journals.sagepub.com/doi/10.1177/0271678X19850936?url_ver=Z39.88-2003&rfr_id=ori:rid:crossref.org&rfr_dat=cr_pub%3dpubmed`

24. Herthum H, Shahryari M, Tzschatzsch H, Schrank F, Warmuth C, Gorner S, Hetzer S, Neubauer H, Pfeuffer J, Braun J, and Sack I. Real-Time Multifrequency MR Elastography of the Human Brain Reveals Rapid Changes in Viscoelasticity in Response to the Valsalva Maneuver. Front Bioeng Biotechnol 2021; 9:666456. DOI: `10.3389/fbioe.2021.666456`. Available from: `https://www.ncbi.nlm.nih.gov/pubmed/34026743`

25. Parker KJ. Experimental evaluations of the microchannel flow model. Phys Med Biol 2015; 60:4227–42. DOI: `10.1088/0031-9155/60/11/4227`. Available from: `https://www.ncbi.nlm.nih.gov/pubmed/25973729`

26. Parker KJ. Are rapid changes in brain elasticity possible? Phys Med Biol 2017; 62:7425–39. DOI: 10.1088/1361-6560/aa8380. Available from: https://www.ncbi.nlm.nih.gov/pubmed/28766505

27. Tzschätzsch H, Kreft B, Braun J, and Sack I. Transtemporal Investigation of Brain Parenchyma Elasticity Using 2-D Shear Wave Elastography: Trustworthy? Ultrasound Med Biol 2019; 45:1344–5. DOI: 10.1016/j.ultrasmedbio.2019.01.005. Available from: https://www.ncbi.nlm.nih.gov/pubmed/30770137

28. Cosgrove D, Barr R, Bojunga J, Cantisani V, Chammas MC, Dighe M, Vinayak S, Xu JM, and Dietrich CF. WFUMB Guidelines and Recommendations on the Clinical Use of Ultrasound Elastography: Part 4. Thyroid. Ultrasound Med Biol 2017; 43:4–26. DOI: 10.1016/j.ultrasmedbio.2016.06.022. Available from: https://www.ncbi.nlm.nih.gov/pubmed/27570210

29. Ferraioli G, Filice C, Castera L, Choi BI, Sporea I, Wilson SR, Cosgrove D, Dietrich CF, Amy D, Bamber JC, Barr R, Chou YH, Ding H, Farrokh A, Friedrich-Rust M, Hall TJ, Nakashima K, Nightingale KR, Palmeri ML, Schafer F, Shiina T, Suzuki S, and Kudo M. WFUMB guidelines and recommendations for clinical use of ultrasound elastography: Part 3: liver. Ultrasound Med Biol 2015; 41:1161–79. DOI: 10.1016/j.ultrasmedbio.2015.03.007. Available from: https://www.ncbi.nlm.nih.gov/pubmed/25800942

30. Shiina T, Nightingale KR, Palmeri ML, Hall TJ, Bamber JC, Barr RG, Castera L, Choi BI, Chou YH, Cosgrove D, Dietrich CF, Ding H, Amy D, Farrokh A, Ferraioli G, Filice C, Friedrich-Rust M, Nakashima K, Schafer F, Sporea I, Suzuki S, Wilson S, and Kudo M. WFUMB guidelines and recommendations for clinical use of ultrasound elastography: Part 1: basic principles and terminology. Ultrasound Med Biol 2015; 41:1126–47. DOI: 10.1016/j.ultrasmedbio.2015.03.009. Available from: https://www.ncbi.nlm.nih.gov/pubmed/25805059

31. Nightingale K. Acoustic Radiation Force Impulse (ARFI) Imaging: a Review. Curr Med Imaging Rev 2011; 7:328–39. DOI: 10.2174/157340511798038657. Available from: https://www.ncbi.nlm.nih.gov/pubmed/22545033

32. Tzschätzsch H, Nguyen Trong M, Scheuermann T, Ipek-Ugay S, Fischer T, Schultz M, Braun J, and Sack I. Two-Dimensional Time-Harmonic Elastography of the Human Liver and Spleen. Ultrasound Med Biol 2016; 42:2562–71. DOI: 10.1016/j.ultrasmedbio.2016.07.004. Available from: https://www.ncbi.nlm.nih.gov/pubmed/27567061%20https://www.umbjournal.org/article/S0301-5629(16)30163-6/fulltext

33. Marticorena Garcia SR, Grossmann M, Lang ST, Nguyen Trong M, Schultz M, Guo J, Hamm B, Braun J, Sack I, and Tzschatzsch H. Full-Field-of-View Time-Harmonic Elastography of the Native Kidney. Ultrasound Med Biol 2018; 44:949–54. DOI: 10.1016/j.ultrasmedbio.2018.01.007. Available from: https://www.ncbi.nlm.nih.gov/pubmed/29478787

34. Burkhardt C, Tzschatzsch H, Schmuck R, Bahra M, Jurgensen C, Pelzer U, Hamm B, Braun J, Sack I, and Marticorena Garcia SR. Ultrasound Time-Harmonic Elastography of the Pancreas: Reference Values and Clinical Feasibility. Invest Radiol 2020; 55:270–6. DOI: `10.1097/RLI.0000000000000638`. Available from: `https://www.ncbi.nlm.nih.gov/pubmed/31985600`

35. Hudert CA, Tzschatzsch H, Guo J, Rudolph B, Blaker H, Loddenkemper C, Luck W, Muller HP, Baumgart DC, Hamm B, Braun J, Holzhutter HG, Wiegand S, and Sack I. US Time-Harmonic Elastography: Detection of Liver Fibrosis in Adolescents with Extreme Obesity with Nonalcoholic Fatty Liver Disease. Radiology 2018; 288:99–106. DOI: `10.1148/radiol.2018172928`. Available from: `https://www.ncbi.nlm.nih.gov/pubmed/29762096`

36. Grossmann M, Tzschatzsch H, Lang ST, Guo J, Bruns A, Durr M, Hoyer BF, Grittner U, Lerchbaumer M, Nguyen Trong M, Schultz M, Hamm B, Braun J, Sack I, and Marticorena Garcia SR. US Time-Harmonic Elastography for the Early Detection of Glomerulonephritis. Radiology 2019; 292:676–84. DOI: `10.1148/radiol.2019182574`. Available from: `https://www.ncbi.nlm.nih.gov/pubmed/31287390`

37. Hudert CA, Tzschatzsch H, Rudolph B, Loddenkemper C, Holzhutter HG, Kalveram L, Wiegand S, Braun J, Sack I, and Guo J. How histopathologic changes in pediatric nonalcoholic fatty liver disease influence in vivo liver stiffness. Acta Biomater 2021; 123:178–86. DOI: `10.1016/j.actbio.2021.01.019`. Available from: `https://www.ncbi.nlm.nih.gov/pubmed/33472102`

38. Ipek-Ugay S, Tzschatzsch H, Braun J, Fischer T, and Sack I. Physiologic Reduction of Hepatic Venous Blood Flow by the Valsalva Maneuver Decreases Liver Stiffness. J Ultrasound Med 2017; 36:1305–11. DOI: `10.7863/ultra.16.07046`. Available from: `https://www.ncbi.nlm.nih.gov/pubmed/28319252`

39. Ipek-Ugay S, Tzschatzsch H, Hudert C, Marticorena Garcia SR, Fischer T, Braun J, Althoff C, and Sack I. Time Harmonic Elastography Reveals Sensitivity of Liver Stiffness to Water Ingestion. Ultrasound Med Biol 2016; 42:1289–94. DOI: `10.1016/j.ultrasmedbio.2015.12.026`. Available from: `https://www.ncbi.nlm.nih.gov/pubmed/26971462`

40. Tzschätzsch H, Sack I, Marticorena Garcia SR, Ipek-Ugay S, Braun J, Hamm B, and Althoff CE. Time-Harmonic Elastography of the Liver is Sensitive to Intrahepatic Pressure Gradient and Liver Decompression after Transjugular Intrahepatic Portosystemic Shunt (TIPS) Implantation. Ultrasound Med Biol 2017; 43:595–600. DOI: `10.1016/j.ultrasmedbio.2016.10.007`. Available from: `https://www.ncbi.nlm.nih.gov/pubmed/27979668`

41. Tzschätzsch H, Kreft B, Schrank F, Bergs J, Braun J, and Sack I. In vivo time-harmonic ultrasound elastography of the human brain detects acute cerebral stiffness changes induced by intracranial pressure variations. Sci Rep 2018; 8:17888. DOI:

10.1038/s41598-018-36191-9. Available from: https://www.ncbi.nlm.nih.gov/pubmed/30559367%20https://www.ncbi.nlm.nih.gov/pmc/articles/PMC6297160/pdf/41598_2018_Article_36191.pdf

42. Sack I, Beierbach B, Wuerfel J, Klatt D, Hamhaber U, Papazoglou S, Martus P, and Braun J. The impact of aging and gender on brain viscoelasticity. Neuroimage 2009; 46:652–7. DOI: 10.1016/j.neuroimage.2009.02.040. Available from: https://www.ncbi.nlm.nih.gov/pubmed/19281851

43. Sack I, Streitberger KJ, Krefting D, Paul F, and Braun J. The influence of physiological aging and atrophy on brain viscoelastic properties in humans. PLoS One 2011; 6:e23451. DOI: 10.1371/journal.pone.0023451. Available from: https://www.ncbi.nlm.nih.gov/pubmed/21931599

44. Looga R. The Valsalva manoeuvre–cardiovascular effects and performance technique: a critical review. Respir Physiol Neurobiol 2005; 147:39–49. DOI: 10.1016/j.resp.2005.01.003. Available from: https://www.ncbi.nlm.nih.gov/pubmed/15848122

45. Fierstra J, Sobczyk O, Battisti-Charbonney A, Mandell DM, Poublanc J, Crawley AP, Mikulis DJ, Duffin J, and Fisher JA. Measuring cerebrovascular reactivity: what stimulus to use? J Physiol 2013; 591:5809–21. DOI: 10.1113/jphysiol.2013.259150. Available from: https://www.ncbi.nlm.nih.gov/pubmed/24081155

46. Prabhakar H, Bithal PK, Suri A, Rath GP, and Dash HH. Intracranial pressure changes during Valsalva manoeuvre in patients undergoing a neuroendoscopic procedure. Minim Invasive Neurosurg 2007; 50:98–101. DOI: 10.1055/s-2007-982505. Available from: https://www.ncbi.nlm.nih.gov/pubmed/17674296

47. Wagshul ME, Eide PK, and Madsen JR. The pulsating brain: A review of experimental and clinical studies of intracranial pulsatility. Fluids Barriers CNS 2011; 8:5. DOI: 10.1186/2045-8118-8-5. Available from: https://www.ncbi.nlm.nih.gov/pubmed/21349153

48. Tzschätzsch H. Entwicklung, Anwendung und Validierung der zeitharmonischen in vivo Ultraschallelastografie an der menschlichen Leber und am menschlichen Herzen. Thesis. 2017. DOI: http://dx.doi.org/10.18452/17685

49. Carcione J. Wave Fields in Real Media: Wave Propagation in Anisotropic, Anelastic, Porous and Electromagnetic Media. Elsevier Science, 2007. Available from: https://books.google.de/books?id=Bla-lAEACAAJ

50. Sarvazyan AP, Urban MW, and Greenleaf JF. Acoustic waves in medical imaging and diagnostics. Ultrasound Med Biol 2013; 39:1133–46. DOI: 10.1016/j.ultrasmedbio.2013.02.006. Available from: https://www.ncbi.nlm.nih.gov/pubmed/23643056

51. Mokri B. The Monro-Kellie hypothesis: applications in CSF volume depletion. Neurology 2001; 56:1746–8. DOI: 10.1212/wnl.56.12.1746. Available from: https://www.ncbi.nlm.nih.gov/pubmed/11425944

52. Richardson A, Eversden I, and Sternbergh C. Intracranial pressure in tumours. Proc R Soc Med 1972; 65:886–8. Available from: `https://www.ncbi.nlm.nih.gov/pubmed/5085087`

53. Pedersen SH, Lilja-Cyron A, Andresen M, and Juhler M. The Relationship Between Intracranial Pressure and Age-Chasing Age-Related Reference Values. World Neurosurg 2018; 110:e119–e123. DOI: `10.1016/j.wneu.2017.10.086`. Available from: `https://www.ncbi.nlm.nih.gov/pubmed/29107158`

54. Marmarou A, Shulman K, and LaMorgese J. Compartmental analysis of compliance and outflow resistance of the cerebrospinal fluid system. J Neurosurg 1975; 43:523–34. DOI: `10.3171/jns.1975.43.5.0523`. Available from: `https://www.ncbi.nlm.nih.gov/pubmed/1181384%20https://thejns.org/view/journals/j-neurosurg/43/5/article-p523.xml`

55. Brimioulle S, Moraine JJ, Norrenberg D, and Kahn RJ. Effects of positioning and exercise on intracranial pressure in a neurosurgical intensive care unit. Phys Ther 1997; 77:1682–9. DOI: `10.1093/ptj/77.12.1682`. Available from: `https://www.ncbi.nlm.nih.gov/pubmed/9413447`

56. Lawley JS, Petersen LG, Howden EJ, Sarma S, Cornwell WK, Zhang R, Whitworth LA, Williams MA, and Levine BD. Effect of gravity and microgravity on intracranial pressure. J Physiol 2017; 595:2115–27. DOI: `10.1113/JP273557`. Available from: `https://www.ncbi.nlm.nih.gov/pubmed/28092926`

57. Rossi S, Picetti E, Zoerle T, Carbonara M, Zanier ER, and Stocchetti N. Fluid Management in Acute Brain Injury. Curr Neurol Neurosci Rep 2018; 18:74. DOI: `10.1007/s11910-018-0885-8`. Available from: `https://www.ncbi.nlm.nih.gov/pubmed/30206730`

58. Giller CA, Bowman G, Dyer H, Mootz L, and Krippner W. Cerebral arterial diameters during changes in blood pressure and carbon dioxide during craniotomy. Neurosurgery 1993; 32:737–41, discussion 741–2. Available from: `https://www.ncbi.nlm.nih.gov/pubmed/8492848`

59. Haubrich C, Steiner LA, Diehl RR, Kasprowicz M, Smielewski P, Pickard JD, and Czosnyka M. Doppler flow velocity and intra-cranial pressure: responses to short-term mild hypocapnia help to assess the pressure-volume relationship after head injury. Ultrasound Med Biol 2013; 39:1521–6. DOI: `10.1016/j.ultrasmedbio.2013.03.020`. Available from: `https://www.ncbi.nlm.nih.gov/pubmed/23830102`

60. Rich M, Scheinberg P, and Belle MS. Relationship between cerebrospinal fluid pressure changes and cerebral blood flow. Circ Res 1953; 1:389–95. DOI: `10.1161/01.res.1.5.389`. Available from: `https://www.ncbi.nlm.nih.gov/pubmed/13082679`

61. Armstrong LE. Hydration assessment techniques. Nutr Rev 2005; 63:S40–54. DOI: `10.1111/j.1753-4887.2005.tb00153.x`. Available from: `https://www.ncbi.nlm.nih.gov/pubmed/16028571`

62. Trangmar SJ, Chiesa ST, Stock CG, Kalsi KK, Secher NH, and Gonzalez-Alonso J. Dehydration affects cerebral blood flow but not its metabolic rate for oxygen during maximal exercise in trained humans. J Physiol 2014; 592:3143–60. DOI: `10.1113/jphysiol.2014.272104`. Available from: `https://www.ncbi.nlm.nih.gov/pubmed/24835170`

63. Duning T, Kloska S, Steinstrater O, Kugel H, Heindel W, and Knecht S. Dehydration confounds the assessment of brain atrophy. Neurology 2005; 64:548–50. DOI: `10.1212/01.WNL.0000150542.16969.CC`. Available from: `https://www.ncbi.nlm.nih.gov/pubmed/15699394%20https://n.neurology.org/content/64/3/548.long`

64. Streitburger DP, Moller HE, Tittgemeyer M, Hund-Georgiadis M, Schroeter ML, and Mueller K. Investigating structural brain changes of dehydration using voxel-based morphometry. PLoS One 2012; 7:e44195. DOI: `10.1371/journal.pone.0044195`. Available from: `https://www.ncbi.nlm.nih.gov/pubmed/22952926`

65. Schizodimos T, Soulountsi V, Iasonidou C, and Kapravelos N. An overview of management of intracranial hypertension in the intensive care unit. J Anesth 2020; 34:741–57. DOI: `10.1007/s00540-020-02795-7`. Available from: `https://www.ncbi.nlm.nih.gov/pubmed/32440802`

66. Schievink WI. Spontaneous spinal cerebrospinal fluid leaks and intracranial hypotension. JAMA 2006; 295:2286–96. DOI: `10.1001/jama.295.19.2286`. Available from: `https://www.ncbi.nlm.nih.gov/pubmed/16705110`

67. Carney N, Totten AM, O'Reilly C, Ullman JS, Hawryluk GW, Bell MJ, Bratton SL, Chesnut R, Harris OA, Kissoon N, Rubiano AM, Shutter L, Tasker RC, Vavilala MS, Wilberger J, Wright DW, and Ghajar J. Guidelines for the Management of Severe Traumatic Brain Injury, Fourth Edition. Neurosurgery 2017; 80:6–15. DOI: `10.1227/NEU.0000000000001432`. Available from: `https://www.ncbi.nlm.nih.gov/pubmed/27654000`

68. Sundholm A, Burkill S, Sveinsson O, Piehl F, Bahmanyar S, and Nilsson Remahl AIM. Population-based incidence and clinical characteristics of idiopathic intracranial hypertension. Acta Neurol Scand 2017; 136:427–33. DOI: `10.1111/ane.12742`. Available from: `https://www.ncbi.nlm.nih.gov/pubmed/28244170`

69. Wuerfel J, Paul F, Beierbach B, Hamhaber U, Klatt D, Papazoglou S, Zipp F, Martus P, Braun J, and Sack I. MR-elastography reveals degradation of tissue integrity in multiple sclerosis. Neuroimage 2010; 49:2520–5. DOI: `10.1016/j.neuroimage.2009.06.018`. Available from: `https://www.ncbi.nlm.nih.gov/pubmed/19539039`

70. Streitberger KJ, Sack I, Krefting D, Pfuller C, Braun J, Paul F, and Wuerfel J. Brain viscoelasticity alteration in chronic-progressive multiple sclerosis. PLoS One 2012; 7:e29888. DOI: `10.1371/journal.pone.0029888`. Available from: `https://www.ncbi.nlm.nih.gov/pubmed/22276134`

71. Wang S, Millward JM, Hanke-Vela L, Malla B, Pilch K, Gil-Infante A, Waiczies S, Mueller S, Boehm-Sturm P, Guo J, Sack I, and Infante-Duarte C. MR Elastography-Based Assessment of Matrix Remodeling at Lesion Sites Associated With Clinical Severity in a Model of Multiple Sclerosis. Front Neurol 2019; 10:1382. DOI: `10.3389/fneur.2019.01382`. Available from: `https://www.ncbi.nlm.nih.gov/pubmed/31998225`

72. Guo J, Hirsch S, Fehlner A, Papazoglou S, Scheel M, Braun J, and Sack I. Towards an elastographic atlas of brain anatomy. PLoS One 2013; 8:e71807. DOI: `10.1371/journal.pone.0071807`. Available from: `https://www.ncbi.nlm.nih.gov/pubmed/23977148`

73. Hetzer S, Birr P, Fehlner A, Hirsch S, Dittmann F, Barnhill E, Braun J, and Sack I. Perfusion alters stiffness of deep gray matter. J Cereb Blood Flow Metab 2018; 38:116–25. DOI: `10.1177/0271678X17691530`. Available from: `https://www.ncbi.nlm.nih.gov/pubmed/28151092%20https://www.ncbi.nlm.nih.gov/pmc/articles/PMC5757437/pdf/10.1177_0271678X17691530.pdf`

74. Lilaj L, Fischer T, Guo J, Braun J, Sack I, and Hirsch S. Separation of fluid and solid shear wave fields and quantification of coupling density by magnetic resonance poroelastography. Magn Reson Med 2020. DOI: `10.1002/mrm.28507`. Available from: `https://www.ncbi.nlm.nih.gov/pubmed/32902011`

75. Hirsch S. A Biphasic Poroelastic Model for Soft Tissues. *Quantification of Biophysical Parameters in Medical Imaging*. Ed. by Sack I and Schaeffter T. 1st ed. Heidelberg: Springer, 2018 :71

76. Marticorena Garcia SR, Grossmann M, Lang ST, Tzschatzsch H, Dittmann F, Hamm B, Braun J, Guo J, and Sack I. Tomoelastography of the native kidney: Regional variation and physiological effects on in vivo renal stiffness. Magn Reson Med 2018; 79:2126–34. DOI: `10.1002/mrm.26892`. Available from: `https://www.ncbi.nlm.nih.gov/pubmed/28856718`

77. Kreft B, Tzschatzsch H, Schrank F, Bergs J, Streitberger KJ, Waldchen S, Hetzer S, Braun J, and Sack I. Time-Resolved Response of Cerebral Stiffness to Hypercapnia in Humans. Ultrasound Med Biol 2020; 46:936–43. DOI: `10.1016/j.ultrasmedbio.2019.12.019`. Available from: `https://www.ncbi.nlm.nih.gov/pubmed/32001088%20https://www.umbjournal.org/article/S0301-5629(19)31639-4/fulltext`

78. Kreft B, Bergs J, Shahryari M, Danyel LA, Hetzer S, Braun J, Sack I, and Tzschatzsch H. Cerebral Ultrasound Time-Harmonic Elastography Reveals Softening of the Human Brain Due to Dehydration. Front Physiol 2020; 11:616984. DOI: `10.3389/fphys.2020.616984`. Available from: `https://www.ncbi.nlm.nih.gov/pubmed/33505319`

79. Kreft B, Tzschatzsch H, Shahryari M, Haffner P, Braun J, Sack I, and Streitberger KJ. Noninvasive Detection of Intracranial Hypertension by Novel Ultrasound Time-Harmonic Elastography. Invest Radiol 2021. DOI: `10.1097/RLI.0000000000000817`. Available from: `https://www.ncbi.nlm.nih.gov/pubmed/34380993`

80. Tzschätzsch H, Guo J, Dittmann F, Hirsch S, Barnhill E, Johrens K, Braun J, and Sack I. Tomoelastography by multifrequency wave number recovery from time-harmonic propagating shear waves. Med Image Anal 2016; 30:1–10. DOI: `10.1016/j.media.2016.01.001`. Available from: `https://www.ncbi.nlm.nih.gov/pubmed/26845371`

81. Manduca A, Lake DS, Kruse SA, and Ehman RL. Spatio-temporal directional filtering for improved inversion of MR elastography images. Med Image Anal 2003; 7:465–73. DOI: `10.1016/s1361-8415(03)00038-0`. Available from: `https://www.ncbi.nlm.nih.gov/pubmed/14561551`

82. Brian J. E. J. Carbon dioxide and the cerebral circulation. Anesthesiology 1998; 88:1365–86. DOI: `10.1097/00000542-199805000-00029`. Available from: `https://www.ncbi.nlm.nih.gov/pubmed/9605698`

83. Ainslie PN and Duffin J. Integration of cerebrovascular CO2 reactivity and chemoreflex control of breathing: mechanisms of regulation, measurement, and interpretation. Am J Physiol Regul Integr Comp Physiol 2009; 296:R1473–95. DOI: `10.1152/ajpregu.91008.2008`. Available from: `https://www.ncbi.nlm.nih.gov/pubmed/19211719`

84. Hetzer S, Dittmann F, Bormann K, Hirsch S, Lipp A, Wang DJ, Braun J, and Sack I. Hypercapnia increases brain viscoelasticity. J Cereb Blood Flow Metab 2019; 39:2445–55. DOI: `10.1177/0271678X18799241`. Available from: `https://www.ncbi.nlm.nih.gov/pubmed/30182788%20https://journals.sagepub.com/doi/10.1177/0271678X18799241?url_ver=Z39.88-2003&rfr_id=ori%3Arid%3Acrossref.org&rfr_dat=cr_pub%3Dpubmed&`

85. Ogoh S, Ainslie PN, and Miyamoto T. Onset responses of ventilation and cerebral blood flow to hypercapnia in humans: rest and exercise. J Appl Physiol (1985) 2009; 106:880–6. DOI: `10.1152/japplphysiol.91292.2008`. Available from: `https://www.ncbi.nlm.nih.gov/pubmed/19131474`

86. Hulst RA van, Hasan D, and Lachmann B. Intracranial pressure, brain PCO2, PO2, and pH during hypo- and hyperventilation at constant mean airway pressure in pigs. Intensive Care Med 2002; 28:68–73. DOI: `10.1007/s00134-001-1157-6`. Available from: `https://www.ncbi.nlm.nih.gov/pubmed/11819003`

87. Arani A, Min HK, Fattahi N, Wetjen NM, Trzasko JD, Manduca A, Jack C. R. J, Lee KH, Ehman RL, and Huston J. 3. Acute pressure changes in the brain are correlated with MR elastography stiffness measurements: initial feasibility in an in vivo large animal model. Magn Reson Med 2018; 79:1043–51. DOI: `10.1002/mrm.26738`. Available from: `https://www.ncbi.nlm.nih.gov/pubmed/28488326%20https://www.ncbi.nlm.nih.gov/pmc/articles/PMC5811891/pdf/MRM-79-1043.pdf`

88. Roscoe MH. Urine in Acute and Chronic Renal Failure. Br Med J 1964; 1:1084–7. DOI: `10.1136/bmj.1.5390.1084`. Available from: `https://www.ncbi.nlm.nih.gov/pubmed/14113823`

89. Tabibzadeh N, Wagner S, Metzger M, Flamant M, Houillier P, Boffa JJ, Vrtovsnik F, Thervet E, Stengel B, Haymann JP, and NephroTest Study G. Fasting Urinary Osmolality, CKD Progression, and Mortality: A Prospective Observational Study. Am J Kidney Dis 2019; 73:596–604. DOI: `10.1053/j.ajkd.2018.12.024`. Available from: `https://www.ncbi.nlm.nih.gov/pubmed/30777634`

90. Tsai YH, Yang JL, Lee IN, Yang JT, Lin LC, Huang YC, Yeh MY, Weng HH, and Su CH. Effects of Dehydration on Brain Perfusion and Infarct Core After Acute Middle Cerebral Artery Occlusion in Rats: Evidence From High-Field Magnetic Resonance Imaging. Front Neurol 2018; 9:786. DOI: `10.3389/fneur.2018.00786`. Available from: `https://www.ncbi.nlm.nih.gov/pubmed/30294297`

91. Watso JC and Farquhar WB. Hydration Status and Cardiovascular Function. Nutrients 2019; 11. DOI: `10.3390/nu11081866`. Available from: `https://www.ncbi.nlm.nih.gov/pubmed/31405195`

92. Ryding E. The Relationship between Intracranial Pressure Increase and Volume of Brain Compression. J Neurol Neurophysiol 2017; 8:436. DOI: `10.4172/2155-9562.1000436`

93. McGarry MD, Johnson CL, Sutton BP, Georgiadis JG, Van Houten EE, Pattison AJ, Weaver JB, and Paulsen KD. Suitability of poroelastic and viscoelastic mechanical models for high and low frequency MR elastography. Med Phys 2015; 42:947–57. DOI: `10.1118/1.4905048`. Available from: `https://www.ncbi.nlm.nih.gov/pubmed/25652507`

94. McGarry M, Van Houten E, Solamen L, Gordon-Wylie S, Weaver J, and Paulsen K. Uniqueness of poroelastic and viscoelastic nonlinear inversion MR elastography at low frequencies. Phys Med Biol 2019; 64:075006. DOI: `10.1088/1361-6560/ab0a7d`. Available from: `https://www.ncbi.nlm.nih.gov/pubmed/30808018`

95. Donnelly J, Aries MJ, and Czosnyka M. Further understanding of cerebral autoregulation at the bedside: possible implications for future therapy. Expert Rev Neurother 2015; 15:169–85. DOI: `10.1586/14737175.2015.996552`. Available from: `https://www.ncbi.nlm.nih.gov/pubmed/25614952`

96. Moerman A and De Hert S. Why and how to assess cerebral autoregulation? Best Pract Res Clin Anaesthesiol 2019; 33:211–20. DOI: `10.1016/j.bpa.2019.05.007`. Available from: `https://www.ncbi.nlm.nih.gov/pubmed/31582100`

97. Pstras L, Thomaseth K, Waniewski J, Balzani I, and Bellavere F. The Valsalva manoeuvre: physiology and clinical examples. Acta Physiol (Oxf) 2016; 217:103–19. DOI: `10.1111/apha.12639`. Available from: `https://www.ncbi.nlm.nih.gov/pubmed/26662857`

98. Sarica A, Curcio M, Rapisarda L, Cerasa A, Quattrone A, and Bono F. Periventricular white matter changes in idiopathic intracranial hypertension. Ann Clin Transl Neurol 2019; 6:233–42. DOI: 10.1002/acn3.685. Available from: https://www.ncbi.nlm.nih.gov/pubmed/30847356

99. Eidsvaag VA, Hansson HA, Heuser K, Nagelhus EA, and Eide PK. Cerebral microvascular abnormalities in patients with idiopathic intracranial hypertension. Brain Res 2018; 1686:72–82. DOI: 10.1016/j.brainres.2018.02.017. Available from: https://www.ncbi.nlm.nih.gov/pubmed/29477544

100. Chisholm JT, Sudhakar P, Alhajeri AN, and Smith JH. Intracranial elastance is increased in idiopathic intracranial hypertension. Eur J Neurol 2017; 24:1457–63. DOI: 10.1111/ene.13410. Available from: https://www.ncbi.nlm.nih.gov/pubmed/28800199

101. Kolipaka A, Wassenaar PA, Cha S, Marashdeh WM, Mo X, Kalra P, Gans B, Raterman B, and Bourekas E. Magnetic resonance elastography to estimate brain stiffness: Measurement reproducibility and its estimate in pseudotumor cerebri patients. Clin Imaging 2018; 51:114–22. DOI: 10.1016/j.clinimag.2018.02.005. Available from: https://www.ncbi.nlm.nih.gov/pubmed/29459315

102. Solamen LM, McGarry MDJ, Fried J, Weaver JB, Lollis SS, and Paulsen KD. Poroelastic Mechanical Properties of the Brain Tissue of Normal Pressure Hydrocephalus Patients During Lumbar Drain Treatment Using Intrinsic Actuation MR Elastography. Acad Radiol 2020. DOI: 10.1016/j.acra.2020.03.009. Available from: https://www.ncbi.nlm.nih.gov/pubmed/32331966

103. Yin Z, Romano AJ, Manduca A, Ehman RL, and Huston J. 3. Stiffness and Beyond: What MR Elastography Can Tell Us About Brain Structure and Function Under Physiologic and Pathologic Conditions. Top Magn Reson Imaging 2018; 27:305–18. DOI: 10.1097/RMR.0000000000000178. Available from: https://www.ncbi.nlm.nih.gov/pubmed/30289827

104. Murphy MC, Huston J. 3, and Ehman RL. MR elastography of the brain and its application in neurological diseases. Neuroimage 2019; 187:176–83. DOI: 10.1016/j.neuroimage.2017.10.008. Available from: https://www.ncbi.nlm.nih.gov/pubmed/28993232

105. Hiscox LV, Johnson CL, Barnhill E, McGarry MD, Huston J, Beek EJ van, Starr JM, and Roberts N. Magnetic resonance elastography (MRE) of the human brain: technique, findings and clinical applications. Phys Med Biol 2016; 61:R401–R437. DOI: 10.1088/0031-9155/61/24/R401. Available from: https://www.ncbi.nlm.nih.gov/pubmed/27845941

106. Bigot M, Chauveau F, Beuf O, and Lambert SA. Magnetic Resonance Elastography of Rodent Brain. Front Neurol 2018; 9:1010. DOI: 10.3389/fneur.2018.01010. Available from: https://www.ncbi.nlm.nih.gov/pubmed/30538670

107. Streitberger KJ, Wiener E, Hoffmann J, Freimann FB, Klatt D, Braun J, Lin K, McLaughlin J, Sprung C, Klingebiel R, and Sack I. In vivo viscoelastic properties of the brain in normal pressure hydrocephalus. NMR Biomed 2011; 24:385–92. DOI: `10.1002/nbm.1602`. Available from: `https://www.ncbi.nlm.nih.gov/pubmed/20931563`

108. Bertalan G, Boehm-Sturm P, Schreyer S, Morr AS, Steiner B, Tzschatzsch H, Braun J, Guo J, and Sack I. The influence of body temperature on tissue stiffness, blood perfusion, and water diffusion in the mouse brain. Acta Biomater 2019; 96:412–20. DOI: `10.1016/j.actbio.2019.06.034`. Available from: `https://www.ncbi.nlm.nih.gov/pubmed/31247381%20https://www.sciencedirect.com/science/article/abs/pii/S1742706119304477?via%3Dihub`

109. Bertalan G, Klein C, Schreyer S, Steiner B, Kreft B, Tzschatzsch H, Schellenberger AA de, Nieminen-Kelha M, Braun J, Guo J, and Sack I. Biomechanical properties of the hypoxic and dying brain quantified by magnetic resonance elastography. Acta Biomater 2020; 101:395–402. DOI: `10.1016/j.actbio.2019.11.011`. Available from: `https://www.ncbi.nlm.nih.gov/pubmed/31726251`

110. Tan L, McGarry MDJ, Van Houten EEW, Ji M, Solamen L, Zeng W, Weaver JB, and Paulsen KD. A numerical framework for interstitial fluid pressure imaging in poroelastic MRE. PLoS One 2017; 12:e0178521. DOI: `10.1371/journal.pone.0178521`. Available from: `https://www.ncbi.nlm.nih.gov/pubmed/28586393`

111. Baranger J, Mertens L, and Villemain O. Blood Flow Imaging with Ultrafast Doppler. J Vis Exp 2020. DOI: `10.3791/61838`. Available from: `https://www.ncbi.nlm.nih.gov/pubmed/33135687`

Eidesstattliche Erklärung

„Ich, Bernhard Kreft, versichere an Eides statt durch meine eigenhändige Unterschrift, dass ich die vorgelegte Dissertation mit dem Thema: „Development and validation of in vivo ultrasound time-harmonic elastography on the human brain towards clinical application/ Entwicklung und Validierung der in vivo zeitharmonischen Ultraschall-Elastografie des menschlichen Gehirns für die klinische Anwendung“ selbstständig und ohne nicht offengelegte Hilfe Dritter verfasst und keine anderen als die angegebenen Quellen und Hilfsmittel genutzt habe.

Alle Stellen, die wörtlich oder dem Sinne nach auf Publikationen oder Vorträgen anderer Autoren/innen beruhen, sind als solche in korrekter Zitierung kenntlich gemacht. Die Abschnitte zu Methodik (insbesondere praktische Arbeiten, Laborbestimmungen, statistische Aufarbeitung) und Resultaten (insbesondere Abbildungen, Graphiken und Tabellen) werden von mir verantwortet.

Ich versichere ferner, dass ich die in Zusammenarbeit mit anderen Personen generierten Daten, Datenauswertungen und Schlussfolgerungen korrekt gekennzeichnet und meinen eigenen Beitrag sowie die Beiträge anderer Personen korrekt kenntlich gemacht habe (siehe Anteilserklärung). Texte oder Textteile, die gemeinsam mit anderen erstellt oder verwendet wurden, habe ich korrekt kenntlich gemacht. Meine Anteile an etwaigen Publikationen zu dieser Dissertation entsprechen denen, die in der untenstehenden gemeinsamen Erklärung mit dem/der Erstbetreuer/in, angegeben sind. Für sämtliche im Rahmen der Dissertation entstandenen Publikationen wurden die Richtlinien des ICMJE (International Committee of Medical Journal Editors; www.icmje.og) zur Autorenschaft eingehalten. Ich erkläre ferner, dass ich mich zur Einhaltung der Satzung der Charité – Universitätsmedizin Berlin zur Sicherung Guter Wissenschaftlicher Praxis verpflichte.

Weiterhin versichere ich, dass ich diese Dissertation weder in gleicher noch in ähnlicher Form bereits an einer anderen Fakultät eingereicht habe.

Die Bedeutung dieser eidesstattlichen Versicherung und die strafrechtlichen Folgen einer unwahren eidesstattlichen Versicherung (§§156, 161 des Strafgesetzbuches) sind mir bekannt und bewusst.“

Datum Unterschrift

Anteilserklärung an den erfolgten Publikationen

Bernhard Kreft hatte folgenden Anteil an den folgenden Publikationen:

Publikation 1: Kreft Bernhard; Tzschätzsch Heiko; Schrank Felix; Bergs Judith; Streitberger Kaspar-Josche; Wäldchen Stephan; Hetzer Stefan; Braun Jürgen; Sack Ingolf, Time-Resolved Response of Cerebral Stiffness to Hypercapnia in Humans, Ultrasound in Medicine and Biology, 2020.

Beitrag im Einzelnen: Die ursprüngliche Idee für die Anwendung der Ultraschall-Elastographie der zweiten Harmonischen auf das menschliche Gehirn wurde von Prof. Sack, Dr. Tzschätzsch und Dr. Braun entwickelt. In enger Zusammenarbeit mit Dr. Tzschätzsch habe ich dann den bestehenden Aufbau für abdominale Anwendungen genutzt, um die Ultraschall-Zeitharmonische-Elastographie-Anwendung für das menschliche Gehirn zu entwickeln. Die von mir durchgeführte Entwicklung des Verfahrens führte zu den in Abbildung 2 gezeigten B-Mode- und Elastographie-Bildern. In enger Zusammenarbeit mit Prof. Sack, Dr. Tzschätzsch, Dr. Streitberger, Dr. Bergs und Dr. Hetzer stellte ich die anfängliche Hypothese auf, dass Hyperkapnie und die daraus resultierende Zunahme der zerebralen Perfusion mit den mechanischen Eigenschaften des Gehirns gekoppelt sein könnten. Anschließend recherchierte ich in der Literatur, wie Hyperkapnie bei gesunden Probanden effektiv induziert werden kann, woraufhin ich in Zusammenarbeit mit Prof. Sack, Dr. Tzschätzsch, Dr. Bergs und Dr. Hetzer den in Abbildung 1 dargestellten Versuchsaufbau entwickelte. Außerdem entwickelte ich in enger Zusammenarbeit mit Dr. Braun eine Halterung für die Ultraschallsonde, um ungewollte Bewegungen während der Messung zu vermeiden (siehe Abbildung 1a). Ich rekrutierte die Probanden, informierte sie sowohl über das Messverfahren als auch den experimentellen Ablauf und führte die Datenerhebung durch, die zu den in Tabelle 1 zusammengefassten physiologischen Parametern und den Elastographie- und B-Mode-Bildern für jeden Probanden führte, welche in Abbildung 3 dargestellt sind. Ich zeichnete die, ebenfalls in Abbildung 3 dargestellten, Bereiche von Interesse in die Bilder ein und analysierte die Daten vollständig in Matlab mit der beratenden Unterstützung von Prof. Sack, Dr. Tzschätzsch, S. Wäldchen, F. Schrank und Dr. Bergs, woraus Tabelle 2 und die Abbildungen 4 und 5 entstanden. Der erste Entwurf des Manuskripts wurde von mir mit Unterstützung von Dr. Tzschätzsch geschrieben und redigiert, während alle Autoren zur sorgfältigen und kritischen Überarbeitung des endgültigen Entwurfs beitrugen. Alle in der Veröffentlichung gezeigten Tabellen und Abbildungen wurden von mir erstellt und sind das Ergebnis meiner Datenanalyse und statistischen Tests. Die Einreichung und die anschließenden Überarbeitungen erfolgten ausschließlich durch mich, mit wertvollen Beiträgen von allen Autoren.

Publikation 2: Kreft Bernhard; Bergs Judith; Shahryari Mehrgan; Danyel Leon Alexander; Hetzer Stefan; Braun Jürgen; Sack Ingolf; Tzschätzsch Heiko, Cerebral Ultrasound Time-Harmonic Elastography Reveals Softening of the Human Brain Due to Dehydration, Frontiers in Physiology, 2020.

Beitrag im Einzelnen: Die ursprüngliche Idee für die Anwendung der zeitharmonischen Ultraschall-Elastographie am menschlichen Gehirn wurde von Prof. Sack, Dr. Tzschätzsch und Dr. Braun entwickelt. In enger Zusammenarbeit mit Dr. Tzschätzsch habe ich dann den bestehenden Aufbau für abdominale Anwendungen genutzt, um die Ultraschall-Zeitharmonische Elastographie-Anwendung für das menschliche Gehirn zu entwickeln, woraus der in Abbildung 2 dargestellte Versuchsaufbau resultierte. In Zusammenarbeit mit allen Mitautoren formulierte ich die Hypothese, dass Dehydratation und Rehydratation zu perfusionsbedingten Veränderungen der mechanischen Eigenschaften des Gehirns führen. Gemeinsam mit Dr. Bergs führte ich die Literaturrecherche bezüglich der Zeitdauer und der Quantifizierung von Dehydratation durch, und entwickelte auf dieser Grundlage den experimentellen Ablauf des Experimentes in Zusammenarbeit mit Dr. Bergs, Dr. Tzschätzsch, Prof. Sack, Dr. Danyel und M. Shahryari. Hieraus resultierte das Flussdiagram in Abbildung 1. Ich rekrutierte die Probanden, informierte sie über das Messverfahren und sorgte für eine ausreichende Flüssigkeitszufuhr vor der Messung. In Zusammenarbeit mit M. Shahryari führte ich die Datenerfassung durch und fasste die erhobenen Werte in den Tabellen 1 und 2 zusammen. Während ich physiologische Parameter wie Alter, Geschlecht, Herzfrequenz und Blutdruck sowie Elastographie-Rohdaten erfasste, sammelte M. Shahryari Blut- und Urinproben, die separat analysiert wurden. Ich verarbeitete die Elastographie-Rohdaten und erstellte für jeden Probanden B-Mode-Bilder und Elastogramme, wie in Abbildung 3 beispielhaft dargestellt. Ich zeichnete die Regionen von Interesse, welche ebenfalls in Abbildung 3 gezeigt sind, und analysierte die Daten mit Hilfe der beratenden Unterstützung aller Mitautoren. Auf Grundlage meiner Datenauswertung entstanden die Abbildungen 4 und 5. Der erste Entwurf des Manuskripts wurde von mir mit der Unterstützung von Dr. Tzschätzsch verfasst und redigiert, während alle Autoren zur sorgfältigen und kritischen Überarbeitung des endgültigen Entwurfs beitrugen. Alle in der Veröffentlichung gezeigten Tabellen und Abbildungen wurden von mir erstellt und sind das Ergebnis meiner Datenanalyse und statistischen Tests. Die Einreichung und die anschließenden Überarbeitungen erfolgten ausschließlich durch mich, mit wertvollen Beiträgen von allen Autoren.

Publikation 3: Kreft Bernhard; Tzschätzsch Heiko; Shahryari Mehrgan; Haffner Paula; Braun Jürgen Braun; Sack Ingolf; Streitberger Kaspar-Josche, Noninvasive Detection of Intracranial Hypertension by Novel Ultrasound Time-Harmonic Elastography, Investigative Radiology, 2021.

Beitrag im Einzelnen: Die ursprüngliche Idee für die Anwendung der zeitharmonischen Ultraschall-Elastographie am menschlichen Gehirn wurde von Prof. Sack, Dr. Tzschätzsch und Dr. Braun entwickelt. In enger Zusammenarbeit mit Dr. Tzschätzsch habe ich dann den bestehenden Aufbau für abdominale Anwendungen genutzt, um die Anwendung der Ultraschall-Elastographie der zweiten Harmonischen auf das menschliche Gehirn zu entwickeln. Das Ergebnis ist der in Abbildung 2 gezeigte Versuchsaufbau und die in Abbildung 3 gezeigten B-Mode-Bilder. In Zusammenarbeit mit Dr. Streitberger, Dr. Tzschätzsch und Prof. Sack formulierte ich die Hypothese, dass ein veränderter intrakranieller Druck mit veränderten mechanischen Eigenschaften des Gehirns einhergeht. Die Idee, die idiopathische intrakranielle Hypertonie als Modellerkrankung für diese Pilotstudie zu untersuchen, stammte ursprünglich von Dr. Streitberger und Dr. Haffner und wurde von mir nach einer gründlichen Literaturrecherche in ein experimentelles Verfahren umgesetzt, das ich anhand des Flussdiagramms in Abbildung 1 darstellte. Während ich für die Rekrutierung der gesunden Probanden verantwortlich war, wurde die Rekrutierung, die medizinische Aufklärung, die Diagnose und die Behandlung der Patienten von Dr. Streitberger und Dr. Haffner durchgeführt. Ich erfasste alle klinischen Parameter der gesunden Probanden und fasste sie in Tabelle 2 zusammen. Ich erfasste und prozessierte auch alle Elastographie-Daten. Das Ergebnis der Prozessierung sind die B-Mode- und Elastogramme in Abbildung 4. Darüber hinaus zeichnete ich alle Regionen von Interesse ein und analysierte die Daten. Diese Analyse habe ich zusammen mit den von Dr. Streitberger und Dr. Haffner erhobenen Daten aus der Lumbalpunktion der Patienten in Tabelle 1 zusammengefasst. Die Gruppenanalyse und die Analyse der diagnostischen Leistung der Methode hinsichtlich der idiopathischen intrakraniellen Hypertension wurden von mir durchgeführt und in Abbildung 5 dargestellt. Darüber hinaus habe ich die Parameterkorrelationen berechnet und in Abbildung 6 dargestellt. Dr. Tzschätzsch, Dr. Streitberger, M. Shahryari und Prof. Sack standen mir bei allen Aspekten der Datenanalyse beratend zur Seite. Der erste Entwurf des Manuskripts wurde von mir mit Unterstützung von Dr. Tzschätzsch und Dr. Streitberger geschrieben und redigiert, während alle Autoren zur sorgfältigen und kritischen Überarbeitung des endgültigen Entwurfs beitrugen. Alle in der Veröffentlichung gezeigten Tabellen und Abbildungen wurden von mir erstellt und sind das Ergebnis meiner Datenanalyse und statistischen Tests. Die Einreichung und die anschließenden Überarbeitungen erfolgten ausschließlich durch mich, mit wertvollen Beiträgen von allen Autoren.

Unterschrift des Doktoranden/der Doktorandin

Journal Data Filtered By: **Selected JCR Year: 2017** Selected Editions: SCIE,SSCI Selected Categories: **'ACOUSTICS'** Selected Category Scheme: WoS

Gesamtanzahl: 26 Journale

Rank	Full Journal Title	Total Cites	Journal Impact Factor	Eigenfactor Score
1	ULTRASONICS SONOCHEMISTRY	14,026	6.012	0.014300
2	ULTRASOUND IN OBSTETRICS & GYNECOLOGY	12,420	5.654	0.018800
3	ULTRASCHALL IN DER MEDIZIN	2,201	4.389	0.004310
4	EURASIP Journal on Audio Speech and Music Processing	377	3.057	0.001040
5	IEEE-ACM Transactions on Audio Speech and Language Processing	1,938	2.950	0.005510
6	IEEE TRANSACTIONS ON ULTRASONICS FERROELECTRICS AND FREQUENCY CONTROL	10,448	2.704	0.009840
7	ULTRASOUND IN MEDICINE AND BIOLOGY	10,316	2.645	0.013440
8	JOURNAL OF SOUND AND VIBRATION	33,536	2.618	0.026300
9	ULTRASONICS	6,518	2.377	0.009140
10	ULTRASONIC IMAGING	1,076	2.300	0.000690
11	JOURNAL OF VIBRATION AND CONTROL	4,131	2.197	0.007690
12	SHOCK AND VIBRATION	2,470	1.857	0.006280
13	JOURNAL OF VIBRATION AND ACOUSTICS-TRANSACTIONS OF THE ASME	3,734	1.777	0.004440
14	WAVE MOTION	2,090	1.723	0.003730
15	APPLIED ACOUSTICS	4,739	1.721	0.006750
16	JOURNAL OF THE ACOUSTICAL SOCIETY OF AMERICA	44,946	1.605	0.026990
17	SPEECH COMMUNICATION	3,266	1.585	0.003040
18	JOURNAL OF ULTRASOUND IN MEDICINE	6,500	1.530	0.008700

Kreft B, Tzschätzsch H, Schrank F, Bergs J, Streitberger KJ, Wäldchen S, Hetzer S, Braun J, Sack I. Time-Resolved Response of Cerebral Stiffness to Hypercapnia in Humans. Ultrasound Med Biol. 2020 Apr;46(4):936-943. Epub 2020 Jan 28.

doi: https://doi.org/10.1016/j.ultrasmedbio.2019.12.019.

Erratum in: Ultrasound Med Biol. 2020 Jun;46(6):1551

doi: https://doi.org/10.1016/j.ultrasmedbio.2020.02.009.

Journal Data Filtered By: **Selected JCR Year: 2019** Selected Editions: SCIE,SSCI Selected Categories: **“PHYSIOLOGY”** Selected Category Scheme: WoS

Gesamtanzahl: 81 Journale

Rank	Full Journal Title	Total Cites	Journal Impact Factor	Eigenfactor Score
1	PHYSIOLOGICAL REVIEWS	28,712	25.588	0.024010
2	Annual Review of Physiology	9,466	19.556	0.010190
3	JOURNAL OF PINEAL RESEARCH	10,537	14.528	0.009430
4	PHYSIOLOGY	3,583	7.212	0.005380
5	International Journal of Behavioral Nutrition and Physical Activity	11,154	6.714	0.018870
6	Comprehensive Physiology	4,877	6.604	0.009170
7	JOURNAL OF CELLULAR PHYSIOLOGY	26,456	5.546	0.024290
8	Acta Physiologica	5,106	5.542	0.008320
9	EXERCISE AND SPORT SCIENCES REVIEWS	3,290	4.915	0.002720
10	Reviews of Physiology Biochemistry and Pharmacology	805	4.700	0.000670
11	JOURNAL OF PHYSIOLOGY-LONDON	50,045	4.547	0.037090
12	AMERICAN JOURNAL OF PHYSIOLOGY-LUNG CELLULAR AND MOLECULAR PHYSIOLOGY	13,085	4.406	0.015510
13	AMERICAN JOURNAL OF PHYSIOLOGY-HEART AND CIRCULATORY PHYSIOLOGY	26,114	3.864	0.020400
14	AMERICAN JOURNAL OF PHYSIOLOGY-GASTROINTESTINAL AND LIVER PHYSIOLOGY	14,186	3.725	0.012280
15	PSYCHOPHYSIOLOGY	14,586	3.692	0.012670
16	JOURNAL OF GENERAL PHYSIOLOGY	7,476	3.628	0.007380
17	International Journal of Sports Physiology and Performance	5,072	3.528	0.009760

Rank	Full Journal Title	Total Cites	Journal Impact Factor	Eigenfactor Score
18	AMERICAN JOURNAL OF PHYSIOLOGY-CELL PHYSIOLOGY	15,502	3.485	0.010450
19	AMERICAN JOURNAL OF PHYSIOLOGY-ENDOCRINOLOGY AND METABOLISM	18,917	3.469	0.013710
20	Frontiers in Physiology	21,190	3.367	0.052500
21	JOURNAL OF MAMMARY GLAND BIOLOGY AND NEOPLASIA	1,951	3.293	0.001080
22	CLINICAL JOURNAL OF SPORT MEDICINE	4,242	3.165	0.005100
23	PFLUGERS ARCHIV-EUROPEAN JOURNAL OF PHYSIOLOGY	9,355	3.158	0.009810
24	AMERICAN JOURNAL OF PHYSIOLOGY-RENAL PHYSIOLOGY	16,035	3.144	0.017010
25	JOURNAL OF BIOLOGICAL RHYTHMS	3,258	3.122	0.003220
26	JOURNAL OF APPLIED PHYSIOLOGY	43,194	3.044	0.020180
27	AMERICAN JOURNAL OF PHYSIOLOGY-REGULATORY INTEGRATIVE AND COMPARATIVE PHYSIOLOGY	17,896	2.992	0.013690
28	Journal of Physiological Sciences	1,380	2.955	0.002160
29	JOURNAL OF PHYSIOLOGY AND BIOCHEMISTRY	1,854	2.952	0.002340
30	PESTICIDE BIOCHEMISTRY AND PHYSIOLOGY	5,930	2.751	0.005660
31	PHYSIOLOGICAL GENOMICS	4,535	2.749	0.004520
32	INTERNATIONAL JOURNAL OF BIOMETEOROLOGY	6,418	2.680	0.007220
33	JOURNAL OF PHYSIOLOGY AND PHARMACOLOGY	3,342	2.644	0.002740
34	INTERNATIONAL JOURNAL OF PSYCHOPHYSIOLOGY	8,822	2.631	0.009440
35	EUROPEAN JOURNAL OF APPLIED PHYSIOLOGY	16,418	2.580	0.012130

Selected JCR Year: 2019; Selected Categories: “PHYSIOLOGY”

frontiers
in Physiology

ORIGINAL RESEARCH
published: 11 January 2021
doi: 10.3389/fphys.2020.616984

Cerebral Ultrasound Time-Harmonic Elastography Reveals Softening of the Human Brain Due to Dehydration

Bernhard Kreft[1], Judith Bergs[2], Mehrgan Shahryari[2], Leon Alexander Danyel[3], Stefan Hetzer[4], Jürgen Braun[1], Ingolf Sack[2] and Heiko Tzschätzsch[2]*

[1]Institute of Medical Informatics, Charité–Universitätsmedizin Berlin, Berlin, Germany, [2]Department of Radiology, Charité–Universitätsmedizin Berlin, Berlin, Germany, [3]Department of Neurology, Charité–Universitätsmedizin Berlin, Berlin, Germany, [4]Bernstein Center of Advanced Neuroimaging, Charité–Universitätsmedizin Berlin, Berlin, Germany

OPEN ACCESS

Edited by:
Simon Chatelin,
UMR7357 Laboratoire des sciences de l'Ingénieur, de l'Informatique et de l'Imagerie (ICube), France

Reviewed by:
Jonathan Vappou,
UMR7357 Laboratoire des sciences de l'Ingénieur, de l'Informatique et de l'Imagerie (ICube), France
Kevin Parker,
University of Rochester, United States

***Correspondence:**
Heiko Tzschätzsch
heiko.tzschaetzsch@charite.de

Specialty section:
This article was submitted to Medical Physics and Imaging, a section of the journal Frontiers in Physiology

Received: *13 October 2020*
Accepted: *09 December 2020*
Published: *11 January 2021*

Citation:
Kreft B, Bergs J, Shahryari M, Danyel LA, Hetzer S, Braun J, Sack I and Tzschätzsch H (2021) Cerebral Ultrasound Time-Harmonic Elastography Reveals Softening of the Human Brain Due to Dehydration. Front. Physiol. 11:616984. doi: 10.3389/fphys.2020.616984

Hydration influences blood volume, blood viscosity, and water content in soft tissues – variables that determine the biophysical properties of biological tissues including their stiffness. In the brain, the relationship between hydration and stiffness is largely unknown despite the increasing importance of stiffness as a quantitative imaging marker. In this study, we investigated cerebral stiffness (CS) in 12 healthy volunteers using ultrasound time-harmonic elastography (THE) in different hydration states: (i) during normal hydration, (ii) after overnight fasting, and (iii) within 1 h of drinking 12 ml of water per kg body weight. In addition, we correlated shear wave speed (SWS) with urine osmolality and hematocrit. SWS at normal hydration was 1.64 ± 0.02 m/s and decreased to 1.57 ± 0.04 m/s ($p < 0.001$) after overnight fasting. SWS increased again to 1.63 ± 0.01 m/s within 30 min of water drinking, returning to values measured during normal hydration ($p = 0.85$). Urine osmolality at normal hydration (324 ± 148 mOsm/kg) increased to 784 ± 107 mOsm/kg ($p < 0.001$) after fasting and returned to normal (288 ± 128 mOsm/kg, $p = 0.83$) after water drinking. SWS and urine osmolality correlated linearly ($r = -0.68$, $p < 0.001$), while SWS and hematocrit did not correlate ($p = 0.31$). Our results suggest that mild dehydration in the range of diurnal fluctuations is associated with significant softening of brain tissue, possibly due to reduced cerebral perfusion. To ensure consistency of results, it is important that cerebral elastography with a standardized protocol is performed during normal hydration.

Keywords: brain, elastography, hydration, ultrasound, time-harmonic elastography

INTRODUCTION

The body water content ranges between 55 and 60% in adults and varies with age, sex, and body constitution, while human brain tissue has a very high water content of about 75% (Mitchell et al., 1945), underlining the importance of adequate cerebral tissue hydration for normal brain function. The human organism can easily adapt to a water deficit of 2–3%; however, beyond this limit, dehydration can impair mental and physical coordination, eventually leading to a fatal breakdown of vital body functions (Ashcroft, 2001). Clinically, three types of dehydration are distinguished: (i) isotonic dehydration, that is loss of body water and salt usually occurring after excessive vomiting, diarrhea or bleeding, (ii) hypotonic dehydration, in which salt loss outweighs water loss, is often associated with the intake of diuretic drugs or kidney damage, and (iii) hypertonic dehydration, often resulting from a lack of water due to fasting or dehydration (Spital, 2007; Bhave and Neilson, 2011; Jablonski, 2012). The diagnosis of chronic dehydration remains challenging since clinical signs such as dry mucous membranes or dry skin are unspecific (Jequier and Constant, 2010) while blood or urine markers can vary markedly among individuals (Armstrong, 2005; Duning et al., 2005; Patterson et al., 2008).

The hydration state of soft tissues affects a variety of biophysical properties, which can be assessed *in vivo* by MRI or ultrasound. While perfusion MRI, flow MRI, and Doppler ultrasound are sensitive to volume and velocity of blood flow, magnetic resonance elastography (MRE) and ultrasound elastography can non-invasively measure stiffness (Sack and Schaeffter, 2018). Hydration-specific imaging markers are potentially important for the management of neurological diseases since dehydration of brain tissue is a frequent and dangerous condition in elderly patients with Alzheimer's disease or other types of dementia (Lauriola et al., 2018).

Studies using MRI and ultrasound markers show that dehydration reduces cerebral blood flow (Trangmar et al., 2014, 2015), decreases brain parenchymal volume, and increases ventricular volume (Duning et al., 2005; Streitburger et al., 2012). However, to date no studies have been published that investigated the effect of dehydration on cerebral stiffness (CS).

Our hypothesis is that CS changes with dehydration and water drinking similar to stiffness changes reported for other organs (Guo et al., 2018). For instance, it has been shown that liver stiffness increases with water ingestion and hepatic blood flow (Ipek-Ugay et al., 2016; Tzschatzsch et al., 2016b). The opposite effect, i.e., softening, has been observed in the pancreas and spleen (Dittmann et al., 2017) while kidney stiffness has been reported to change only slightly with increasing bladder filling (Gandhi et al., 2020) and hydration (Marticorena Garcia et al., 2018).

In this study, we investigate the effect of dehydration on CS using cerebral time-harmonic elastography (THE), which utilizes multifrequency vibrations induced in the brain by an external driver in combination with transtemporal ultrasound (Tzschatzsch et al., 2018). Cerebral THE has several advantages over MRE such as being available at the bedside and providing instantaneous feedback, which facilitates identification of rapid CS changes. We will exploit this real-time feedback capability of THE to study possible CS changes induced by dehydration of brain tissue after overnight fasting and water drinking. Overall, this study aims at providing insight into the sensitivity of CS to physiological changes in tissue hydration toward a clinical tool for monitoring brain mechanical properties at the bedside.

MATERIALS AND METHODS

Study Design

The study protocol conformed to the guidelines of the Declaration of Helsinki and was approved by the institutional review board of Charité–Universitätsmedizin Berlin (EA1/242/18). All study participants gave their written consent to conduct the experiment as well as for the publication of any potentially identifiable images or data included in this article. Inclusion criteria were absence of any history of cerebral disease or trauma and no impairment of renal function. Insufficient acoustic windows due to high skull thickness cause relatively high dropout rates of around 10% in studies of transcranial ultrasound (Marinoni et al., 1997). To avoid such dropout rates, we checked the acoustic window previously to the measurements. Finally, a total of 12 volunteers (3/9 females/males; mean age of 33 ± 9 years, range: 22–50 years) with a sufficient transcranial bone window were included in the study, while one volunteer did not meet the inclusion criterion. Two volunteers (#5 and #12) were further excluded from statistical group analysis due to incomplete fasting. Volunteer demographic data, including sex, age, and body mass index (BMI) are summarized in **Table 1**.

Each participant was investigated on 2 days. On the first day, data were acquired in a normally hydrated (NH) state, defined as drinking 1.5 L water within 5 h prior to the examination. After 12-h overnight fasting, the second set of data (dehydrated, DH) was acquired. Then, the volunteers were asked to drink 12 ml/kg of water within 15 min (Duning et al., 2005). Immediately after drinking water, four sets of data (rehydrated, RH1–RH4) were acquired at 15-min intervals. Thus, a total of six sets of data were acquired for every volunteer. Each dataset consisted of THE, transcranial Doppler (TCD), and recordings of blood pressure and heart rate. Urine and blood were collected at hydration states 1 (NH), 2 (DH), and 6 (RH4) to determine urine osmolality and hematocrit. The time sequence of THE examinations is illustrated in **Figure 1**.

Cerebral THE

The setup of cerebral THE including (i) customized vibration bed with vibration plate mounted on a shaker (GAMPT, Merseburg, Germany), (ii) standard clinical ultrasound scanner

TABLE 1 | Demographic data, including sex, age, and BMI with group mean and standard deviation (SD) of all volunteers.

Subject #	Sex	Age in years	BMI in kg/m^2
1	m	25	23.2
2	m	50	20.1
3	f	40	21.5
4	f	27	31.6
5	m	26	20.2
6	m	35	19.9
7	m	46	25.8
8	f	28	20.7
9	m	37	26.2
10	m	22	24.0
11	m	22	24.5
12	m	43	23.6
Mean (SD)		33.4 (9.3)	23.4 (3.5)

Volunteers #5 and #12 were excluded from statistical analysis due to poor compliance with the study protocol.

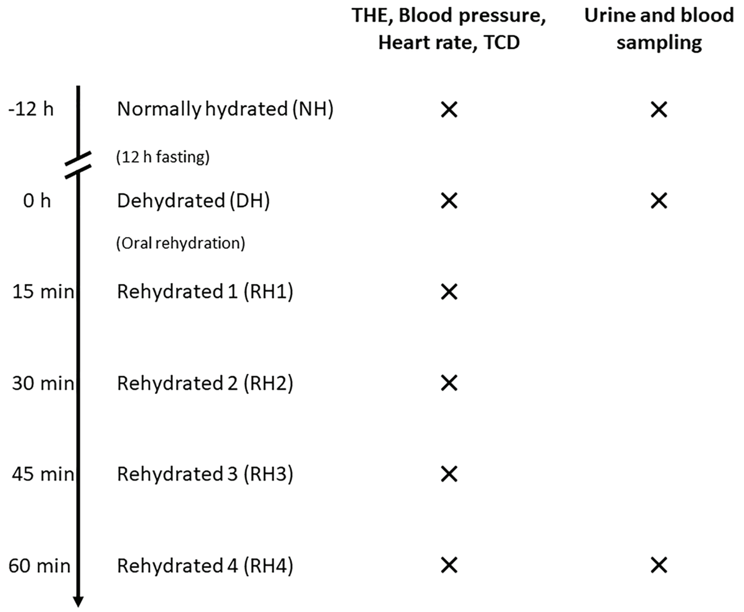

		THE, Blood pressure, Heart rate, TCD	Urine and blood sampling
-12 h	Normally hydrated (NH)	×	×
	(12 h fasting)		
0 h	Dehydrated (DH)	×	×
	(Oral rehydration)		
15 min	Rehydrated 1 (RH1)	×	
30 min	Rehydrated 2 (RH2)	×	
45 min	Rehydrated 3 (RH3)	×	
60 min	Rehydrated 4 (RH4)	×	×

FIGURE 1 | Time sequence of THE examinations in volunteers. Volunteers were first examined in a normally hydrated state (NH). After a 12-h-fasting period, measurements were conducted in the dehydrated state (DH). Then, four sets of data in different hydration states were acquired after oral rehydration (RH1–RH4) at 15-min intervals. For every hydration state, time-harmonic elastography (THE), transcranial Doppler (TCD), and blood pressure and heart rate measurements were performed. Urine and blood for determination of urine osmolality and hematocrit were sampled at hydration states NH, DH, and RH4.

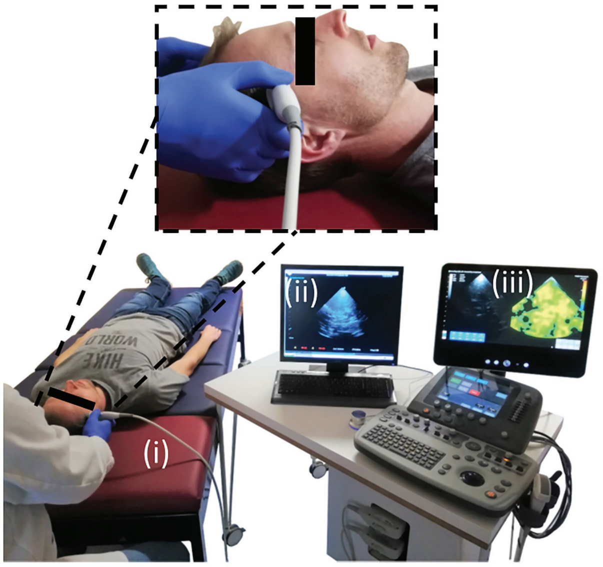

FIGURE 2 | Experimental setup for conduct of cerebral THE. The setup comprised of three main components: (i) the customized patient bed with the vibration plate (red), (ii) the clinical ultrasound scanner, and (iii) the elastography computer with the integrated post-processing software. The magnification shows the positioning of the ultrasound probe over the volunteer's temporal bone window for transcranial ultrasound.

(SonixMDP, UltraSonix, Scottsdale AZ, United States) equipped with a phased-array transducer (SA4-2/24), and (iii) elastography computer with the integrated post-processing pipeline is illustrated in **Figure 2**. The volunteers were asked to lie in a supine position with the head on the vibration plate. According to the current guidelines for transcranial ultrasound (Brian D Coley et al., 2012), the probe was positioned for imaging through the temporal bone window, as shown in the magnification in **Figure 2**. Shear waves were induced in the head by applying a multifrequency waveform comprising six frequencies (27, 33, 39, 44, 50, and 56 Hz). Signal-to-noise-ratio (SNR) in transcranial ultrasound is known to be relatively low compared to abdominal ultrasound. The stability of shear wave speed (SWS) estimation was found to be stable at vibration amplitudes larger than 2 μm. Therefore, we ensured that vibration amplitudes were above this threshold in order to compensate for low SNR. For data acquisition, a basic preset for transcranial Doppler ultrasound was adapted from the UltraSonix-System (Phased Array, Vascular, TCD, 3.3 MHz). To further improve image SNR, number of pulse cycles was increased to two. In addition, the frame rate was adjusted to 80 Hz in order to fulfill the requirements of the post-processing pipeline. For elastography, ultrasound radiofrequency data were acquired over 1 s and transferred to the elastography computer, where the post-processing was performed.

To obtain the tissue displacement caused by multifrequency vibration, the axial phase shift between adjacent frames was calculated. Temporal Fourier transformation was used for the decomposition of the six superimposed frequencies. Thereby, three vibration frequencies were above the Nyquist limit of ½ frame rate = 40 Hz (44, 50, and 56 Hz) and appeared at the aliased spectral positions (36, 30, and 24 Hz, respectively; Tzschatzsch et al., 2016b). Further post-processing was applied for single frequencies. Noise and unwanted motion were suppressed by a spatial 2D Gaussian bandpass filter. The resulting complex valued shear wave field was directional filtered yielding eight single-directional (single wave number) wave images per frequency, which were converted into a single wave speed map by multifrequency phase gradient inversion and weighted averaging over frequency (Tzschatzsch et al., 2016a).

To exclude low SWS-values corresponding to noisy radiofrequency data, we applied a 1 m/s threshold to the elastogram, as explained by Kreft et al. (2020). To determine the average SWS in the temporal lobe parenchyma, a region of interest (ROI) was manually defined based on anatomical landmarks in the B-mode image delimiting that region from the midbrain, such as the butterfly-shaped hypoechogenic mesencephalon and the surrounding hyperechogenic basal cisterns. Areas in the elastogram that corresponded to B-mode artifacts such as reverberation artifacts from the skull were excluded from the ROI. **Figure 3** illustrates the drawn ROI in a representative volunteer. For further stabilization, measurements were repeated 10 times. Since motion was negligible, we applied the same ROI to all 10 elastograms for averaging the 10 intra-ROI SWS to one mean SWS-value. It should be noted that this mean SWS value efficiently averaged out the relatively large variability of SWS within a ROI and thus did not reflect intraregional standard deviations. The duration of a continuous examination was no longer than 2 min, which prevented heating of the skull by ultrasound energy absorption.

In order to reduce the expectation bias of the investigator who also analyzed the data, the order of THE acquisitions during all six hydration states was randomly permuted before the ROIs were drawn, and chronological order was restored just after the calculation of SWS.

Transcranial Doppler Ultrasound

A transcranial Doppler examination was performed with the ultrasound plane aligned for optimal visibility of the middle cerebral artery (MCA). One Doppler spectrum was acquired, which was used to measure mean MCA blood flow at each hydration state over a range of five heartbeats. As TCD is highly dependent on the position and alignment of the MCA in the brain, blood flow measurement in the MCA was not accomplished in all volunteers. TCD was successful in six volunteers (#1, #6, and #8–11), while THE data could be evaluated in all 12 cases.

Statistical Analysis

All physiological parameters (SWS, cerebral blood flow velocity, blood pressure, heart rate, urine osmolality, and hematocrit) were measured once at three different hydration states (NH, DH, and RH4). Therefore, physiological parameters were considered as independent variables. Correlations between the 30 SWS values (hydration states NH, DH, and RH4 for all 10 volunteers included) and all other parameters were determined by calculating Pearson's linear correlation coefficients. Correlations between age or body mass index (BMI) and SWS were calculated separately only for NH, DH, and RH4 state. Differences in SWS variation between different hydration states were assessed using Bartlett's test for equality of variances. Statistical differences between all data measured at different hydration states were tested by one-way ANOVA. Standard deviations for every hydration state were calculated based on the mean values across all subjects. For all p-values lower than 0.05, the null hypothesis was rejected.

RESULTS

A typical B-mode image and corresponding SWS maps obtained through the temporal bone window by cerebral THE at different hydration states in one volunteer are shown in **Figure 3**. A blue line delimits the selected ROI, while white labels indicate typical anatomical landmarks, including the mesencephalon and basal cisterns.

We found a moderate linear correlation between SWS and urine osmolality ($r = -0.68$, $p < 0.001$), as shown in the scatter plot in **Figure 4**, while SWS did not correlate with any other physiological parameter. Blood pressure, heart rate, cerebral blood flow velocity, and hematocrit values did not change with hydration. In contrast, urine osmolality increased

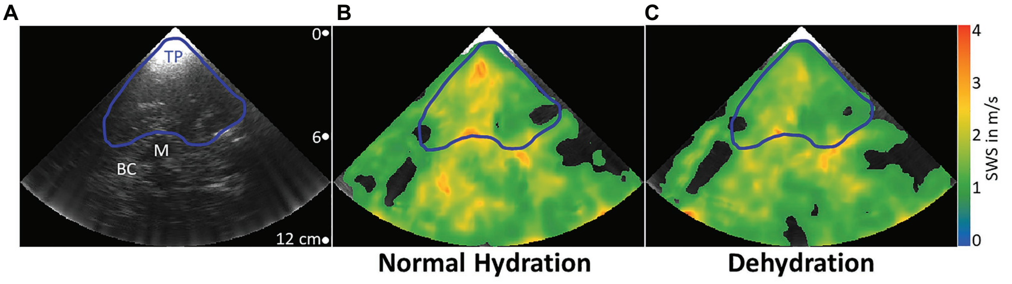

FIGURE 3 | Representative B-mode image and elastograms in normal hydrated and dehydrated states. Transcranial B-mode image **(A)**. Typical landmarks are the temporal parenchyma (blue line, TP), where ROIs were drawn, the mesencephalon (white line, M), which was used as the most prominent landmark, and basal cisterns (BC), a highly vascularized area around the mesencephalon with high echogenicity. Elastograms are shown as color-coded shear wave speed (SWS) maps. In the normally hydrated state **(B)**, mean SWS in the demarcated region of interest is higher than in the dehydrated state **(C)**.

from a normal hydration value of 324 ± 148 mOsm/kg to 784 ± 107 mOsm/kg in the dehydrated state ($p < 0.001$), as illustrated in **Figure 5A**. In two subjects (#5 and #12), changes in urine osmolality deviated from those observed in the other volunteers, which was attributed to incomplete fasting. As the two volunteers later confirmed this, they were excluded from the statistical group analysis. After water drinking, urine osmolality decreased to 288 ± 128 mOsm/kg ($p < 0.001$), which corresponded to normal hydration values ($p = 0.83$). Inversely to urine osmolality, SWS was found to decrease with dehydration from 1.64 ± 0.02 m/s to 1.57 ± 0.04 m/s ($p < 0.001$; **Figure 5B**). Within 30 min of water ingestion, SWS increased again to 1.62 ± 0.02 m/s ($p < 0.001$) and remained unchanged for another 30 min, where SWS reached a plateau. The plateau value was similar to normal hydration values (all $p > 0.9$). The variability in SWS was not different between hydration states ($p = 0.14$). All data are summarized in **Table 2**.

DISCUSSION

This study shows for the first time that de- and rehydration of brain tissue influence brain stiffness *in vivo*.

In healthy subjects, urine osmolality increases with hypertonic dehydration and decreases with oral rehydration. Conversely, in patients with renal dysfunction or chronic kidney disease, when the kidneys' ability to concentrate urine is impaired, this parameter is less markedly affected by dehydration (Roscoe, 1964; Tabibzadeh et al., 2019). In our study, two volunteers were identified as outliers not complying with the fasting protocol due to their urine osmolality. Notably, changes in SWS were still in line with the changes in urine osmolality observed in these two volunteers, providing further evidence for the high sensitivity of SWS to urine osmolality.

Unlike SWS and urine osmolality, other physiological markers such as blood pressure, heart rate, and hematocrit as well as cerebral blood flow velocity were not observed to be affected by dehydration. Other studies found a slight decrease in blood pressure and cerebral blood flow (Trangmar et al., 2014, 2015; Tsai et al., 2018; Watso and Farquhar, 2019) and an increase in heart rate variability (Castro-Sepulveda et al., 2014) upon mild hypertonic dehydration. However, these studies also measured vessel diameter, which is a critical parameter in assessing cerebral blood flow and could not be reliably assessed in this study. Additionally, the authors of these studies focused on dehydration during physical activity while our measurements were performed under resting conditions, which are characterized by relatively stable physiological parameters.

It is well-known that dehydration decreases cerebral blood volume and blood flow (Duning et al., 2005; Streitburger et al., 2012; Ryding, 2017; Sonig et al., 2020). Blood volume and blood flow in turn influence stiffness. Different studies have addressed the relationship between cerebral blood flow and CS (Guo et al., 2018). For example, studying regional variation of cerebral perfusion in deep gray matter using MRE, we found a direct and positive correlation between perfusion

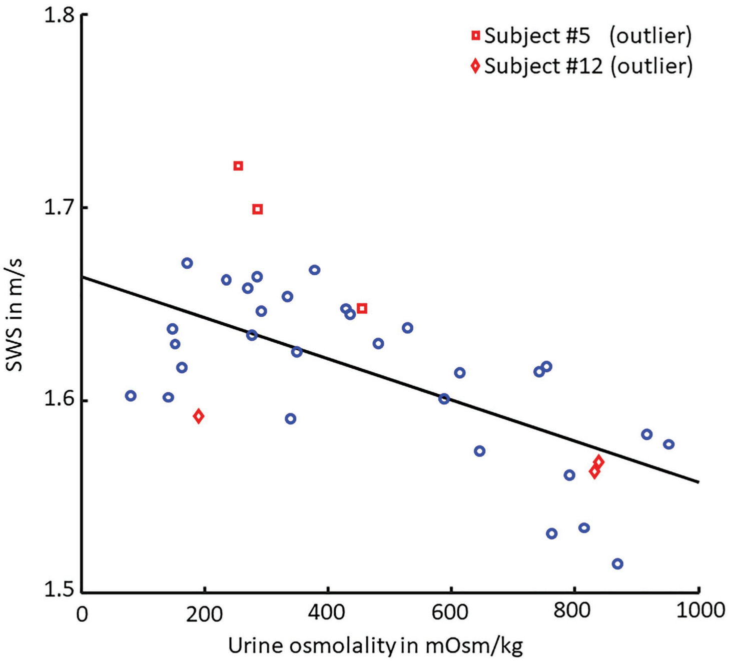

FIGURE 4 | Scatter plot of SWS vs. urine osmolality. Pearson's linear correlation between shear wave speed (SWS) and urine osmolality (30 values each, $p < 0.001$, $r = -0.68$). Linear regression is shown as black line. Volunteers #5 (□, red) and #12 (◊, red) were excluded from correlation analysis as they failed to comply with the fasting protocol.

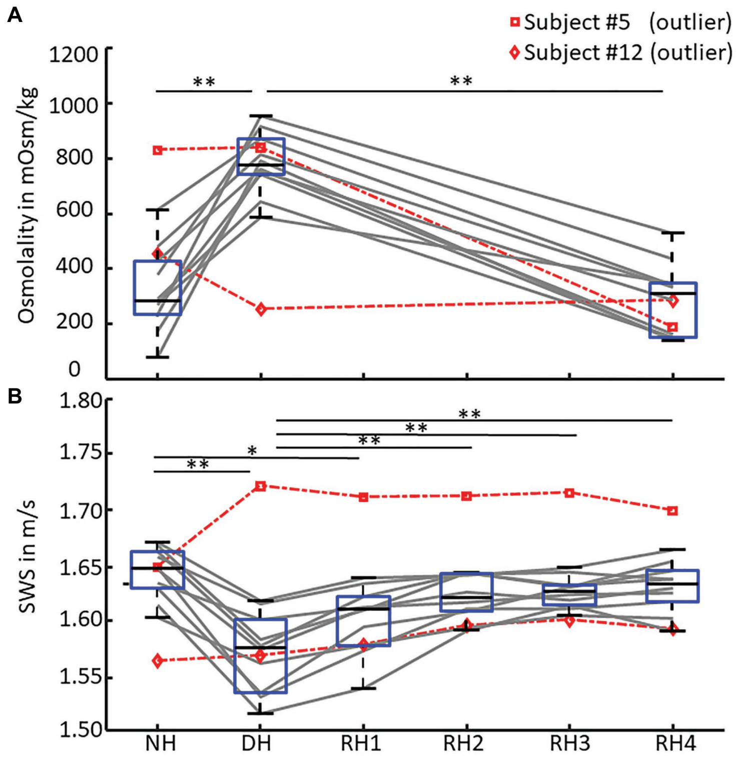

FIGURE 5 | SWS and urine osmolality changes during de- and rehydration. Boxplots of **(A)** urine osmolality for three hydration states – normal hydration (NH), dehydration (DH), and rehydration (RH4) and **(B)** mean shear wave speed (SWS) across all hydration states measured in each volunteer. Urine osmolality increased after dehydration and decreased to normal hydration values after 1 h of rehydration. Conversely, SWS significantly decreased after 12 h of fasting and returned to normal hydration values within 30 min of oral rehydration. Volunteers #5 (□, dashed red) and #12 (◊, dashed red) were excluded from statistical group analysis due to incomplete fasting, as reflected in urine osmolality and confirmed by them after the experiment. Significant differences between the groups are indicated by $^{*}p < 0.05$ and $^{**}p < 0.001$.

TABLE 2 | Group mean values (standard deviation) across volunteers (#5 and #12 excluded) for all physical parameters obtained including shear wave speed (SWS), blood pressure, heart rate, cerebral blood flow velocity, and urine osmolality.

Parameters	NH	DH	RH1	RH2	RH3	RH4
SWS in m/s	1.64 (0.02)	1.57 (0.04)	1.60 (0.03)	1.62 (0.02)	1.63 (0.01)	1.63 (0.02)
Blood pressure in mmHg	131/79 (10/6)	127/75 (7/6)	123/73 (7/9)	123/74 (7/8)	125/77 (6/8)	125/76 (9/9)
Heart rate in bpm	68 (10)	67 (9)	60 (10)	63 (11)	62 (12)	60 (10)
Cerebral blood flow velocity in cm/s	68.3 (7.7)	71.7 (4.4)	68.3 (4.8)	69.4 (6.6)	65.2 (4.6)	68.5 (4.1)
Urine osmolality in mOsm/kg	324 (148)	784 (107)	-	-	-	288 (128)
Hematocrit in %	42.4 (3)	42.2 (2.8)	-	-	-	42.7 (3.3)

All parameters were measured for normal hydration (NH), dehydration (DH), and four times during rehydration (RH1–RH4).

pressure and CS (Tzschatzsch et al., 2016b; Hetzer et al., 2018). Similarly, experimentally induced hypercapnia was associated with a synchronous increase in cerebral blood flow and CS, as revealed by MRE (Hetzer et al., 2019) and THE (Kreft et al., 2020). Previous work also revealed that the Valsalva maneuver causes an increase in CS on a short time scale in the order of seconds (Tzschatzsch et al., 2018). Taken together, this previous evidence suggests that lower cerebral blood flow, as a result of dehydration, reduces CS, which is consistent with the observations made in our study. However, with 4.4 ± 1.7%, the observed effect of dehydration is relatively small, which may be attributable to two factors: first, tissue stiffness is only indirectly linked to blood perfusion through poroelastic interactions such as have been described for *in vivo* brain tissue (McGarry et al., 2015, 2019; Parker, 2017; Lilaj et al., 2020). Second, autoregulation of cerebral blood volume, perfusion pressure, and intracranial pressure only occurs across a small range of biophysical property changes and possibly compensates for minor changes in CS (Donnelly et al., 2015; Moerman and De Hert, 2019). Nevertheless, the observed decrease in SWS from normal hydration to dehydration is significant and potentially adds to the variability of CS measured in patients. Therefore, we recommend that cerebral elastography be performed under normal hydration conditions.

Our study has limitations. Since we did not record any parameters to determine renal function, the urine osmolality we measured, although correlated with SWS, can only be considered as indirect measurements of body tissue dehydration. In TCD measurements, the exact transducer positioning relative to flow direction influences the measured blood velocity value. Therefore, variability of TCD is relatively high and operator dependent. Our experimental setup was optimized for THE leading to a relatively high drop-out rate of 6 from 12 and limited statistical power of our TCD data for the comparison to published values of cerebral blood flow during de- and rehydration (Trangmar et al., 2014, 2015). Additionally, our volunteers did not observe a standardized diet *before* fasting, which may have led to variability in our SWS data due to individual adaptation mechanisms. Further biological confounders of brain stiffness should be investigated by cerebral THE in a larger group of volunteers observing standardized conditions.

In summary, CS was measured by cerebral THE in a group of healthy volunteers who fasted overnight to induce mild hypertonic dehydration of brain tissue. We found dehydration to cause a slight decrease in CS on the order of 4.4%. CS increased to normal values within 1/2 h of drinking water. CS correlated with urine osmolality but not with hematocrit. Brain softening due to dehydration might be explained by reduced cerebral perfusion in agreement with prior findings of MRE and THE on the correlation between cerebral perfusion and CS. To minimize variability of CS values in a standardized protocol of cerebral elastography, examiners should make sure that volunteers or patients are in normal hydration states during the examination.

DATA AVAILABILITY STATEMENT

All data needed to evaluate the conclusions drawn in the article have been presented in the manuscript. Additional data may be requested from the authors.

ETHICS STATEMENT

The studies involving human participants were reviewed and approved by Institutional Review Board of Charité - Universitätsmedizin Berlin. The patients/participants provided their written informed consent to participate in this study.

AUTHOR CONTRIBUTIONS

All authors contributed to the conception and design of the study and formed the hypothesis. BK, HT, MS, and SH acquired the data. BK, HT, and LD analyzed the data. BK, HT, LD, and IS drafted the manuscript. All authors carried out critical revision of the manuscript equally.

FUNDING

The authors acknowledge funding from the German Research Foundation (DFG, SFB1340 Matrix in Vision, GRK2260 BIOQIC).

REFERENCES

Armstrong, L. E. (2005). Hydration assessment techniques. *Nutr. Rev.* 63, S40–S54. doi: 10.1111/j.1753-4887.2005.tb00153.x

Ashcroft, F. (2001). *Life at the extremes*. London: Flamingo.

Bhave, G., and Neilson, E. G. (2011). Volume depletion versus dehydration: how understanding the difference can guide therapy. *Am. J. Kidney Dis.* 58, 302–309. doi: 10.1053/j.ajkd.2011.02.395

Brian D Coley, L. A. F., Hashimoto, B. E., Hernanz-Schulman, M., Rumack, C. M., Cohen, H. L., Mccarville, M. E., et al. (2012). AIUM practice guideline for the performance of a transcranial Doppler ultrasound examination for adults and children. *J. Ultrasound Med.* 31, 1489–1500. doi: 10.7863/jum.2012.31.9.1489

Castro-Sepulveda, M., Cerda-Kohler, H., Perez-Luco, C., Monsalves, M., Andrade, D. C., Zbinden-Foncea, H., et al. (2014). Hydration status after exercise affect resting metabolic rate and heart rate variability. *Nutr. Hosp.* 31, 1273–1277. doi: 10.3305/nh.2015.31.3.8523

Dittmann, F., Tzschatzsch, H., Hirsch, S., Barnhill, E., Braun, J., Sack, I., et al. (2017). Tomoelastography of the abdomen: tissue mechanical properties of the liver, spleen, kidney, and pancreas from single MR elastography scans at different hydration states. *Magn. Reson. Med.* 78, 976–983. doi: 10.1002/mrm.26484

Donnelly, J., Aries, M. J., and Czosnyka, M. (2015). Further understanding of cerebral autoregulation at the bedside: possible implications for future therapy. *Expert. Rev. Neurother.* 15, 169–185. doi: 10.1586/14737175.2015.996552

Duning, T., Kloska, S., Steinstrater, O., Kugel, H., Heindel, W., and Knecht, S. (2005). Dehydration confounds the assessment of brain atrophy. *Neurology* 64, 548–550. doi: 10.1212/01.WNL.0000150542.16969.CC

Gandhi, D., Kalra, P., Raterman, B., Mo, X., Dong, H., and Kolipaka, A. (2020). Magnetic resonance elastography-derived stiffness of the kidneys and its correlation with water perfusion. *NMR Biomed.* 33:e4237. doi: 10.1002/nbm.4237

Guo, J., Dittmann, F., and Braun, J. (2018). "Sensitivity of tissue shear stiffness to pressure and perfusion in health and disease" in *Quantification of biophysical parameters in medical imaging*. eds. I. Sack and T. Schaeffter (Springer Nature), 429–449.

Hetzer, S., Birr, P., Fehlner, A., Hirsch, S., Dittmann, F., Barnhill, E., et al. (2018). Perfusion alters stiffness of deep gray matter. *J. Cereb. Blood Flow Metab.* 38, 116–125. doi: 10.1177/0271678X17691530

Hetzer, S., Dittmann, F., Bormann, K., Hirsch, S., Lipp, A., Wang, D. J., et al. (2019). Hypercapnia increases brain viscoelasticity. *J. Cereb. Blood Flow Metab*. 39, 2445–2455. doi: 10.1177/0271678X18799241

Ipek-Ugay, S., Tzschatzsch, H., Hudert, C., Marticorena Garcia, S. R., Fischer, T., Braun, J., et al. (2016). Time harmonic elastography reveals sensitivity of liver stiffness to water ingestion. *Ultrasound Med. Biol.* 42, 1289–1294. doi: 10.1016/j.ultrasmedbio.2015.12.026

Jablonski, S. (2012). Oral rehydration of the pediatric patient with mild to moderate dehydration. *J. Emerg. Nurs.* 38, 185–187. doi: 10.1016/j.jen.2011.12.001

Jequier, E., and Constant, F. (2010). Water as an essential nutrient: the physiological basis of hydration. *Eur. J. Clin. Nutr.* 64, 115–123. doi: 10.1038/ejcn.2009.111

Kreft, B., Tzschatzsch, H., Schrank, F., Bergs, J., Streitberger, K. J., Waldchen, S., et al. (2020). Time-resolved response of cerebral stiffness to Hypercapnia in humans. *Ultrasound Med. Biol.* 46, 936–943. doi: 10.1016/j.ultrasmedbio.2019.12.019

Lauriola, M., Mangiacotti, A., D'onofrio, G., Cascavilla, L., Paris, F., Paroni, G., et al. (2018). Neurocognitive disorders and dehydration in older patients: clinical experience supports the hydromolecular hypothesis of dementia. *Nutrients* 10:562. doi: 10.3390/nu10050562

Lilaj, L., Fischer, T., Guo, J., Braun, J., Sack, I., and Hirsch, S. (2020). Separation of fluid and solid shear wave fields and quantification of coupling density by magnetic resonance poroelastography. *Magn. Reson. Med.* 85, 1655–1668. doi: 10.1002/mrm.28507

Marinoni, M., Ginanneschi, A., Forleo, P., and Amaducci, L. (1997). Technical limits in transcranial Doppler recording: inadequate acoustic windows. *Ultrasound Med. Biol.* 23, 1275–1277. doi: 10.1016/s0301-5629(97)00077-x

Marticorena Garcia, S. R., Grossmann, M., Lang, S. T., Tzschatzsch, H., Dittmann, F., Hamm, B., et al. (2018). Tomoelastography of the native kidney: regional variation and physiological effects on in vivo renal stiffness. *Magn. Reson. Med.* 79, 2126–2134. doi: 10.1002/mrm.26892

Mcgarry, M. D., Johnson, C. L., Sutton, B. P., Georgiadis, J. G., Van Houten, E. E., Pattison, A. J., et al. (2015). Suitability of poroelastic and viscoelastic mechanical models for high and low frequency MR elastography. *Med. Phys.* 42, 947–957. doi: 10.1118/1.4905048

Mcgarry, M., Van Houten, E., Solamen, L., Gordon-Wylie, S., Weaver, J., and Paulsen, K. (2019). Uniqueness of poroelastic and viscoelastic nonlinear inversion MR elastography at low frequencies. *Phys. Med. Biol.* 64:075006. doi: 10.1088/1361-6560/ab0a7d

Mitchell, H. H., Hamilton, T. S., Steggerda, F. R., and Bean, H. W. (1945). The chemical composition of the adult human body and its bearing on the biochemistry of growth. *J. Biol. Chem.* 158, 625–637.

Moerman, A., and De Hert, S. (2019). Why and how to assess cerebral autoregulation? *Best Pract. Res. Clin. Anaesthesiol.* 33, 211–220. doi: 10.1016/j.bpa.2019.05.007

Parker, K. J. (2017). Are rapid changes in brain elasticity possible? *Phys. Med. Biol.* 62, 7425–7439. doi: 10.1088/1361-6560/aa8380

Patterson, S. M., Vanderkaay, M. M., Shanholtzer, B. A., and Patterson, C. A. (2008). Influence of acute fluid loading on stress-induced hemoconcentration and cardiovascular reactivity. *J. Behav. Med.* 31, 319–330. doi: 10.1007/s10865-008-9162-7

Roscoe, M. H. (1964). Urine in acute and chronic renal failure. *Br. Med. J.* 1, 1084–1087. doi: 10.1136/bmj.1.5390.1084

Ryding, E. (2017). The relationship between intracranial pressure increase and volume of brain compression. *J. Neurol. Neurophysiol.* 8:436. doi: 10.4172/2155-9562.1000436

Sack, I., and Schaeffter, T. (2018). *Quantification of biophysical parameters in medical imaging*. Springer Nature.

Sonig, A., Jumah, F., Raju, B., Patel, N. V., Gupta, G., and Nanda, A. (2020). The historical evolution of intracranial pressure monitoring. *World Neurosurg.* 138, 491–497. doi: 10.1016/j.wneu.2020.03.028

Spital, A. (2007). Dehydration versus volume depletion--and the importance of getting it right. *Am. J. Kidney Dis.* 49, 721–722. doi: 10.1053/j.ajkd.2007.03.012

Streitburger, D. P., Moller, H. E., Tittgemeyer, M., Hund-Georgiadis, M., Schroeter, M. L., and Mueller, K. (2012). Investigating structural brain changes of dehydration using voxel-based morphometry. *PLoS One* 7:e44195. doi: 10.1371/journal.pone.0044195

Tabibzadeh, N., Wagner, S., Metzger, M., Flamant, M., Houillier, P., Boffa, J. J., et al. (2019). Fasting urinary osmolality, CKD progression, and mortality: a prospective observational study. *Am. J. Kidney Dis.* 73, 596–604. doi: 10.1053/j.ajkd.2018.12.024

Trangmar, S. J., Chiesa, S. T., Llodio, I., Garcia, B., Kalsi, K. K., Secher, N. H., et al. (2015). Dehydration accelerates reductions in cerebral blood flow during prolonged exercise in the heat without compromising brain metabolism. *Am. J. Physiol. Heart Circ. Physiol.* 309, H1598–H1607. doi: 10.1152/ajpheart.00525.2015

Trangmar, S. J., Chiesa, S. T., Stock, C. G., Kalsi, K. K., Secher, N. H., and Gonzalez-Alonso, J. (2014). Dehydration affects cerebral blood flow but not its metabolic rate for oxygen during maximal exercise in trained humans. *J. Physiol.* 592, 3143–3160. doi: 10.1113/jphysiol.2014.272104

Tsai, Y. H., Yang, J. L., Lee, I. N., Yang, J. T., Lin, L. C., Huang, Y. C., et al. (2018). Effects of dehydration on brain perfusion and infarct Core after acute middle cerebral artery occlusion in rats: evidence from high-field magnetic resonance imaging. *Front. Neurol.* 9:786. doi: 10.3389/fneur.2018.00786

Tzschatzsch, H., Guo, J., Dittmann, F., Hirsch, S., Barnhill, E., Johrens, K., et al. (2016a). Tomoelastography by multifrequency wave number recovery from time-harmonic propagating shear waves. *Med. Image Anal.* 30, 1–10. doi: 10.1016/j.media.2016.01.001

Tzschatzsch, H., Kreft, B., Schrank, F., Bergs, J., Braun, J., and Sack, I. (2018). In vivo time-harmonic ultrasound elastography of the human brain detects acute cerebral stiffness changes induced by intracranial pressure variations. *Sci. Rep.* 8:17888. doi: 10.1038/s41598-018-36191-9

Tzschatzsch, H., Nguyen Trong, M., Scheuermann, T., Ipek-Ugay, S., Fischer, T., Schultz, M., et al. (2016b). Two-dimensional time-harmonic elastography of the human liver and spleen. *Ultrasound Med. Biol.* 42, 2562–2571. doi: 10.1016/j.ultrasmedbio.2016.07.004

Watso, J. C., and Farquhar, W. B. (2019). Hydration status and cardiovascular function. *Nutrients* 11:186. doi: 10.3390/nu11081866

Conflict of Interest: The authors declare that the research was conducted in the absence of any commercial or financial relationships that could be construed as a potential conflict of interest.

Copyright © 2021 Kreft, Bergs, Shahryari, Danyel, Hetzer, Braun, Sack and Tzschätzsch. This is an open-access article distributed under the terms of the Creative Commons Attribution License (CC BY). The use, distribution or reproduction in other forums is permitted, provided the original author(s) and the copyright owner(s) are credited and that the original publication in this journal is cited, in accordance with accepted academic practice. No use, distribution or reproduction is permitted which does not comply with these terms.

Journal Data Filtered By: **Selected JCR Year: 2019** Selected Editions: SCIE,SSCI
Selected Categories: **“RADIOLOGY, NUCLEAR MEDICINE and MEDICAL IMAGING”** Selected Category Scheme: WoS
Gesamtanzahl: 133 Journale

Rank	Full Journal Title	Total Cites	Journal Impact Factor	Eigenfactor Score
1	JACC-Cardiovascular Imaging	10,110	12.740	0.027550
2	MEDICAL IMAGE ANALYSIS	9,028	11.148	0.017100
3	RADIOLOGY	52,731	7.931	0.057130
4	JOURNAL OF NUCLEAR MEDICINE	26,844	7.887	0.032990
5	EUROPEAN JOURNAL OF NUCLEAR MEDICINE AND MOLECULAR IMAGING	15,787	7.081	0.023630
6	IEEE TRANSACTIONS ON MEDICAL IMAGING	21,657	6.685	0.030060
7	CLINICAL NUCLEAR MEDICINE	5,042	6.587	0.006200
8	NEUROIMAGE	102,632	5.902	0.125360
9	Photoacoustics	715	5.870	0.001760
10	INTERNATIONAL JOURNAL OF RADIATION ONCOLOGY BIOLOGY PHYSICS	44,197	5.859	0.042160
11	Circulation-Cardiovascular Imaging	5,574	5.691	0.016320
12	ULTRASOUND IN OBSTETRICS & GYNECOLOGY	13,078	5.571	0.018050
13	JOURNAL OF CARDIOVASCULAR MAGNETIC RESONANCE	5,205	5.361	0.011120
14	INVESTIGATIVE RADIOLOGY	6,136	5.156	0.008830
15	RADIOGRAPHICS	12,418	4.967	0.010750
16	ULTRASCHALL IN DER MEDIZIN	2,185	4.966	0.002530
17	RADIOTHERAPY AND ONCOLOGY	17,774	4.856	0.026510
18	European Heart Journal-Cardiovascular Imaging	6,359	4.841	0.023110
19	HUMAN BRAIN MAPPING	23,094	4.421	0.042760
20	Journal of the American College of Radiology	4,409	4.268	0.010730

Selected JCR Year: 2019; Selected Categories: “RADIOLOGY, NUCLEAR MEDICINE and MEDICAL IMAGING”

Kreft B, Tzschätzsch H, Shahryari M, Haffner P, Braun J, Sack I, Streitberger KJ. Noninvasive Detection of Intracranial Hypertension by Novel Ultrasound Time-Harmonic Elastography. Invest Radiol. 2022 Feb 1;57(2):77-84.

doi: https://doi.org/10.1097/RLI.0000000000000817.

Curriculum Vitae

Mein Lebenslauf wird aus datenschutzrechtlichen Gründen in der elektronischen Version meiner Arbeit nicht veröffentlicht.

Danksagung

An dieser Stelle möchte ich allen beteiligten Personen meinen Dank aussprechen, die mich bei der Anfertigung meiner Dissertation unterstützt haben.

Mein besonderer Dank geht an Professor Ingolf Sack, Dr. Jürgen Braun und Dr. Heiko Tzschätzsch für die hervorragende Betreuung und die enorme Unterstützung bei der Umsetzung dieses Projektes. Vielen Dank für die Verwandlung meiner Fehler in wertvolle Lektionen, die Ausarbeitung meiner Interessen in Stärken und das Teilen unschätzbaren Wissens und Erfahrungen mit mir.

Außerdem möchte ich mich bei meinen Kollegen und Freunden Anna-Sophie Morr, Tom Meyer, Yasmine Safraou, Jakob Jordan, Yang Yang, Ledia Lilaj, Carsten Warmuth, Jing Guo, Felix Schrank, Florian Dittmann, Gergeley Bertalan, Helge Herthum, Joachim Snellings, Judith Bergs, Karolina Garczynska, Matthias Anders, Mehrgan Shahryari, Rolf Otto Reiter, Steffen Görner, Stephan Marticorena Garcia, Stefan Hetzer, Yavuz Uca, Markus Grossmann, Christian Burkhardt und Judith Bergs bedanken, die meine Arbeit durch ihre Unterstützung, ihren Rat und mit produktiven Gesprächen bereichert haben.

Nicht zuletzt möchte ich mich bei meinem besten Freund Moritz Muthwill bedanken, der in jeder Situation und jederzeit zu mir steht und auch in schwierigen Zeiten immer die richtigen Worte findet. „Et hätt noch immer jot jejange!“

Ein besonderer Dank geht auch an meine Freundin Hasret Ayhan, die mir in jeglichen Situationen mit ihrer Liebe und ihrem Rat zur Seite steht.

Zu guter Letzt möchte ich meinen Eltern Peter und Maria Kreft sowie meiner Schwester Janine Reinhardt für ihren Rückhalt, ihre Geduld und ihre Ermutigung während meines gesamten Studiums und der Arbeit an dieser Dissertation danken. Ein besonderer Dank gilt meinem Bruder Markus Kreft, der mich zu meinem Berufsweg inspirierte.

Vielen Dank!